Improving the early Eocene timescale

High-precision $^{40}Ar/^{39}Ar$ geochronology and integrated stratigraphy of the Willwood and Tatman Formations in the Bighorn Basin (Wyoming, USA)

Research Project Master Earth Sciences (AM_1187) - 27EC
Vrije Universiteit Amsterdam, Faculty of Science, Geology & Geochemistry

Edwin Kruitbosch
Student number 2538285
edwinkruitbosch@gmail.com

Supervisors

K.F. Kuiper, Faculty of Science (k.f.kuiper@vu.nl)

R.J.G. Kaandorp, Faculty of Science (ron.kaandorp@vu.nl)

A. Turtù, Faculty of Science (turtuantonio@gmail.com)

12 October 2021

Cover photo: view on Tatman Mountain from the Blackburn Gulch section (by A. Turtù).

Abstract

The early Eocene is characterised by transient greenhouse warming events marking perturbations of the global carbon cycle. Terrestrial geochemical proxies facilitate evaluation of these hyperthermal events - having durations in the order of 10^5 yr - in a high-resolution timeframe. The northern Bighorn Basin has provided such proxies for the Paleocene-Eocene Thermal Maximum up to hyperthermal I2 constrained by basin-wide magnetostratigraphy, an exceptional mammal biostratigraphy and, more recently, floating astrochronological timescales. The astrochronology is based on inferred ~21 kyr precession-control on the fluvial stacking pattern in the Willwood Fm. allowing unprecedented time control. To extend the proxies upward, the central part of the basin has to be sampled. However, age models in the central Bighorn Basin suffer from discrepancies in the age of the Willwood Ash, uncertainties in the magnetostratigraphic record and disagreement with inferred precession forcing.

This thesis presents an updated chronostratigraphic framework for the central basin including 1) high-precision $^{40}Ar/^{39}Ar$ dating of the Willwood Ash (52.53 ± 0.04/0.86 Ma; 2σ internal/external error) and three new, younger tephras SB-3 (52.20 ± 0.04/0.85 Ma), SB-4 (52.08 ± 0.04/0.85 Ma) and SB-5 (51.94 ± 0.09/0.85 Ma); 2) new magnetostratigraphy interpreted as the top of Chron C24 and base of C23 and 3) new detailed stratigraphy and cyclostratigraphy of the Willwood Fm. (cyclicity of 7.8 ± 1.7 m and 4.4 ± 0.7 m period; 1 standard deviation) and overlying Tatman Fm. (6.5 ± 1.3 m). The chronostratigraphic framework suggests that the upper part of the Willwood Fm. is ~0.5 Myr younger than formerly thought. Climate and carbon cycle proxies spanning the Paleocene-Eocene Thermal Maximum to the Early Eocene Climatic Optimum can be obtained from the Bighorn Basin. However, discrepancies with previous age models remain and, consequently, precession forcing in the basin cannot be confirmed.

Abbreviations

AF	Alternating field (demagnetization)
$^{40}Ar^*$	Radiogenic ^{40}Ar
BBG	Blackburn Gulch section
BBGD	Blackburn Gulch Downward extension
BBGU	Blackburn Gulch Upward extension
ChRM	Characteristic remnant magnetisation
CSD	Circular standard deviation
EECO	Early Eocene Climatic Optimum
ETM	Eocene Thermal Maximum
FCT	Fish Canyon Tuff
FPR	Fenton Pass Road section
GSI	Grain size index
GTS	Geological Timescale
MAD	Maximum angular deviation
MDF	Mass discrimination factor
MSWD	Mean squared weighted deviations
NALMA	North American Land Mammal Age
NRM	Natural remnant magnetisation
PCA	Principal component analysis
PETM	Paleocene-Eocene Thermal Maximum
PDD	Probability density distribution
Pmag	Paleomagnetism
SBN	Squaw Buttes North section
SBND	Squaw Buttes Downward extension
SBS	Squaw Buttes South section
SBU	Squaw Buttes Upward extension
SDI	Soil development index
TH	Thermal (demagnetization)

Table of contents

Appendices

1. Introduction

The early Eocene (Ypresian, 56-48 Ma) represents the warmest period in the Cenozoic Era. A long term warming trend, initiated in the late Paleocene, reached its peak during the Early Eocene Climatic Optimum (EECO, ~49-53 Ma; Zachos et al., 2001; Speijer et al., 2020) and was punctuated by a series of distinctive hyperthermal events such as the Paleocene-Eocene Thermal Maximum (PETM), the Eocene Thermal Maximum 2 (ETM2; or Elmo or H1) and the Eocene Thermal Maximum 3 (ETM3; or K or X event; Kennett and Stott, 1991; Cramer et al., 2003; Lourens et al., 2005; Zachos et al., 2010; Westerhold et al., 2017). Hyperthermals, often considered analogous to present-day climate change (Zachos et al., 2008), are primarily evidenced by negative $\delta^{13}C$ excursions in both terrestrial and marine settings which are paced by orbital eccentricity (Cramer et al., 2003; Lourens et al., 2005; Zachos et al., 2010; Lauretano et al., 2016; Westerhold et al., 2017). Therefore, to understand causes, implications and coupling of the marine and terrestrial realm during these events (Zachos et al., 2001, 2010; McInerney and Wing, 2011; references therein), detailed chronostratigraphic frameworks from both realms are needed. Marine archives have provided continuous, astronomically tuned cyclostratigraphic records - contributing to the astronomical age model that almost completely underlies the Paleogene period in the Geologic Timescale 2020 (GTS 2020; Speijer et al., 2020; Francescone et al., 2019; Westerhold et al., 2017) - but carbonate dissolution and low sedimentation rates restrict their time resolution (Westerhold et al., 2018). Continental records, on the other hand, can provide high resolution age models for the carbon isotope excursions owing to high sedimentation rates.

The first terrestrial PETM section was recognised in the Bighorn Basin, Wyoming (Koch et al., 1992; McInerney and Wing, 2011) and since then four more hyperthermals (up to I2) have been identified (Abels et al., 2012, 2016). $\delta^{13}C$ records in the Bighorn Basin are predominantly obtained from carbonate nodules in floodplain paleosols, and basin-wide geochronology traditionally stems from an exceptional mammal biostratigraphy, part of the North American Land Mammal Ages (NALMA; Gingerich and Clyde, 2001; Speijer et al., 2020; references therein), and magnetostratigraphy (Butler et al., 1981; Clyde et al., 1994; Tauxe et al., 1994; Secord et al., 2006; Clyde et al., 2007; overview in the latter). Additionally, two radio-isotopic tie-points have been produced: the Belt Ash (~59 Ma; Secord et al., 2006) and

the Willwood Ash (~53 Ma; Wing et al., 1991; Smith et al., 2004), both also incorporated in the radio-isotopic age model of the Geologic Timescale 2012 (Vandenberghe et al., 2012). More recently, astronomical timescales for local sections have been constructed based on the cyclic stacking pattern of floodplain deposits of the Willwood Formation (Abdul Aziz et al., 2008; Abels et al., 2012, 2013; Westerhold et al., 2018; van der Meulen et al., 2020). The stacking pattern - alternating avulsion and pedogenically altered floodplain deposits - is considered orbitally forced by ~21 kyr precession (see Abels et al. (2013) for model). Cyclostratigraphic records have successfully delivered timing and durations for different stages of the PETM (Abdul Aziz et al., 2008; Westerhold et al., 2018; van der Meulen et al., 2020) and younger hyperthermals (Abels et al., 2012).

However, problems in the Bighorn Basin chronostratigraphic framework remain. In the northern part of the basin, and lower part of the Willwood Fm., sedimentation rates derived from magnetostratigraphy and cyclostratigraphy are in agreement; whereas in the central part, and upper Willwood Fm., the scarcer cyclostratigraphic records require higher sedimentation rates for a link to precession than indicated by magnetostratigraphy and the Willwood Ash age (Abdul Aziz et al., 2008). Alternatively, Hajek and Straub (2017) suggest that autogenic sedimentary processes alone might be able to explain the cyclic deposition of the Willwood Fm. The age model discrepancy can also arise from large uncertainties in the magnetostratigraphy of the central part of the basin (Tauxe et al., 1994): in particular the Chron C24r-C24n.3n reversal has been interpreted at two different positions implying either an asynchronous faunal reorganisation (Biohorizon B) or strong normal overprints (see discussion in Clyde et al. (2007)). Persistent normal overprints have indeed been reported in most paleomagnetic studies of the Willwood Fm. (Tauxe et al., 1994; Clyde et al., 1994; Clyde et al., 2007). Furthermore, Tauxe et al. (1994) placed the Chron C24n.1r-C24n.1n reversal in a zone where individual samples show large scatter in polarity and were not able to interpret polarity for their samples in the overlying Tatman Fm. The age of the Willwood Ash and its magnetostratigraphic position has also been disputed (Clyde et al., 2004; Smith et al., 2004). Smith et al. (2004) determined a significantly younger age (~0.5 Ma) than the original - but recalculated - age of Wing et al. (1991; respectively through total fusion and step heating $^{40}Ar/^{39}Ar$ analysis of 1 to 3 sanidine crystals and multigrain sanidine total fusion $^{40}Ar/^{39}Ar$ analysis). Smith et al. (2004) attributed the inconsistency to contamination of

xenocrystic or detrital grains in the multigrain analysis of Wing et al. (1991). Finally, zooming in on individual cyclic floodplain units, lateral and vertical variations in thickness and sand bodies hamper cycle counting of bandpass-filtered cyclostratigraphic records, so van der Meulen et al. (2020) emphasize that reliable precession-based age models cannot be constructed without parallel sections and detailed assessment of sedimentary facies.

This study sets out to improve the chronostratigraphic framework in the central part of the Bighorn Basin with the goal to 1) provide a solid age model for future extension of geochemical climate proxies from carbonate nodules to the top of the Willwood Fm., 2) test the inferred precession control on the Willwood Fm. fluvial stacking pattern and 3) contribute high-precision radio-isotopic tie-points for the early Eocene, specifically the Chron C24-C23 interval. Two new composite sections, from the top of the Willwood Fm. and into the overlying Tatman Fm., are presented (Blackburn Gulch and Squaw Buttes, Fig. 1.1), including detailed sedimentology and stratigraphy, tephrochronology, magnetostratigraphy and cyclostratigraphy. To obtain new and independent time control, the Willwood Ash and three younger, recently identified tephras in the Tatman Fm. were dated through high-precision, single grain sanidine $^{40}Ar/^{39}Ar$ analysis an order of magnitude more precise than previous Willwood Ash ages (Wing et al., 1991; Smith et al., 2004). A new magnetostratigraphic record was built corresponding to the top of the composite of Tauxe et al., (1994) to resolve uncertainties related to magnetostratigraphic interpretations and to correlate the new sections to the basin-wide magnetostratigraphic and biostratigraphic framework (e.g. Clyde et al., 2007). In addition, a simple thermomagnetic analysis was carried out to better understand the magnetic mineralogy and its role as carriers of primary and secondary remnant magnetisation. Further, time series analysis of colour reflectance and soil development index records from the top of the Willwood Fm., combined with lithostratigraphic logs from the two partly parallel composite sections, allow the development of a cyclostratigraphic record that can be evaluated against the $^{40}Ar/^{39}Ar$ chronology. As the new sections extend into the Tatman Fm. and rhythmic lithostratigraphic alternations were recognised here as well, this thesis also presents a first cyclostratigraphic analysis in this formation. The combined age model for the new composite sections additionally facilitates evaluation of the significance of the boundary between the paleosol-rich Willwood and paleosol-poor Tatman Fm.

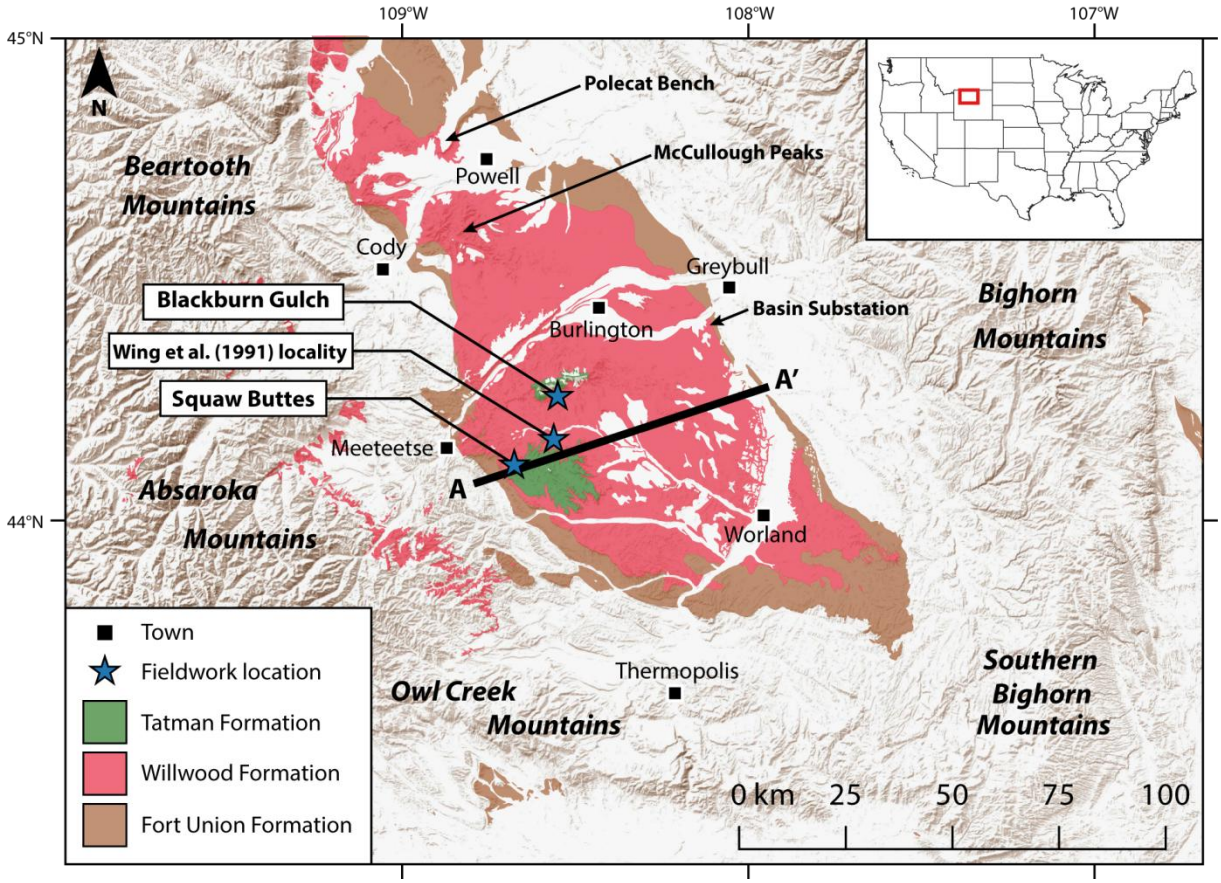

Figure 1.1 *- Geographical and geological setting of the Bighorn Basin, Wyoming, USA. Study areas indicated by blue stars. Geological map (USGS) overlies terrain map (ESRI) and only shows Paleocene and early Eocene formations. Cross section A - A' is shown in Fig. 2.1.*

2. Geological setting

2.1 Geographical setting

The Bighorn Basin, located in north-western Wyoming, is an intramontane basin in the Western Interior and is part of a NW-SE trending structural through that extends into central Montana (Gingerich, 1983). The basin has an oval shape bordered by mountain ranges (Fig. 1.1): the Bighorn Mountains separate the basin from the Powder Basin in the east; the Southern Bighorn Mountains, Bridger Mountains and Owl Creek mountains form the border with the Wind River Basin in the south; and the Absaroka Mountains and Beartooth Mountains separate the basin from the Yellowstone area in the west. In the north, the Bighorn Basin continues as the Clark's Fork Basin (Gingerich, 1983).

2.2 Structural and stratigraphic evolution

In the Late Jurassic, the Western Interior developed as retroarc foreland basin of the Cordilleran Orogen and vast areas were covered by marine and marginal environments of the Western Interior Seaway (Miall et al., 2008; DeCelles, 2004). Starting in the Late Cretaceous, a phase of thick-skin deformation - the Laramide orogeny - propagated eastward from the Cordillera and compartmentalised the western part of the foreland into several asymmetrical intramontane basins, including the Bighorn area (Fan and Carrapa, 2014). Laramide deformation was first marked in the Bighorn area by uplift of the Bighorn and Beartooth Mountains and was accompanied in the Paleocene by uplift of the Southern Bighorn and Owl Creek Mountains (Bown, 1980). The increasingly enclosed basin developed asymmetrical with its synclinical axis located on the west side of the basin, reflected by the thickness variation of the Paleocene Fort Union Fm. (Fig. 2.1). Basin subsidence was continuous over the late Paleocene-early Eocene with average subsidence rates of 200-250 m/Myr in the northern part of the basin and 85 m/Myr in the southern part (Clyde et al., 2007).

During Fort Union deposition, predominantly comprising fluvial sediments, the Bighorn Basin became permanently part of the continental realm (Bown, 1980). Fluvial sedimentation continued at the end of the Paleocene and into the early Eocene by deposition of the Willwood Fm. (Bown, 1980). Persisting deformation of the southern mountain ranges

reversed the major drainage direction from southeast to northwest during Willwood deposition (Bown, 1980). At the end of the early Eocene a lake system evolved and deposition of the Tatman Formation began (Bown, 1980; Rohrer and Smith, 1969). Volcanic activity in the Yellowstone and Absaroka area began at the end of Willwood deposition as is evidenced by tuffaceous strata in the upper Willwood and Tatman formations (Bown, 1980; Rohrer and Smith, 1969).

The Absoraka volcanic field was uplifted throughout the Eocene, while volcaniclastic and subsequent Oligocene fluvial deposition filled the basin up to the lower crests of the Bighorn Mountains (Bown, 1980, 1982). Post-Oligocene epeirogenic uplift of the Western Interior, continuing to present day, lowered base level and caused rivers to excavate the Bighorn Basin extensively (Bown, 1980; Gingerich, 1983). At present, the Bighorn basin lies at an >1km altitude and essentially horizontal Willwood and Tatman strata represent the majority of outcrops in the central part of the basin (Fig. 2.1).

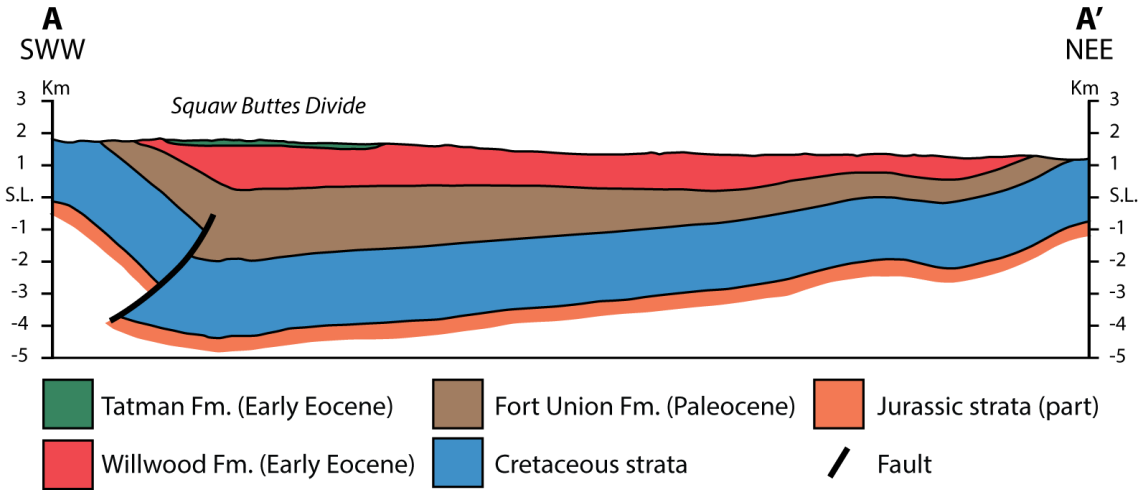

Figure 2.1 *- Simplified cross section through the central Bighorn Basin; location in Fig. 1.1. Vertical exaggeration: ~2x. S.L. = sea level. Adapted from Wyoming State Geological Survey.*

2.3 Willwood Formation

The Willwood Fm., coined by van Houten (1944), predominantly consists of variegated mudrocks and lenticular and sheet sandstones, while carbonaceous shales and conglomerates form minor constituents (Neasham and Vondra, 1972). The formation is well known for its rich vertebrate fossil record predominantly comprising mammals, crocodilians and turtles (Gingerich and Clyde, 2001). The Willwood Fm. is distributed along the central

part of the Bighorn and Clark's Fork Basins and has a thickness of ~700 m and ~1100 m, respectively (Gingerich, 1983). Deposition occurred in marginal alluvial fans grading basinward into meander channels on floodplains where distinctive coloured soils formed yielding abundant carbonate nodules (Neasham and Vondra, 1972). In the marginal areas, the Willwood Fm. overlies the Fort Union Fm. (or older rocks) above an angular unconformity, indicating previous deformation and erosion of the basin margins (Bown, 1980). Conversely, in axial parts of the basin, the contact with the Fort Union Fm. is conformable and the boundary between the two fluvial units is placed at the first occurrence of red banding (van Houten, 1944; Neasham and Vondra, 1972).

Three components make up the floodplain sedimentological architecture: 1) sheet sandstones deposited by meandering trunk rivers, 2) mudrocks with strong pedogenic development deposited as overbank fines and 3) heterolithic strata with weak paleosol development deposited by avulsion events of the trunk channel (Kraus, 2001). The heterolithic intervals, which consist of mudrocks and ribbon and thin sheet sandstones, alternate vertically with the overbank mudrocks, while major sheet sandstones locally truncate this stacking pattern (Fig. 2.2; Kraus, 2001). Paleosols formed concurrent with slow accumulation of overbank fines indicating stability of the main river channels. The cumulative nature of paleosol development meant that the overbank interval can include several vertically stacked paleosols and overprinted soil horizons (Abels et al., 2013). Subsequent avulsion of the main channels caused rapid accumulation of the heterolithic interval resulting in only weak or absent pedogenesis (Kraus, 2001).

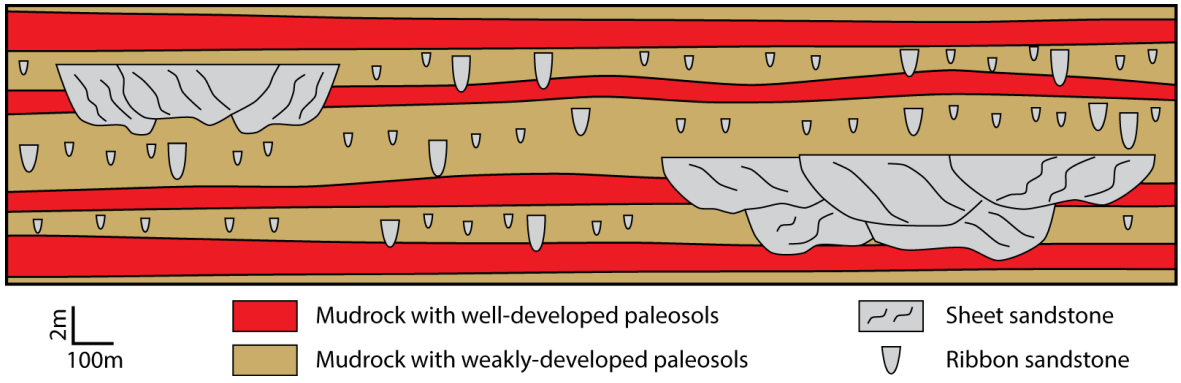

Figure 2.2 *- Schematic cross-section showing the three component architecture of Willwood Fm. floodplain deposits. Vertical exaggeration: 50x. From (Kraus, 2001).*

Pedogenesis of the overbank deposits is expressed by redoximorphic features, carbonate and iron concretions, rhizoliths and pedogenic slickensides (Kraus, 2001; Kraus and Hasiotis, 2006). Three types of paleosols are distinguished: 1) red paleosols, 2) purple paleosols and 3) purple/red paleosols. The dominant field characteristic of red paleosols is a B horizon rubified by pedogenic oxidation of hematite, whereas purple paleosols are defined by purple gleyed B horizons formed in high water table conditions (Kraus, 2001; Neasham and Vondra, 1972). Purple/red paleosols have characteristics of both and usually appear as purple/red couplets or red/purple/red sequences (Kraus, 2001). Willwood paleosols formed in a subtropical to tropical climate with a wet and dry season, allowing periodic oxidation in the red paleosols (Kraus, 2001). According to Kraus (2001), the main discriminating factors of soil wetness and thus the formation of different paleosol types on local and basin-wide scale were sedimentation rate and drainage (influenced by grain size of parent material, paleotopography and distance from main channel).

Volcanic material is present in the upper part of the Willwood Fm.: Pierce and Andrews (1941) reported a 2.4 m tuff in outcrops along the Absoraka margin; Bown (1982) mentioned probable tuffaceous mudstones in the Squaw Buttes area; and Rohrer (1964a, b) mapped a bentonite (his bed B) 60 m below the overlying Tatman Fm. in the Tatman Mountain area.

2.4 Tatman Formation

The Tatman Fm. (Sinclair and Granger, 1912; van Houten, 1944) overlies the Willwood Fm., but is only present in the central and southern Bighorn Basin as erosional remnants (Fig 1.1). It measures a maximum thickness of ~270m at Squaw Buttes Divide and ~210m at Tatman Mountain (Rohrer and Smith, 1969). The formation lies above a conformable contact and intertongues with the uppermost part of the Willwood Fm. (Bown T, 1980). The transition is marked by the striking disappearance of the periodic rubified paleosols and, consequently, the Tatman Fm. lacks carbonate nodules. Tatman strata consist of 3-24 m thick alternating units of grey, green, yellow and brown sandstone, mudrock and carbonaceous shales, deposited in lacustrine, palludial and fluvial settings, and yield a scarce vertebrate fossil record (van Houten, 1944; Bown, 1982; Gingerich and Clyde, 2001). Although Bown (1982) considered the Tatman Fm. non-tuffaceous compared to younger Tatman-like strata preserved in margins of the Absaroka and Southern Bighorn Mountains (Rohrer and Smith,

1969; Bown, 1982), Rohrer and Smith (1969) recorded several bentonitic units at Squaw Buttes Divide and Tatman Mountain.

3. Methods

3.1 Integrated stratigraphic approach

3.2.1 Sections and section correlation

During fieldwork, a new composite section of ~270 m was build spanning the uppermost part of the Willwood Fm. and the lower part of the Tatman Fm. The composite log consists of ten sections from two main sites: the Blackburn Gulch site and the Squaw Buttes site (Fig. 1.1; Table 3.1; Appendix XVIII). Tephra layers and other prominent strata (e.g. paleosols and carbonaceous shales) were used for section correlation (Fig. 3.1). The sections at Squaw Buttes site were connected using tephra layers SB-1 and SB-3 to SB-6 (layer SB-2 is a carbonaceous shale); these distinctive grey beds could be easily traced in the field. The Willwood ash is the most important correlative datum at the Blackburn Gulch site. The Willwood ash and SB-1 are the only tephras in the Willwood Fm. at their respective sites and were therefore presumed to be the same tephra layer. To test this, the tephra layers were traced on Google Earth Pro through which the distinctive outcrops in the virtually undeformed, sub-horizontal strata are easily detectable.

3.2.2 Logging and sampling

Sections were measured using a Jacob staff with Abney level, and beds were logged in detail after digging trenches in weathered surfaces to unearth fresh lithologies. Sections consisted of several trenches that could be easily correlated following individual sub-horizontal beds. The BBGU and SBU sections were mainly logged without digging trenches and thus based on (weathered) surface expression. Besides sedimentological and stratigraphic observations, presence and properties of soil morphological features (mottling, pedogenic slickensides and carbonate nodules) were recorded. A Munsell colour chart was used to assign colour codes to matrix and mottle colours of fresh rock surfaces.

Several types of samples were collected, always from fresh rock: tephra samples, paleomagnetic samples, colour reflectance measurements, bulk rock and carbonate nodules (Appendix III, XII and XVII); the latter two sample types were not further investigated in this study. Table 3.1 summarises the sample collection relevant for this study.

Blackburn Gulch site								
Section	**Code**	**Fm.**	**GPS location**	**Detailed log**	**Log length**	**Key tephra layers**	**Colour reflectance data**	**Pmag samples**
Fenton pass Road	FPR	Wi	44°15'38.17"N, 108°31'52.01"W	Yes	30 m	-	Yes; 10 cm resolution	Yes
Blackburn gulch Downward extension	BBGD	Wi	44°15'49.63"N, 108°32'57.52"W	Yes	41 m	Willwood Ash	Yes; 10 cm resolution	Yes
Blackburn Gulch	BBG	Wi, Ta	44°16'4.51"N, 108°33'57.37"W	Yes	56 m	Willwood Ash	Yes; 10 cm resolution	Yes*
Blackburn Gulch Upward extension	BBGU	Ta	44°15'57.66"N, 108°34'6.79"W	Mainly from surface expression	34.5 m	-	-	-
Squaw Buttes site								
Section	**Code**	**Fm.**	**GPS location**	**Detailed log**	**Log length**	**Key ash layers**	**Colour reflectance data**	**Pmag samples**
Squaw Buttes North Downward extension	SBND	Wi	44° 8'18.00"N, 108°40'24.14"W	Yes	15 m	SB-1	-	Yes
Squaw Buttes North	SBN	Wi	44° 8'18.00"N, 108°40'24.14"W	Yes	59.5 m	SB-1, SB-3	-	Yes
Squaw Buttes North Gap	SBN Gap	Wi, Ta	44° 8'28.96"N, 108°39'57.55"W	Yes	7 m	SB-3	-	Yes
Squaw Buttes South 1	SBS1	Wi, Ta	44° 6'32.70"N, 108°40'47.32"W	Yes	13.5 m	SB-3, SB-4	-	-
Squaw Buttes South 2	SBS2	Ta	44° 6'32.70"N, 108°40'47.32"W	Yes	37.5 m	SB-4, SB-5, SB-6	Yes; 30 cm resolution	Yes
Squaw Buttes South Upward extension	SBU	Ta	44° 6'19.83"N, 108°40'39.21"W	Mainly from surface expression	103 m	SB-6	-	Yes

Table 3.1 *- Sections and samples. * samples not analysed in this study. Wi = Willwood Fm., Ta = Tatman Fm., Pmag = paleomagnetic.*

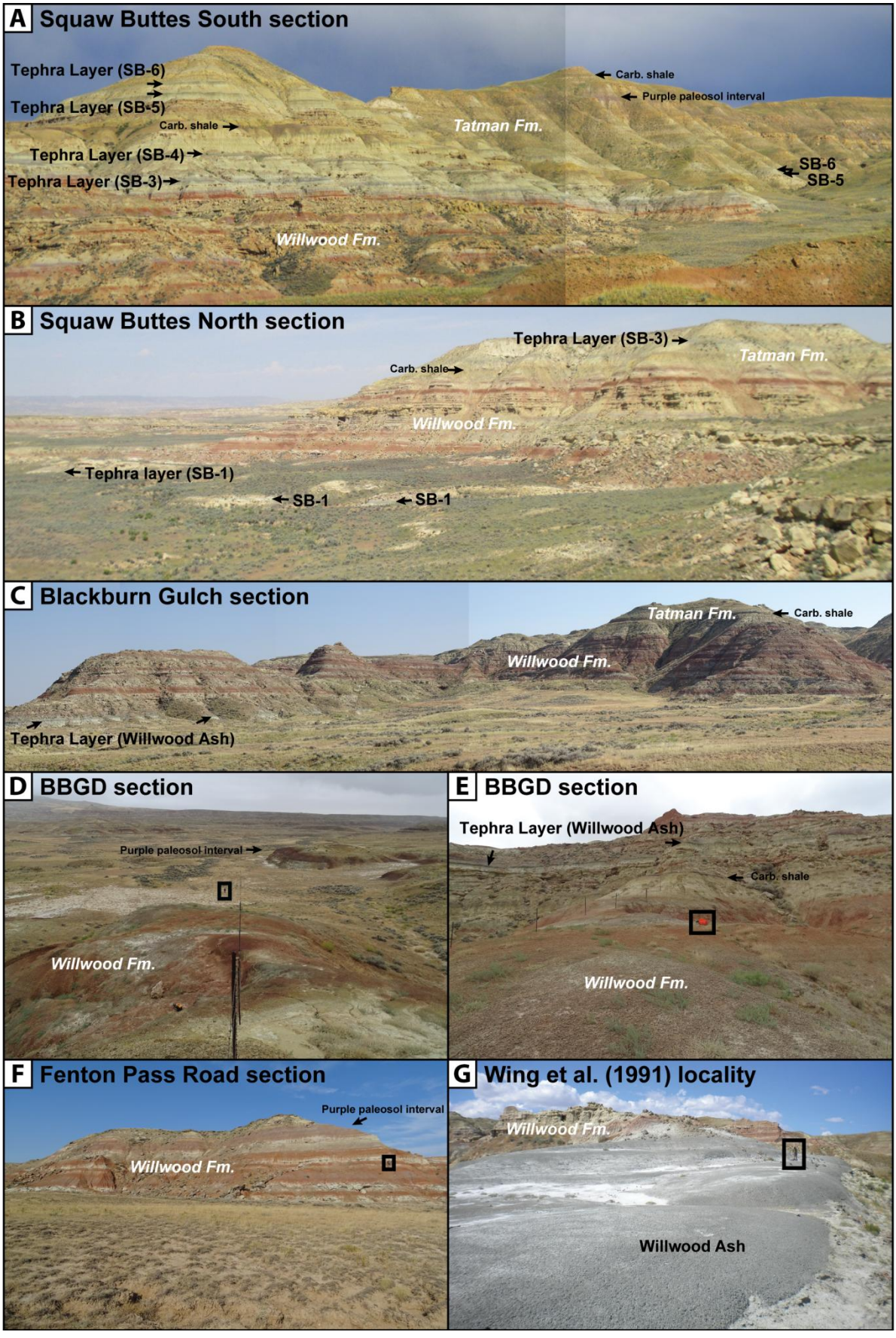
A Squaw Buttes South section
Tephra Layer (SB-6)
Tephra Layer (SB-5)
Carb. shale
Tephra Layer (SB-4)
Tephra Layer (SB-3)
Tatman Fm.
Carb. shale
Purple paleosol interval
SB-6
SB-5
Willwood Fm.
B Squaw Buttes North section
Tephra Layer (SB-3)
Tatman Fm.
Carb. shale
Willwood Fm.
Tephra layer (SB-1)
SB-1
SB-1
C Blackburn Gulch section
Tatman Fm.
Carb. shale
Willwood Fm.
Tephra Layer (Willwood Ash)
D BBGD section
Purple paleosol interval
Willwood Fm.
E BBGD section
Tephra Layer (Willwood Ash)
Carb. shale
Willwood Fm.
F Fenton Pass Road section
Purple paleosol interval
Willwood Fm.
G Wing et al. (1991) locality
Willwood Fm.
Willwood Ash

Figure 3.1 *- Field photos. Formations are indicated in white, stratigraphic elements in black. Carb. shale = carbonaceous shale.* ***A)*** *Squaw Buttes South section. The SBS2 section is logged on the left hill and the SBU section is logged on the right hill. For scale: stratigraphic height between SB-4 and SB-6 is 37 m in the SBS2 section. Stratigraphic height between SB-6 and the carbonaceous shale on the right is 94 m in the SBU section. Photo taken in ~SE direction.* ***B)*** *Squaw Buttes North section. The SBN section is logged on the left side of the hill and on hills behind. For scale: stratigraphic height between SB-1 and SB-3 is 57 m. Photo taken in ~NE direction.* ***C)*** *Blackburn Gulch section. The BBG section is logged on the left and right hills. BBGU is logged on the right side of the right hill. For scale: stratigraphic height between the Willwood Ash (BBG) and the carbonaceous shale (BBGU) is 65 m. Photo taken in ~SSW direction.* ***D)*** *Blackburn Gulch Downward extension. View on lower part of the BBGD section: indicated paleosol interval is at ~8 m stratigraphic height; paleosols on the foreground are at ~24 m. In the rectangle: person for scale. Photo taken in ~NEE direction from the carbonaceous shale on photo E.* ***E)*** *Blackburn Gulch Downward extension. View on upper part of the BBGD section: the carbonaceous shale is at ~29 m stratigraphic height. In the rectangle: backpack for scale. Photo taken in ~SSW direction.* ***F)*** *Fenton pass Road section. FPR is logged on this side of the hill. Purple paleosol interval is at ~20 m stratigraphic height. In the rectangle: person for scale. Photo taken in ~NE direction.* ***G)*** *Wing et al. (1991) locality. In the rectangle: person for scale. All photos taken by A. Turtù. Interpretation A, B and G adapted from A. Turtù (unpublished).*

3.2 $^{40}Ar/^{39}Ar$ geochronology

3.2.1 Samples and sample preparation

Tephra layers in the Willwood and Tatman Fm. contain sanidine crystal grains which are suitable for $^{40}Ar/^{39}Ar$ dating due to high potassium content. It is assumed that the age of these crystals represent the age of volcanic eruption and deposition of the tephra. Four tephras - the Willwood Ash/SB-1 (three samples), SB-3 (two samples), SB-4 and SB-5 - were selected for single grain total fusion dating (Table 3.2).

Ash sample	Sample location	Grain size	Irradiation and ID	Number of grains analysed				
				T007	T008	T011	T012	**Total**
SB1	Squaw Buttes North	> 250 µm	VU111-T15	30	8			38
SB3	Squaw Buttes South	200-250 µm	VU111-T16	30	8			38
SB4	Squaw Buttes South	125-250 µm	VU111-T17	30	8			38
SB5	Squaw Buttes South	200-250 µm	VU111-T18		38			38
WA-2017-1	Wing et al. (1991) locality	250-500 µm	VU112-T13			29	14	43
BBG-2017-1	Blackburn Gulch	250-500 µm	VU112-T14			30	14	44
SBN-2017-SB3	Squaw Buttes North	125-500 µm	VU112-T15			30	14	44

Table 3.2 *- Samples for $^{40}Ar/^{39}Ar$ dating. T007, T008, T011 and T012 represent different trays in which grains were loaded.*

Tephra layers were sampled by removing weathered surfaces and collecting fresh handpieces. Sanidine crystals were extracted from the handpieces in the mineral separation laboratory at VU Amsterdam. First step of the process (Fig. 3.2) was removing weathered parts from the handpieces using a pocketknife. If necessary, handpieces were reduced in size by a steel rock splitter. Before a new sample was treated, the rock splitter was cleaned with a vacuum cleaner, ethanol and compressed air. Next, the rock was crushed by a steel jaw crusher using a coarse (~1 cm) and a subsequent fine (~2 mm) jaw crusher opening. The jaw crusher was cleaned before use with a steel brush, vacuum cleaner, ethanol and compressed air.

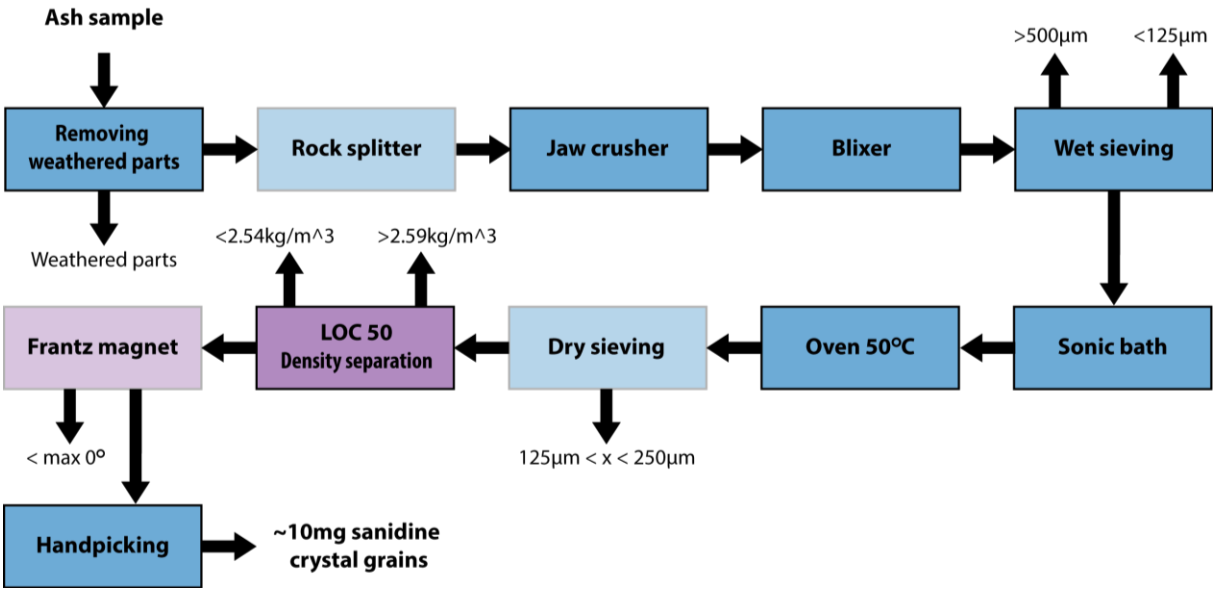

Figure 3.2 *- Workflow of sample preparation and mineral separation (for an example with target fraction 250-500 µm). In purple mineral separation steps. Light colour indicates steps that were applied to only a selection of the samples.*

Subsequently, fragments were further reduced in size by wet (tap water) grinding in a blixer for 5 minutes. The resulting crystal grains were wet sieved into fractions of >500 µm, 125-500 µm and <125 µm. Before use, the blixer was thoroughly cleaned with tap water. The sieves were cleaned by a 1 hour treatment in a sonic bath and with compressed air. The 125-500 µm target fraction was washed into a steel bowl and treated in a sonic bath to remove impurities attached to the surface of individual crystals. After 1 hour the bowl was taken out of the bath and the target fraction was given 1 minute to settle to the bottom. Then the water carrying very fine suspended material was drained off. Water was added and drained off two more times. The sonic bath treatment was repeated three or four times depending on the amount of released suspended material. Afterwards the remaining 125-500 µm fraction was dried overnight in an oven at 50 °C. Depending on the quality and quantity of the material, the sample was dry sieved to obtain the fractions specified in Table 3.2.

Target fractions were then subjected to density separation performed on a liquid overflow centrifuge, the LOC50, using mixtures of diiodomethane and dichlorobenzene as heavy liquid media. First a heavy liquid of 2.59 kg/m^3 was applied, so grains of lower density overflowed the centrifuge. Secondly, this 'float' was treated by a heavy liquid of 2.54 kg/m^3 and grains of

higher density sank in the centrifuge. The centrifuge and accompanying equipment to collect separates and filter heavy liquids from the separates were cleaned with acetone and compressed air in between centrifuge runs.

Although the 'float 2.59 sink 2.54' consisted mostly of sanidine, the quality of the crystals and amount of other grains varied per sample. Relatively dirty separates were further subjected to magnetic separation on a Frantz magnet. As sanidine has low magnetic susceptibility, the Frantz magnet separated clean sanidine crystals from dirty sanidine crystals and other grains of higher magnetic susceptibility. During the separation the magnet was set at maximum intensity, the inclination of the vibrating gutter along transport direction was set at 10° and the inclination between the dividing gutters was set at 0°. Before each separation, the gutter and accompanying equipment for introducing and collecting separates was cleaned by vacuum cleaner and compressed air.

~10 mg of the largest, most transparent and inclusion free sanidine crystals were collected from the final separates. The collection was done by handpicking under a microscope using a tiny vacuum cleaner: a little sample material was dispersed on a small tray to examine every single grain. The tiny vacuum cleaner was used to either remove undesired grains or collect target grains. Trays and vacuum cleaner were cleaned by compressed air before use.

3.2.2 Irradiation

Handpicked sanidine crystals of each sample were wrapped in 6 mm diameter aluminium packages. These packages were placed in aluminium cups together with packages of standards: Fish Canyon Tuff sanidine. The packages of standards and samples were evenly distributed over the cups so neutron flux could be monitored for all samples (Appendix II). The cups, placed in an aluminium vial, were irradiated in the TRIGA reactor Cadmium-Lined In-Core Irradiation Tube (CLICIT) at Oregon State University. Samples of this study were divided over two irradiation batches: VU111 and VU112 (Table 3.3). Batch VU111 was irradiated at 1MW power for a total of 12 hours in two segments on 6 and 7 December 2017. VU122 was irradiated for a total of 18 hours at 1MW in four segments divided over 6 to 8 March 2018.

Irradiation batch	Date	Power (MW)	Irradiation time (h)
VU111	6 -7 December 2017	1	12
VU112	6 - 8 March 2018	1	18

Table 3.3 *- Irradiation specifics.*

3.2.3 Loading

After irradiation the batches were put in storage for several months for radioactivity of short-lived isotopes, a by-product of irradiation, to decrease. Back at the VU, samples were taken from their aluminium packages and stored in plastic vials in the radioactive geochemistry laboratory. Samples of this study were divided over four tray runs on the mass spectrometer (Table 3.4). For each run, samples and accompanying standards were loaded in a copper tray with 185 holes; a single crystal was placed in each hole. The tray and sanidine crystals were only handled with gloves and tools cleaned with methanol. The loaded tray was heated to 250 °C under vacuum for at least 24 hours in a pre-bake apparatus to remove adsorbed atmospheric argon and other possible contaminants.

Tray run	Date
T007	27 July - 5 August 2018
T008	19 September - 28 September 2018
T011	24 October - 2 November 2018
T012	6 November - 14 November2018

Table 3.4 *- Dates of experiments on the Argus VI+.*

3.2.4 Mass spectrometry

$^{40}Ar/^{39}Ar$ analyses were performed on the Thermo Fisher Scientific Argus VI+ multi-collector mass spectrometer at the VU. The mass spectrometer and part of the extraction line are kept under ultrahigh vacuum, so before a loaded tray was placed in the extraction line, the sample house was closed off from the rest of the system. After placement, the copper ring sealing the lid of the sample house was replaced and the sample house was reconnected and ultrahigh-vacuum was restored. The sample house was subsequently baked at 120 °C for >12 hours. Meanwhile, the rest of the gas purification system was baked at 150 °C.

After baking, the mass spectrometer was prepared for operation by 1) evaluating background noise and 2) allocating the spectrometer's collectors. When the instrument is not pumped (measurement mode), degassing of the instrument causes an increasing

background noise. At the start of all four tray runs this static rise after 2 minutes did not exceed 3 fA (measured on collector H1). The Argus is equipped with an array of six collectors: four Faraday cups on the high mass positions and two compact discrete dynodes (CCDs) on the low mass side (Kuiper et al., 2018). The collectors were allocated to the different argon isotopes (^{40}Ar, ^{39}Ar, ^{38}Ar, ^{37}Ar, ^{36}Ar) in two configurations (jumps; Table 3.5). Two jumps were needed because the ^{37}Ar ion beam is not completely centred at collector L2 in the first configuration. To check for the exact position of the peak signals for the different isotopes, one sample in the tray was fused and its gas analysed. According to the signal peak centres, the collector array jump 1 and 2 positions for the run was set.

	H2 Faraday cup (10^{-12} amplifier)	**H1** Faraday cup (10^{-13} amplifier)	**Ax** Faraday cup (10^{-13} amplifier)	**L1** Faraday cup (10^{-13} amplifier)	**L2** CCD	**L3** CCD
Jump 1		^{40}Ar	^{39}Ar	^{38}Ar		^{36}Ar
Jump 2					^{37}Ar	

Table 3.5 *- Mass spectrometer collector allocation.*

A tray of samples and accompanying standards was analysed in an automated process spanning several consecutive days. A 25W CO_2 laser, operating at 40% power, heated an individual hole in the tray to fuse a single sanidine crystal in one step. Released sample gas was subsequently introduced to the gas preparation line where interfering volatiles were removed by a cold finger and three getter pumps. The cold finger (-70 °C) removed condensable gases such as H_2O, two NP10 getters (room temperature) adsorbed reactive gases such as H_2, and a NEG50 getter (400 °C) adsorbed heavier gasses such as N_2. The purified gas was then expanded into the mass spectrometer in static mode, ionised by electrons of ~70 eV and analysed for three minutes. Ultimately, the entire system was pumped preparing it for the next fusion.

In order to monitor background noise and bias between different detectors (mass discrimination) throughout a tray run, blanks and air shots were also analysed during an experiment. The following protocol was used: 1) before every two samples or standards, a blank was analysed; 2) after measurement of 18 samples or standards, two series (preceded

by air blanks) of two air shots were analysed; and 3) at the start and end of tray run, several series of blanks and air shots were analysed. Blank values are presented in Appendix IV.

3.2.5 Data reduction and age calculation

Raw data reduction and $^{40}Ar/^{39}Ar$ age calculations were performed using the ArArCalc 2.5.2 software (Koppers, 2002). The equations of Min et al., 2000 were used for the age calculations. The Fish Canyon Tuff sanidine standard (FCT) was assigned the age of 28.201 Ma ± 0.08% of Kuiper et al. (2008). Applied physical constants and correction factors for neutron interference reactions are listed in Table 3.6.

As mass spectrometer analyses were performed in static mode, static rise effected the measured intensities over the measurement interval. Therefore, raw intensity data for mass 36, 37, 38, 39 and 40 were regressed to determine the intercept value at the time of sample gas introduction. This regression was done for blanks, air shots, standards and samples by exponential regression unless scatter was too high and linear regression yielded a better fit. A maximum of three outliers were excluded from the regression if it yielded a better fit. After regression, polynomial fits were drawn for relevant blanks to determine the blank values of individual airshots, standards and samples: for airshots the polynomial fit was based on the blanks of the previous, current and next airshot sequence; for standards and samples on the blanks between two airshot sequences. Outliers were excluded from the polynomial fit.

The blank corrected air shots were used to determine the mass discrimination factor (MDF) of the mass spectrometer. The $^{40}Ar/^{36}Ar$ ratios of the air shots showed no trend throughout a tray run, so a weighted mean $^{40}Ar/^{36}Ar$ air ratio - weighted by the inverse of the variance - was calculated for every tray run. Outliers were excluded from the weighted mean, but a mean squared weighted deviation (MSWD) above 1 was accepted. From the $^{40}Ar/^{36}Ar$ weighted mean, the MDF was calculated applying a linear mass discrimination law. The MDF was applied in subsequent J-value and age calculations. The irradiation parameter 'J' was calculated for every standard using the assigned FCT age. From the combination of standards from relevant irradiation positions, a weighted mean J-value - weighted by the inverse of the

variance - was determined for every sample age calculation. Outliers and standards with $^{40}Ar^* < 95\%$ were left out of the weighted mean.

Age calculations of individual grains were carried out by applying the relevant MDF and J-value. To visualize the distribution of individual grains, a probability density distribution (PDD) was drawn from individual ages and 1σ error using AgeDisplay 1.0 software (Sircombe, 2004) with PDD increment set at 0.01 Myr. It is assumed that the tephra eruption age is represented by a normal distribution of individual ages, so the ash sample ages were determined by a mean weighted by the inverse of the variance, from which grains with $^{40}Ar^* < 95\%$ and outliers were excluded. A shapiro-Wilks normality test (Shapiro-Wilk Test Calculator, 2017) was conducted to test for normality of individual ages (right-tailed; 95% significance level).

Two types of error are used to describe uncertainty in the ash sample age results: internal error and external error. The first encompasses the analytical error and the error on the J-value; the latter also comprises the systematic errors as those on the decay constants and abundance ratios used for the age calculation (Koppers, 2002). The internal error is used for comparison of $^{40}Ar/^{39}Ar$ ages based on the same standard; the external error is used for absolute comparison to other $^{40}Ar/^{39}Ar$ ages and ages of independent dating techniques (Koppers, 2002). In this report ages are principally accompanied by their internal error. However, when external errors are presented additionally, an age is described in the following style: 'age' ± 'internal error'/'external error.' All errors are presented on the 2σ level.

Decay constants ± % 1σ		Source
^{40}K	5.53 x 10^{-10} ± 0.877% [yr^{-1}]	Min et al. (2000)
$^{40}K(ec, \beta^{+})$	5.8 x 10^{-11} ± 1.466% [yr^{-1}]	Min et al. (2000)
$^{40}K(\beta^{-})$	4.95 x 10^{-10} ± 0.869% [yr^{-1}]	Min et al. (2000)
^{39}Ar	2.94 x 10^{-7} ± 0.558% [h^{-1}]	ENDSF database
^{37}Ar	8.23 x 10^{-4} ± 0.143% [h^{-1}]	ENDSF database
^{36}Cl	2.257 x 10^{-6} ± 0.65% [yr^{-1}]	ENDSF database
Decay activities ± % 1σ		
$^{40}K(ec, \beta^{+})$	3.31 ± 1.209% [dps/g]	Min et al. (2000)
$^{40}K(\beta^{-})$	28.27 ± 0.177% [dps/g]	Min et al. (2000)
$^{36}Cl/^{38}Cl$ production ratio	262.8 ± 0.65%	Renne et al. (2008)
Other physical constants ± % 1σ		
Avogadro's number	6.0221367 x 10^{23} ± 0.000059% [mol^{-1}]	Cohen and Taylor (1988)
Atomic weight K	39.0983 ± 0.000154% [amu]	Min et al. (2000)
Seconds per year	31556930 [s]	Min et al. (2000)
$^{40}K/K$ ratio	0.000117 ± 0.855%	Min et al. (2000)
$^{35}Cl/^{37}Cl$ ratio	3.0866 ± 2%	n/a
HCl/Cl ratio	0.2 ± 20%	n/a
$^{40}Ar/^{36}Ar$ atmospheric ratio	295.5 ± 0.237%	Nier (1950)
Neutron interference corrections ± % 1σ		
$^{40}Ar/^{36}Ar$ trapped atmospheric	298.56 ± 0.104%	Lee et al. (2006)
$^{40}Ar/^{36}Ar$ cosmogenic	0.018 ± 35%	Lee et al. (2006)
$^{38}Ar/^{36}Ar$ trapped atmospheric	0.1885 ± 0.159%	Lee et al. (2006)
$(^{39}Ar/^{37}Ar)_{Ca}$	0.000673 ± 0.55%	Steenbrink et al. (1999)
$(^{36}Ar/^{37}Ar)_{Ca}$	0.000264 ± 0.64%	Steenbrink et al. (1999)
$(^{40}Ar/^{39}Ar)_{K}$	0.00086 ± 8.1%	Steenbrink et al. (1999)
$(^{38}Ar/^{39}Ar)_{K}$	0.01211 ± 0.25%	Lelieveldt (1995)
K/Ca ratio	0.43 ± 0%	Wijbrans et al. (1995)
Neutron fluence monitor age ± % 1σ		
Fish Canyon Tuff sanidine	28.201 Ma ± 0.08%	Kuiper et al. (2008)

Table 3.6 *- Constants, neutron interference corrections and FCT age applied in the $^{40}Ar/^{39}Ar$ age calculations.*

3.3 Magnetostratigraphy

3.3.1 Sampling and subsampling

Paleomagnetic samples were drilled from fresh rock surfaces using a hand-held water cooled drill with hollow drill bit of 2.5 cm diameter. These cores were oriented in situ using a Pomeroy orientation stage with compass. Azimuth and hade were noted and arrows pointing into the outcrop were carved on the side of the cores. Samples were then wrapped in aluminium foil to protect them during transport. As many silt and clay lithologies as possible were sampled while sand bodies were avoided. Effort was made to recover at least two samples per sample site. In total 419 samples from 151 sampling sites were collected resulting in an average sample site resolution of 2-3 m. At paleomagnetic laboratory Fort Hoofddijk at Utrecht University the samples were cut into (multiple) specimens of ~2 cm length using a circular saw. During the subsampling many specimens broke and had to be glued back together using a ceramic glue with negligible magnetic properties.

3.3.2 Thermomagnetic analysis

Ferro-/ferrimagnetic minerals have diagnostic Curie temperatures at which their saturation magnetization disappears. Therefore the analysis of sample magnetization as a function of temperature can be used to evaluate magnetic mineral content (e.g. Butler, 1992; McElhinny and McFadden, 2000). Seven specimens representing common lithologies (Table 3.7) were selected for this analysis. Thermomagnetic runs were carried out on a modified horizontal translation type Curie balance (Mullender et al., 1993) at Fort Hoofddijk.

Before each experiment, sample material was scraped off of the selected specimen and effort was made to reach fresh material. Material in the order of 10s of milligrams was put in a (diamagnetic) quartz glass sample holder, and glass wool was used to keep the material in place. The sample holder was attached to the translation arm and the assembly of the electromagnet and furnace was placed over the sample holder. The sample remained in contact with air.

During the experiment the sample was heated to 700 °C at a rate of 6 or 10 °C/min (Table 3.7). The heating mode was either linear or stepwise. In linear mode the sample was heated

continuously to 700 °C. In stepwise mode the sample was heated and partly cooled down 7 times before reaching the maximum temperature of 700 °C (Fig. 4.10). After reaching maximum temperature, all samples were cooled back to room temperature at a rate of 10 °C/min. The electromagnet applied a magnetic field cycling between 50 or 150 mT and 300 mT at a cycling frequency of 1.2 seconds during the heating and cooling. Due to the applied magnetic field the sample experienced a mechanical force related to the magnetic properties of the sample. Subsequent displacement of the translation arm was measured continuously by a sensor. The output signal of the sensor was smoothed by standard Savitzky-Golay filtering.

Although the cycling magnetic field (in contrast to a static field) provided the possibility to distinguish between ferro-/ferrimagnetic and paramagnetic components in the sample, only simple qualitative analysis of the output signal was performed. This had two reasons: 1) due to maintenance the output signal was not calibrated during experiments of this study and therefore it was not clear how the measurements related to the noise level of the Curie balance. 2) It was unknown if the applied magnetic field was enough to saturate the ferro-/ferrimagnetic components in the samples which is needed for the separation of the ferro-/ferrimagnetic and paramagnetic components.

Lithology	Formation	Specimen	Mass (mg)	Heating mode	Heating rate (°C/min)	Magnetic field cycling (mT)
Olive grey very fine sandstone	Tatman	FH_1.1	47.23	Linear	6	50-300
Grey paleosol	Tatman	FH_5.2	42.33	Linear	10	50-300
Dark red paleosol (orange and greenish mottling)	Willwood	SBN_16.3	48.89	Stepwise	6	50-300
Purple paleosol (Greenish/grey mottling)	Willwood	SBN_14.1	45.05	Stepwise	6	50-300
Yellowish brown fine sandstone	Tatman	FH_39.2	37.69	Linear	10	50-300
Olive grey siltstone	Tatman	FH_14.2b	39.76	Linear	6	50-300
Dull brown fine sandstone	Tatman	FH_9.1b	38.53	Stepwise	6	150-300

Table 3.7 *- Thermomagnetic samples and experimental procedures.*

3.3.3 Paleomagnetic measurements and demagnetization

168 specimens from 109 sampling sites were selected for two methods of partial demagnetization: 56 specimens from the SBN, SBN gap and SBS2 sections were subjected to alternating field (AF) demagnetization and 112 specimens from the FPR, BBGD, SBND, SBN,

SBN gap and SBU sections were processed by thermal (TH) demagnetization; both carried out at Fort Hoofddijk.

AF demagnetization and magnetization measurement were carried out on an in-house built robotized 2G Enterprise horizontal DC-SQUID magnetometer with in-line AF acquisition (Mullender et al., 2016) stationed in a shielded room. Specimens were put in cube perspex holders and held in place by silicon kit. These cubes were cleaned beforehand with water and soap. The holders containing specimens were placed in the loading tray and the automated process was started. Natural remnant magnetization (NRM) of each specimen was measured at the start of the process. Thereafter the specimens were AF demagnetized in steps from 4 to 100 mT (Table 3.8). After each step the remnant magnetization was measured. The magnetometer has a noise level of 10^{-12} Am^2 (10^{-7}A/m translated to sample magnetization) and the perspex holders have a magnetization of 1-2 x 10^{-6}A/m (Mullender et al., 2016). This is two or three orders of magnitude lower than the typical NRM of the specimens.

TH demagnetization was applied by heating specimens in a shielded furnace at progressive steps from 80 to maximum 650 °C (Table 3.8). Linger time at target temperature was set at 35 minutes. Before specimens were put in the furnace the sample holder was cleaned with ethanol. Each heating step ~28 specimens at a time were positioned on the holder in a direction 180° to their direction in the previous heating step. This was done to minimise the remagnetizing effect of possible magnetic fields within the oven.

Specimen magnetisation was measured before the first heating step and after each heating step on a shielded 2G Enterprises DC SQUID magnetometer with a noise level of 3 x 10^{-12} Am^2. The measurements were done manually. The range was set at 1 and the number of SQUID readings was set at 3. Before a group of specimens was measured, the glass sample holder of the magnetometer was cleaned with ethanol. A cohesive tape was attached to the holder to keep specimens in place. The empty sample holder with strip of tape was measured and found acceptable if the value was less than 50 x 10^{-12} Am^2. When the sample holder or tape became visibly dirty, the holder was cleaned again and the tape was replaced.

During analysis a specimen was placed on the sample holder with the down-core side pointing to the magnetometer. The holder was then inserted into the magnetometer and the measurement was started after the instrument was given 20-30 seconds to stabilise. The measurement was accepted if the difference between blanks measured at insertion and withdrawal of the sample holder was less than 0.05% and if the circular standard deviation (CSD) was less than 10°. Otherwise measurement was repeated. If a specimen showed chaotic behaviour during several subsequent demagnetization steps, it was taken out of the heating and measuring procedure. Specimens standing by for measurement or heating were stored in a zero-field shield.

AF demagnetization			TH demagnetization	
Step	Magnetic field (mT)		Step	Temperature (°C)
1	0 (untreated)		1	20 (unheated)
2	4		2	80
3	8		3	100
4	12		4	120
5	16		5	150
6	20		6	175
7	25		7	200
8	30		8	225
9	35		9	250
10	40		10	275
11	45		11	300
12	50		12	325
13	60		13	350
14	70		14	375
15	80		15	400
16	90		16	425
17	100		17	450
			18	475
			19	500
			20	520
			21	540
			22	560
			23	580
			24	600
			25	625
			26	650

Table 3.8 *- Steps in the AF and TH demagnetization.*

3.3.4 ChRM identification

Demagnetisation data was interpreted using Remasoft 3.2 software (Chadima and Hrouda, 2006) to determine specimen characteristic remnant magnetisation (ChRM). Data was plotted on orthogonal projections, or Zijderveld diagrams (Zijderveld, 1967), and equal area projections along with intensity diagrams. Most specimens showed magnetic components of low stability (<200 °C or <20 mT) which were considered overprinted directions. If specimens carried more components, the highest stability component was established as ChRM by principal component analysis (PCA; Kirschvink, 1980) or by calculating a Fisher mean (Fisher, 1953). PCA was carried out when at least four consecutive vector end points displayed a clear trend (approximately) to the origin. The origin was only included as data point in the calculation if the origin was clearly part of the trend. A Fisher mean was calculated when at least three consecutive vector end points showed clustering. Resulting ChRM directions were accepted if mean angular deviation (MAD) was less than 25°. Non-linear demagnetisation along a great circle path was recognised, but great circles were not used to establish ChRMs.

3.4 Cyclostratigraphy

3.4.1 Colour reflectance measurements

Colour reflectance measurements were taken from the FPR, BBGD, BBG (Willwood Fm.) and SBS2 (Tatman Fm.) sections at a vertical resolution of 10 or 30 cm (Table 3.1) using a Minolta CM 600d portable photospectrometer. Measurements were obtained from fresh rock surfaces of typical colour (matrix colour) for the specific stratigraphic level, either directly from the trench or from broken-off pieces. Effort was made to measure from flat rock surfaces and to keep the photospectrometer in the shadow during measurement to minimise sunlight entering the apparatus. At each stratigraphic level, two consecutive measurements of the same rock surface were carried out; at the SBS2 section one with specular component excluded (SCE) and the other with specular component included (SCI).

The Minolta illuminated a sample area of 8 mm diameter (D65 set as illuminant) and measured the reflected light. The value of each measurement is based on the automatically calculated average of three analyses. Reflectance was recorded in L*a*b* colour space (CIELAB), where L* expresses lightness, a* green to red and b* blue to yellow (Mokrzycki and Tatol, 2009). At the start of a series of measurements, zero calibration (photospectrometer aimed at the sky) and white calibration (white calibration cap attached) were performed.

3.4.2 Soil development index

Based on soil horizon characterization of Kraus and Hasiotis (2006) and Abels et al. (2013), paleosol profiles were recognised from the logs of the FPR, BBGD and BBG sections. To quantify the magnitude of pedogenesis for these profiles a soil development index was used following the method of Abels et al. (2013). The soil development index (SDI) consist of three parameters: B-horizon thickness and rubification, and intensity of horizon development; these were quantified according to Table 3.9 and standardised by two standard deviations of all values of the three sections. The standardized parameters were then averaged and 1 was added (Appendix XVII). The resulting SDI categorises stratigraphic units in: no (SDI = 0), incipient (SDI 0 - 0.5), intermediate (SDI 0.5 - 1) and intense (SDI >1) pedogenesis.

B-horizon thickness		B-horizon rubification		Intensity of horizon development	
Thickness (m)	Thickness index	Hue	Hue index	Horizon development	Horizon index
0.00 - 0.20	0.0	5R/5RP	1.00	Incipient *Discontinuous colouring/little horizon differentiation*	0
0.20 - 0.35	0.1	7.5R	0.85		
0.35 - 0.50	0.2	10R	0.70	Poor *Vague horizons; small slickensides and mottles*	1
0.50 - 0.65	0.3	2.5YR	0.55		
0.65 - 0.80	0.4	5YR	0.40	Intermediate *Clear horizons; slickensides, mottles (and nodules).*	2
0.80 - 0.95	0.5	7.5YR	0.25		
0.95 - 1.10	0.6	10YR	0.10	Well *Strong horizon differentiation; large and abundant slickensides, mottling (and nodules).*	3
1.10 - 1.25	0.7				
1.25 - 1.40	0.8				
1.40 - 1.55	0.9				
>1.55	1.0				

Table 3.9 *- Quantification of SDI parameters.*

3.4.3 Grain size index

In contrast to the Willwood Fm., the Tatman Fm. contains few paleosols, so differentiation of pedogenesis - and, therefore, the SDI - is not a useful measure to specify cyclicity in the SBS2 section. To quantify lithological variability of this section a simple grain size index was adopted: a value based on lithology (Table 3.10) was assigned at 30 cm vertical resolution. These values were subsequently standardised by two standard deviations of the total and added to 1 (Appendix XVII) to produce a grain size index (GSI) which classifies carbonaceous shales (GSI < 0), mudrock (GSI 0 - 1) and sandstone (GSI > 1).

Lithology	Lithology index
Coal	0.0
Carbonaceous shale	0.5
Clay	1.0
Mud	1.5
Silt	2.0
Very fine sandstone	2.5
Fine sandstone	3.0
Medium sandstone	3.5
Coarse sandstone	4.0

Table 3.10 *- Quantification of lithology for the GSI (following Noorbergen et al., 2018).*

3.4.4 Spectral analysis

Duplicate colour measurements of the FPR, BBGD and BBG sections differed typically less than 1% of total record range (exceptions <15%), so duplicate measurements were averaged (using Acycle 2.2; Li et al., 2019). Difference between the SCE and SCI records of the SBS2

section was negligible, so only the SCE colour records were taken for further processing. Stratigraphic logs and, consequently, colour records and SDI of the FPR, BBGD and BBG sections were combined in a composite section (Blackburn Gulch composite). The SDI record was resampled at 10 cm resolution.

Time-series analysis of the selected colour reflectance data, SDI and GSI was performed using Acycle 2.2 sofware (Li et al., 2019). Firstly, long-term trends were removed from records with high power low-frequency variability using a rLOESS detrending model. The sliding window was chosen to reveal most frequency components in subsequent spectral analysis; Table 3.11 shows selected sliding windows for all records. Detrended records were spectrally analysed applying a 2π multi-taper method with zero-padding while background noise was estimated using a classic AR(1) red noise model (Husson, 2014 with corrections by L.A. Hinnov).

3.4.5 Bandpass filtering

Abdul Aziz et al. (2008), Abels et al. (2012, 2013, 2016), Westerhold et al. (2018) and van der Meulen et al. (2020) linked ~21 kyr precession to cyclicity of ~7 m period in the northern Bighorn Basin Willwood Fm. Clyde et al. (2007) concluded that subsidence rates in the period of 60-53 Ma in the central part of the Bighorn Basin were half of the rate in the northern part of the basin. Preliminary $^{40}Ar/^{39}Ar$ results of this study indicated a sedimentation rate which would result in ~21 kyr precession corresponding to periods of 3-6 m. Therefore, dominant periodicities of 3-10 m revealed by spectral analysis of the SDI, GSI and detrended colour records were extracted using Gaussian bandpass filters (Kodema and Hinnov, 2014). Settings for bandpass centre and bandwidth are listed in Table 3.11.

Blackburn Gulch composite						
Record	**Detrending model**	**Gaussian bandpass filtering**				
		#	Centre (frequency)	Bandwidth (frequency)	Centre (period)	Bandwidth (period)
SDI	-	1	0.11	0.020	9.09m	7.69-11.11m
		2	0.1546	0.025	6.47m	5.57-7.72m
		3	0.22	0.020	4.55m	4.17-5.00m
L*	60m-rLOESS	4	0.1092	0.022	9.16m	7.62-11.47m
		5	0.183	0.020	5.46m	4.93-6.13m
		6	0.2269	0.015	4.41m	4.13-4.72m
a*	50m-rLOES	7	0.1361	0.030	7.35m	6.02-9.43m
		8	0.23	0.014	4.35m	4.10-4.63m
b*	60m-rLOES		-			
Squaw Buttes South 2 (SBS2)						
Record	**Detrending model**	**Gaussian bandpass filtering**				
		#	Centre (frequency)	Bandwidth (frequency)	Centre (period)	Bandwidth (period)
GSI	-	1	0.155	0.035	6.45m	5.26-8.33m
L*	20m-rLOES	2	0.1084	0.021	9.23m	7.73-11.44m
		3	0.173	0.028	5.78m	4.98-6.90m
a*	15m-rLOES	4	0.11	0.030	9.09m	7.14-12.5m
b*	30m-rLOES	5	0.12	0.030	8.33m	6.67-11.11m

Table 3.11 *- Colour reflectance, SDI and GSI detrending models and bandpass filters.*

4. Results

4.1 Stratigraphy and sedimentology

4.1.1 Tephra description and stratigraphy

Two types of tephra layers were encountered: bentonites and thin granular layers. Bentonites are laterally continuous, decimetre to metre scale thick sandy clay beds with a sharp base. The sandy part consists of crystal grains, including biotite and feldspar, with a fine to medium grain size. The amount and size of the crystal grains decrease to the top. Fresh rock has an olive grey colour, but bentonites have a typical (light) grey 'popcorn-like' weathered surface that stands out from other lithologies of the Willwood and Tatman Fm. (Fig. 3.1G and 4.2). Thin granular tephras are cm-scale thick, sharply bounded, pinkish or yellowish layers of fine to coarse crystal grains and were only found in some carbonaceous shales of the Tatman Fm. (see logs in Appendix I).

The important tephras Willwood Ash, SB-1 and SB-3 to SB-6 are all bentonites. Tracing on Google Earth Pro showed that SB-1 connects to the tephra at the Wing et al. (1991) locality (Fig. 4.2), but the bentonite is not present in the valley between the Wing et al. (1991) locality and the Blackburn Gulch site. However the bentonites at both Squaw Buttes and Blackburn Gulch have a similar appearance and stratigraphic position approximately 55 m below the Willwood-Tatman boundary, so the bentonites at both sites are considered the same tephra (see Discussion). Tatman Fm. tephras SB-3 to SB-6 at Squaw Buttes could not be connected one-to-one to Tatman Fm. bentonites found at Blackburn Gulch. Tephra stratigraphy and resulting section correlation is displayed in Fig. 4.3.

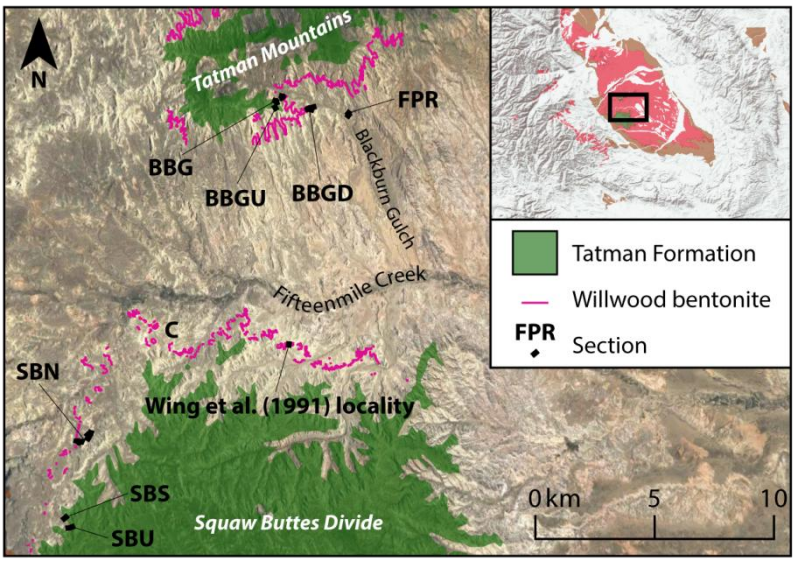

Figure 4.1 *- Study area showing the traced Willwood Ash/SB-1 and logged sections. Geological map of the Tatman Fm. (USGS) overlies Google satellite map. Inset is simplification of Fig. 1.1. Bentonite trace around Tatman Mountains is drawn from Rohrer (1964a, b; his bed B). Trace around Squaw Buttes Divide is adapted from A. Turtù (unpublished). C indicates location of Fig. 4.2C. Section abbreviations explained in Table 3.1.*

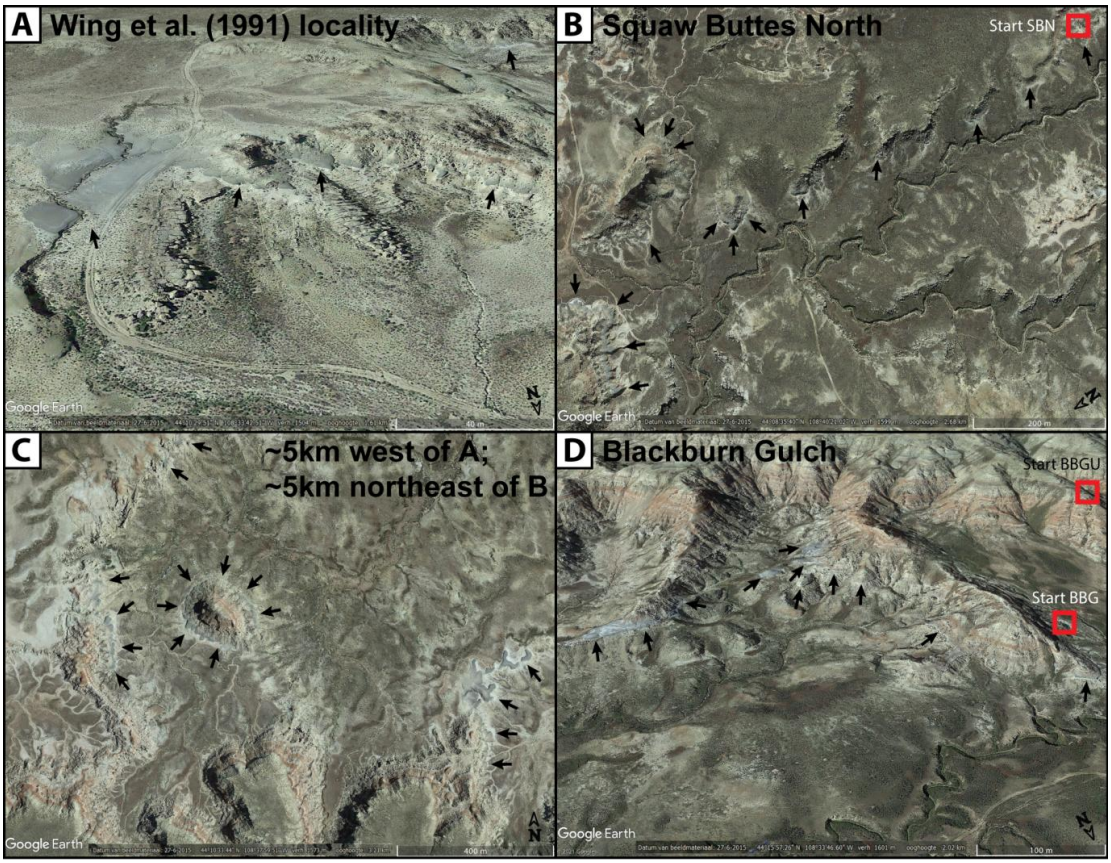

Figure 4.2 *- Examples of tephra tracing in Google Earth Pro. Arrows indicate tephra outcrops in the Willwood Fm.* ***A)*** *Willwood Ash locality sampled by Wing et al. (1991) and this study (sample WA-2017-1).* ***B)*** *Map view of SB-1 near the start of the SBN section.* ***C)*** *Map view of tephra outcrops in between the Wing et al. (1991) locality and SB-1. Exact location in Fig. 4.1.* ***D)*** *Bed B of Rohrer (1964a, b) near the start of the Blackburn Gulch section. The Blackburn Gulch Upward section (BBGU) marks the Willwood-Tatman Fm. boundary.*

4.1.2 Lithostratigraphic logs

A generalised overview of the stratigraphy and correlation of the composite section is given in Fig. 4.3. Detailed logs are presented in Appendix I.

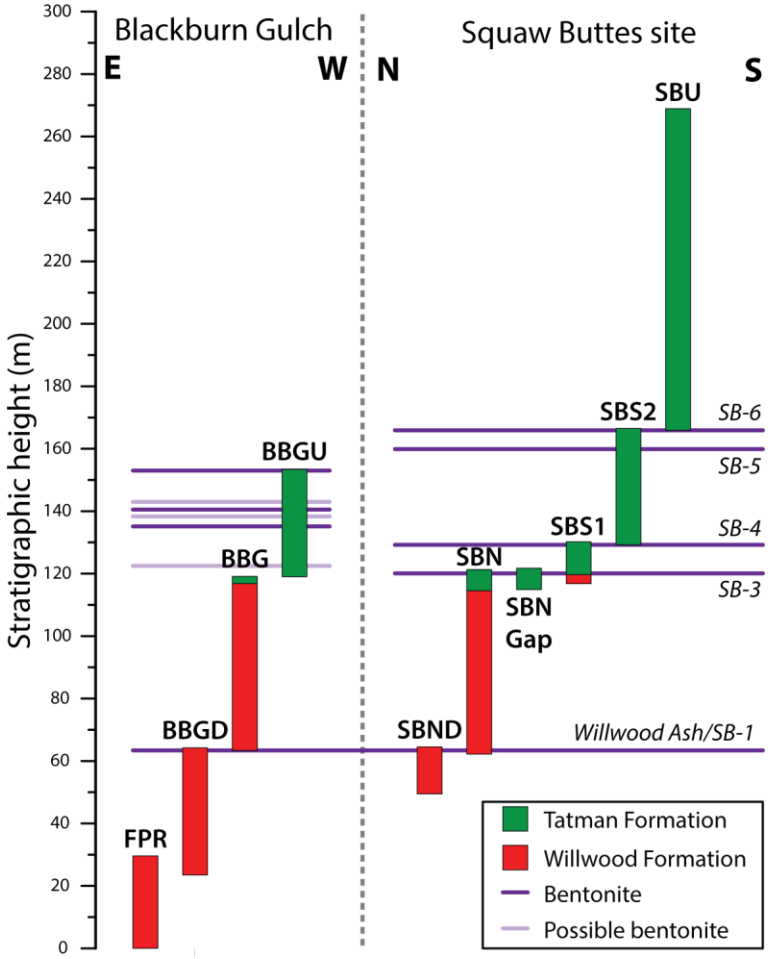

Figure 4.3 *- Generalised overview of the composite section showing stratigraphic positions of sections and bentonites. Bentonites used for section correlation are named. Section abbreviations in Table 3.1.*

4.2 $^{40}Ar/^{39}Ar$ geochronology

4.2.1 Mass discrimination factors

$^{40}Ar/^{36}Ar$ ratios of individual air shots showed no trend within the four tray runs, but varied between 312 and 320. Fig. 4.4 shows the air shots per experiment in increasing $^{40}Ar/^{36}Ar$ order and illustrates the weighted means. The MDFs, calculated from these weighted mean $^{40}Ar/^{36}Ar$ ratios, are presented in Table 4.1.

4.2.2 J-values

Three sets of standards from relevant irradiations positions were used to determine the weighted mean J-values for the age calculations (Table 4.1; Fig. 4.5).

Samples (irradiation)	Tray run	$^{40}Ar/^{36}Ar$ air ratio ± 2σ	MDF ± 2σ	Relevant standards (irradiation)	J-value ± 2σ
SB1, SB3, SB4 (VU111)	T007	314.61 ± 0.17 (0.05%)	0.984792 ± 0.001144 (0.12%)	S10, S11, S13, S14 (VU111)	0.0030984 ± 0.0000020 (0.07%)
	T008	315.27 ± 0.29 (0.09%)	0.984299 ± 0.001194 (0.12%)		
SB5 (VU111)	T008	315.27 ± 0.29 (0.09%)	0.984299 ± 0.001194 (0.12%)	S6, S7, S8, S15, S16 (VU111)	0.0030780 ± 0.0000017 (0.06%)
WA-2017-1, BBG-2017-1, SBN-2017-SB3 (VU112)	T011	317.08 ± 0.29 (0.09%)	0.982961 ± 0.001187 (0.12%)	F8, F9, F10, F11, F12, F13, F14 (VU112)	0.0046053 ± 0.0000020 (0.04%)
	T012	317.25 ± 0.27 (0.09%)	0.982835 ± 0.001175 (0.12%)		

Table 4.1 *- Overview of mass discrimination factors and J-values.*

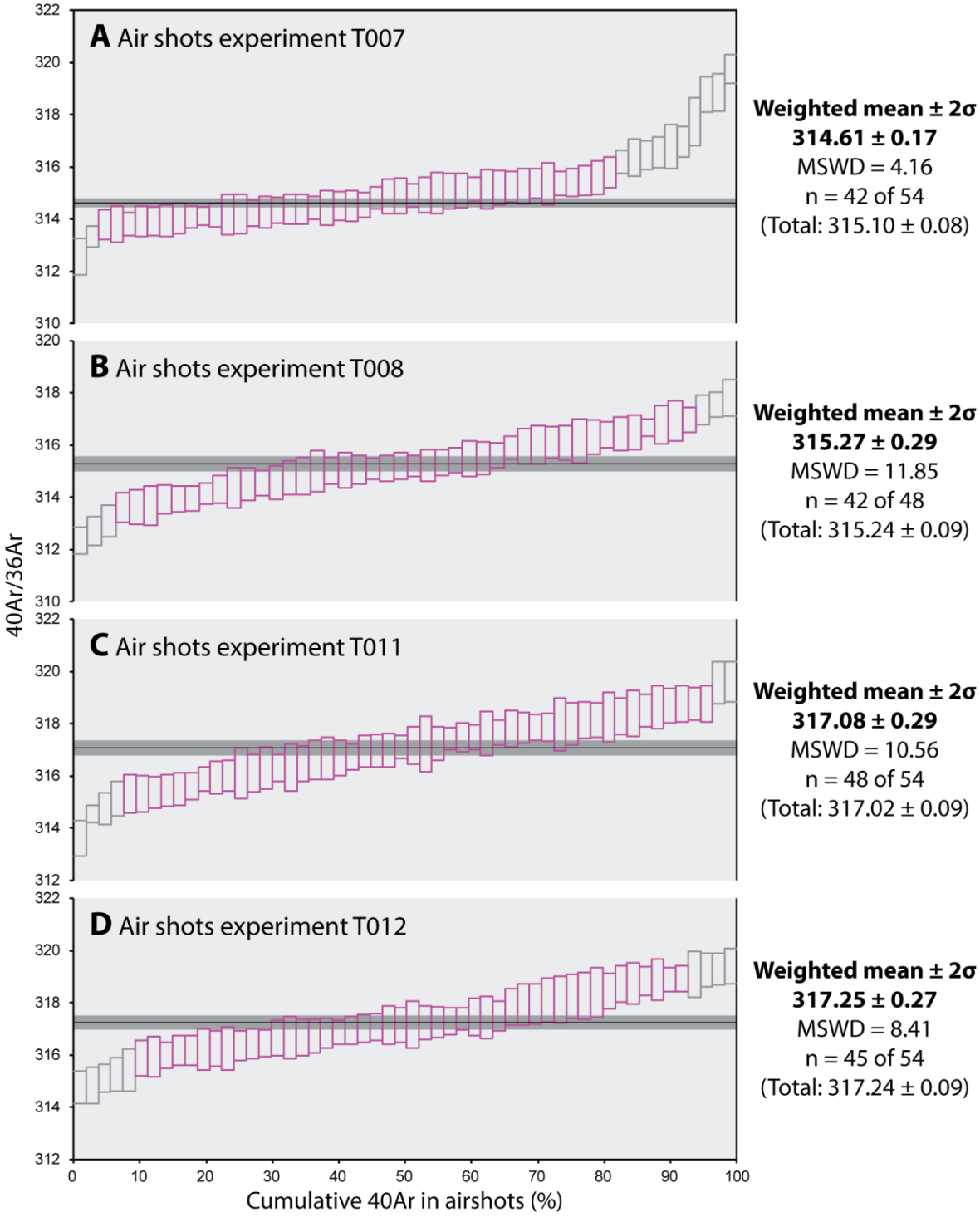

Figure 4.4 *- Air shot $^{40}Ar/^{36}Ar$ values and weighted mean per tray run. Air shots are displayed as boxes representing 2σ error and are sorted by $^{40}Ar/^{36}Ar$ ratio. Air shots depicted in pink are included in the calculation of the $^{40}Ar/^{36}Ar$ weighted mean which is illustrated by the black line with dark grey 2σ uncertainty. Next to the graph the weighted mean, the MSWD, number of included air shots and the mean of all air shots (with 2σ error) are stated.*

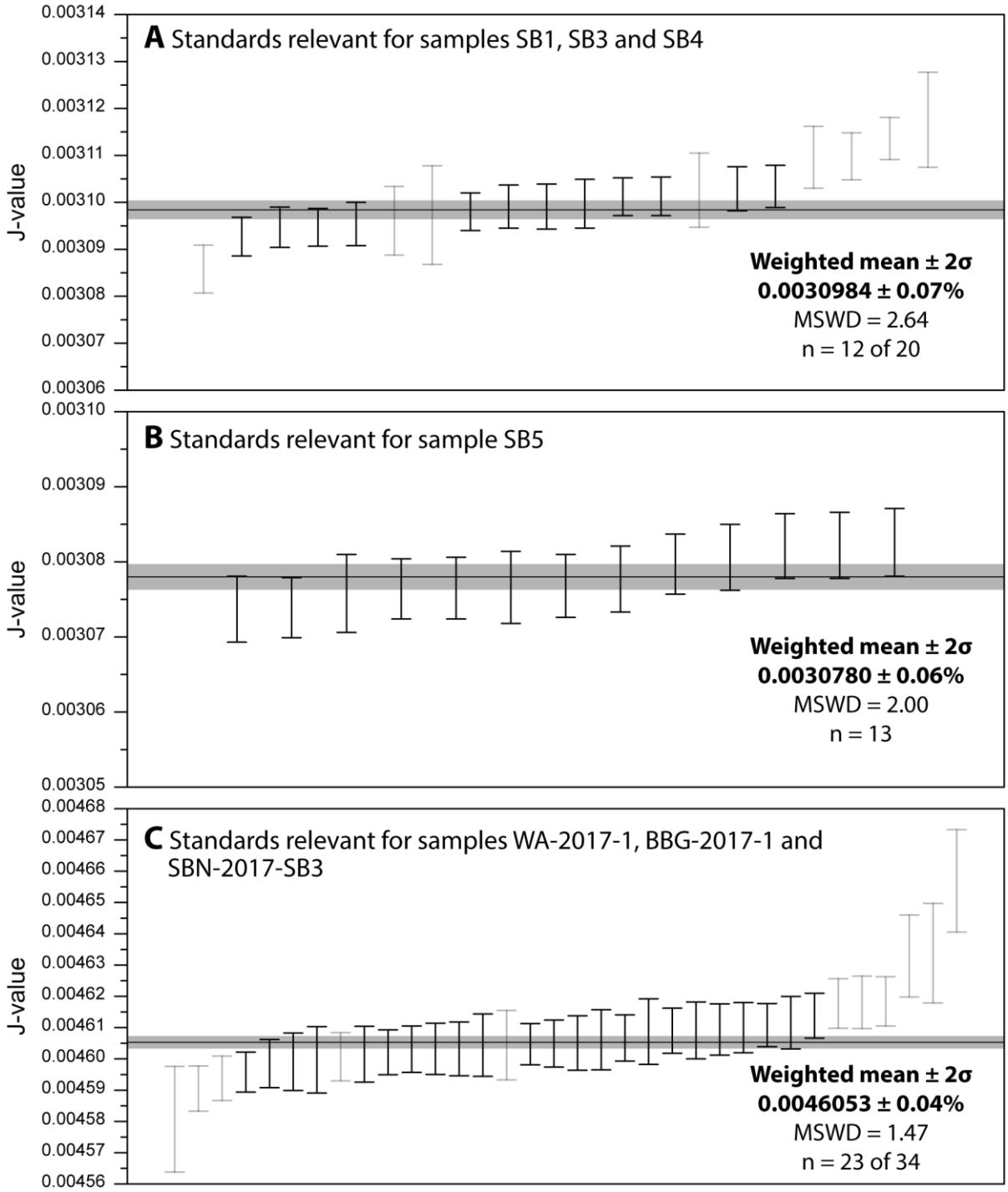

Figure 4.5 *- J-values of individual FCT standards. Each crystal is represented by a 2σ error bar; faded bars are excluded from the calculation of the weighted mean J-value (either outlier or* $^{40}Ar^{*} < 95\%$*). The weighted mean is shown as the horizontal line with grey 2σ uncertainty interval. In the lower right corner the weighted mean, the MSWD and number of included standards are stated.*

4.2.3 Date Willwood Ash/SB-1

Three tephra samples of the Willwood Ash/SB-1 were dated: WA-2017-1, BBG-2017-1 and SB1 (Fig. 4.6; Table 4.2). WA-2017-1 has a weighted mean age of **52.43 ± 0.03/0.86 Ma** (MSWD = 1.83; n = 42). The individual dates range from 52.32 ± 0.07 Ma to 52.66 ± 0.08 Ma; the included ages follow a normal distribution (p-value = 0.339; skewness = 0.266; W statistic = 0.970). The weighted mean age of BBG-2017-1 is **52.54 ± 0.03/0.86 Ma** (MSWD = 2.67; n = 43). Individual ages have a range from 52.40 ± 0.09 Ma to 52.67 ± 0.09 Ma and the included ages describe a normal distribution (p-value = 0.212; skewness = -0.146; W statistic = 0.965). SB1 has a weighted mean age of **52.52 ± 0.04/0.86 Ma** (MSWD = 1.55; n = 32). Individual ages range from 52.42 ± 0.08 to 52.72 ± 0.11; included ages follow a normal distribution (p-value = 0.819; skewness = 0.045; W statistic = 0.981). The inverse isochron intercepts of all three ash samples are in agreement with the atmospheric ratio on the 2σ level. Full analytical data in Appendix V, VI and VII.

Tephra Willwood Ash/SB-1	**Weighted mean age (Ma)**	**Internal error (2σ)**	**External error (2σ)**
SB1	52.52	0.04 (0.07%)	0.86
WA-2017-1	52.43	0.03 (0.05%)	0.86
BBG-2017-1	52.54	0.03 (0.06%)	0.86
Tephra SB-3	**Weighted mean age (Ma)**	**Internal error (2σ)**	**External error (2σ)**
SB3	52.20	0.04 (0.07%)	0.85
SBN-2017-SB3	52.20	0.03 (0.05%)	0.85
Tephra SB-4	**Weighted mean age (Ma)**	**Internal error (2σ)**	**External error (2σ)**
SB4	52.08	0.04 (0.09%)	0.85
Tephra SB-5	**Weighted mean age (Ma)**	**Internal error (2σ)**	**External error (2σ)**
SB5	51.94	0.09 (0.18%)	0.85

Table 4.2 *- Summary of $^{40}Ar/^{39}Ar$ ages.*

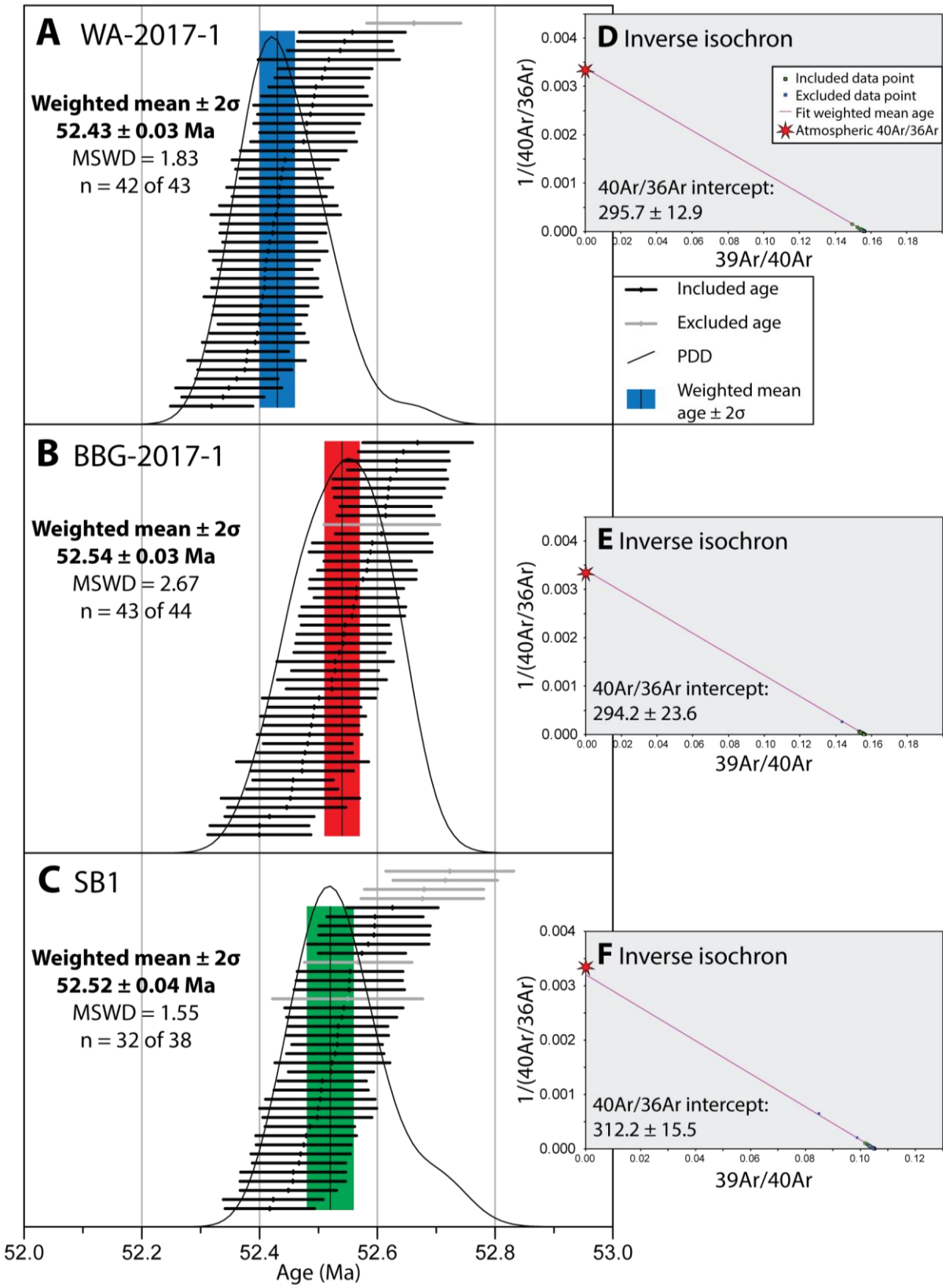

Figure 4.6 *- $^{40}Ar/^{39}Ar$ results of the Willwood Ash/SB-1 for ash samples WA-2017-1* ***(A)****, BBG-2017-1* ***(B)*** *and SB1* ***(C)****. Ages of individual grains are represented by bars on the 2σ level; grey bars are excluded from the calculation of the weighted mean age (either outlier or $^{40}Ar^{*}$ <*

95%). PDD's are based on both included and excluded individual ages; y-axis is relative probability. The weighted mean age is represented by a coloured bar on the 2σ level and stated with the MSWD and number of included individual ages. ***D, E, F)*** *Inverse isochrons of data in A, B and C. The atmospheric* $^{40}Ar/^{36}Ar$ *composition of 298.56 (Lee et al., 2006) is indicated by a red asterisk. The inverse isochron intercept - translated to* $^{40}Ar/^{36}Ar$ *- is stated in the lower left corner of the graph.*

4.2.4 Date SB-3

The two ash samples of tephra SB-3 yielded the same weighted mean age: **52.20 ± 0.04/0.85 Ma** (MSWD = 1.87; n = 37) for SB3 and **52.20 ± 0.03/0.85 Ma** (MSWD = 1.16; n = 39) for SBN-2017-SB3 (Fig. 4.7; Table 4.2). The individual ages of SB3 range from 52.01 ± 0.13 Ma to 52.38 ± 0.10 Ma and the included ages are normally distributed (p-value = 0.124; skewness = -0.456; W statistic = 0.953). Total range of SBN-2017-SB3 is 52.02 ± 0.10 Ma to 52.48 ± 0.10 Ma; the included ages follow a normal distribution (p-value = 0.134; skewness = 0.130; W statistic = 0.956). The intercept of the inverse isochron of both samples overlap with the atmospheric ratio. Full analytical data in Appendix VIII and IX.

4.2.5 Date SB-4

Ash sample SB4 yielded a weighted mean age of **52.08 ± 0.04/0.85 Ma** (MSWD = 2.48; n = 30; Fig. 4.8; Table 4.2). Individual ages range from 51.73 ± 0.18 Ma to 52.33 ± 0.12 Ma; included grains are normally distributed (p-value = 0.174; skewness = 0.305; W statistic = 0.951). The inverse isochron implies an $^{40}Ar/^{36}Ar$ intercept that overlaps with the atmospheric ratio. Full analytical data in Appendix X.

4.2.6 Date SB-5

The weighted mean age of sample SB-5 is **51.94 ± 0.09/0.85 Ma** (MSWD = 3.64; n = 14; Fig. 4.9; Table 4.2). The total range of individual dates is more extensive compared to the other ash samples: 2.16 ± 21.68 Ma to 925.70 ± 1.64 Ma. Majority of extreme outliers have $^{40}Ar^* <$ 95%, yet two grains of ~62 Ma, a grain of ~72 Ma and a grain of ~925 Ma have $^{40}Ar^* >$ 95%. The grains included in the weighted mean age describe a normal distribution (p-value = 0.840; skewness = 0.451; W statistic = 0.967). The inverse isochron yields an intercept that overlaps with the atmospheric ratio. Full analytical data in Appendix XI.

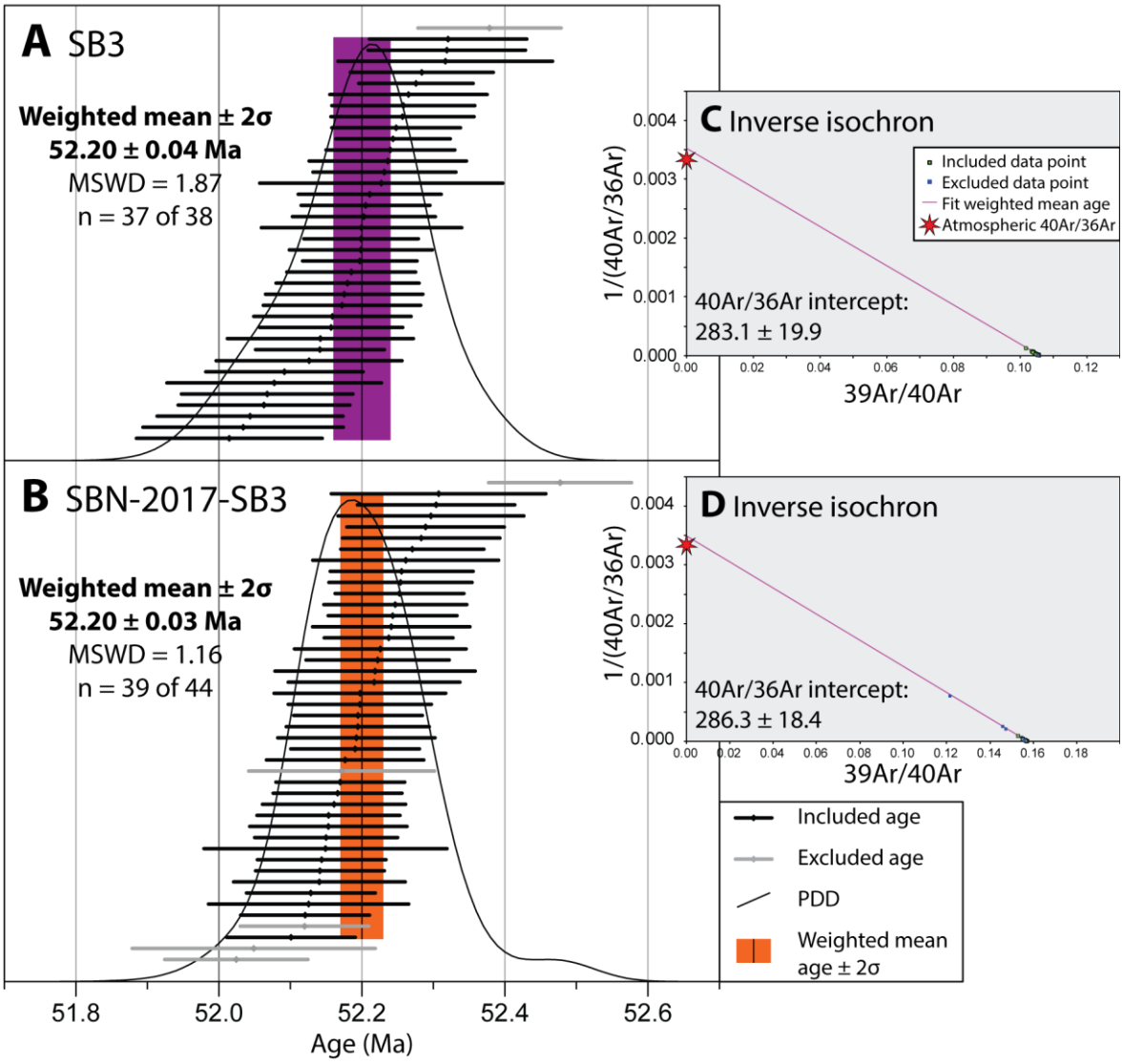

Figure 4.7 *- $^{40}Ar/^{39}Ar$ results of tephra SB-3 for ash samples SB3* ***(A)*** *and SBN-2017-SB3* ***(B)****. Ages of individual grains are represented by bars on the 2σ level; grey bars are excluded from the calculation of the weighted mean age (either outlier or $^{40}Ar^* < 95\%$). PDD's are based on both included and excluded individual ages; y-axis is relative probability. The weighted mean age is represented by a coloured bar on the 2σ level and stated with the MSWD and number of included individual ages.* ***C, D)*** *Inverse isochrons of data in A and B. The atmospheric $^{40}Ar/^{36}Ar$ composition of 298.56 (Lee et al., 2006) is indicated by a red asterisk. The inverse isochron intercept - translated to $^{40}Ar/^{36}Ar$ - is stated in the lower left corner of the graph.*

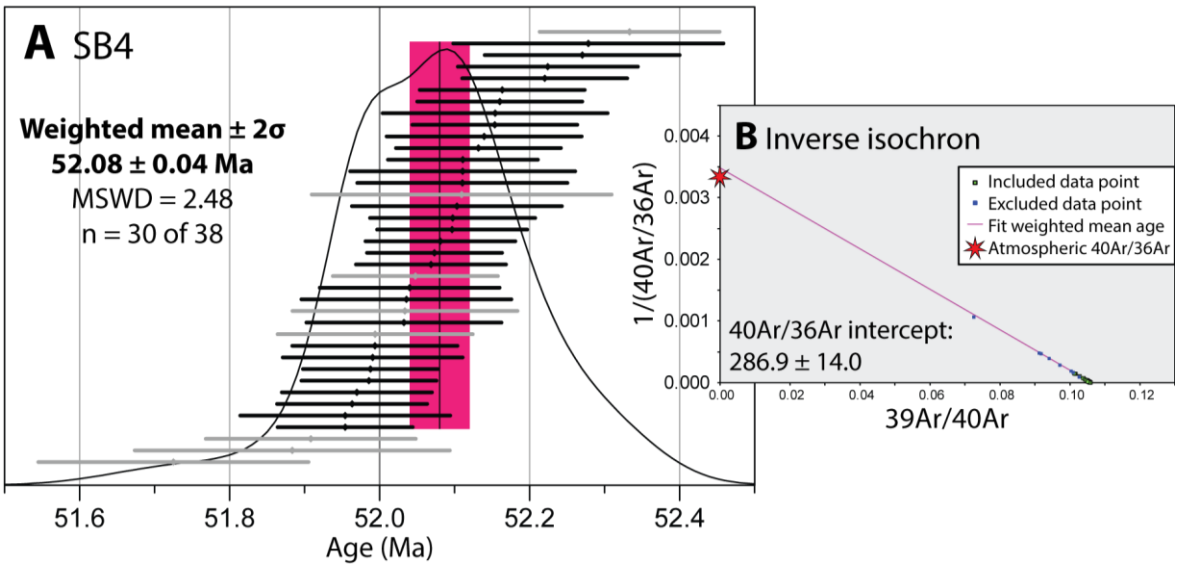

Figure 4.8 *- $^{40}Ar/^{39}Ar$ results of ash sample SB4.* ***A****) Ages of individual grains are represented by bars on the 2σ level; grey bars are excluded from the calculation of the weighted mean age (either outlier or $^{40}Ar^* < 95\%$). PDD is based on both included and excluded individual ages; y-axis is relative probability. The weighted mean age is represented by a coloured bar on the 2σ level and stated with the MSWD and number of included individual ages.* ***B)*** *Inverse isochrons of data in A. The atmospheric $^{40}Ar/^{36}Ar$ composition of 298.56 (Lee et al., 2006) is indicated by a red asterisk. The inverse isochron intercept - translated to $^{40}Ar/^{36}Ar$ - is stated in the lower left corner of the graph.*

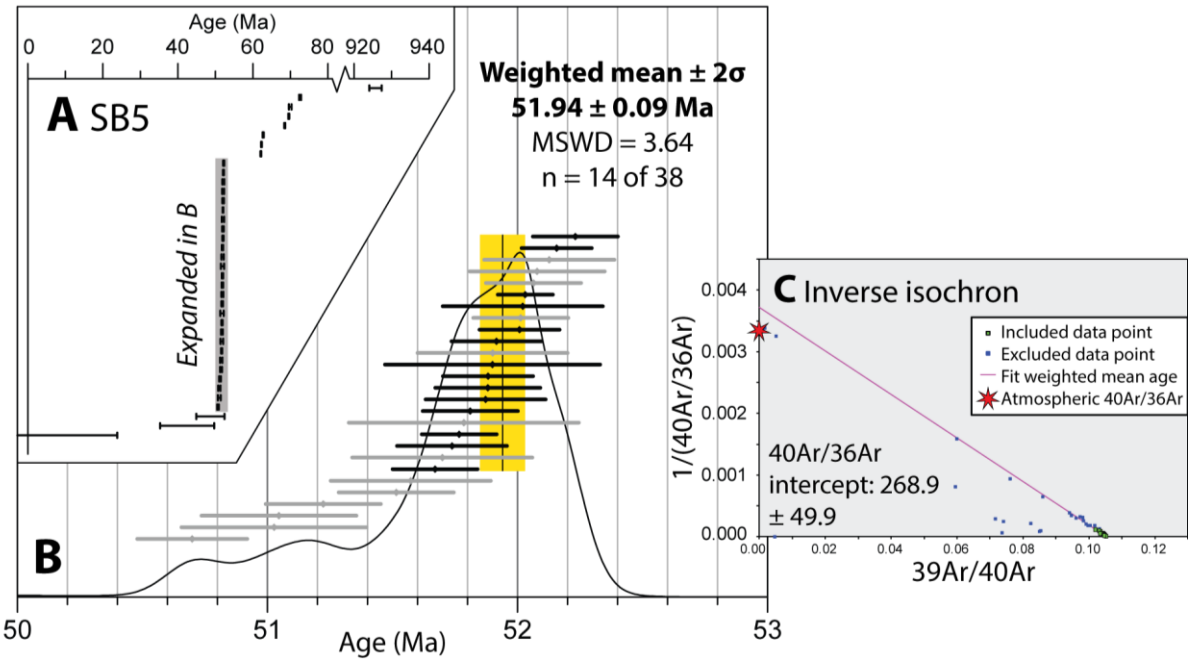

Figure 4.9 *- $^{40}Ar/^{39}Ar$ results of ash sample SB5.* ***A****) Ages of all individual grains represented by bars on the 2σ level.* ***B)*** *Individual ages in the 50-53 Ma range represented by bars on the 2σ level; grey bars are excluded from the calculation of the weighted mean age (either outlier or $^{40}Ar^* < 95\%$). PDD is based on both included and excluded individual ages; y-axis is relative probability. The weighted mean age is represented by a coloured bar on the 2σ level and stated with the MSWD and number of included individual ages. Note that grid lines have the same interval as in previous age figures.* ***C)*** *Inverse isochrons of data in B. The atmospheric $^{40}Ar/^{36}Ar$ composition of 298.56 (Lee et al., 2006) is indicated by a red asterisk. The inverse isochron intercept - translated to $^{40}Ar/^{36}Ar$ - is stated in the lower left corner of the graph.*

4.3 Magnetostratigraphy

4.3.1 Thermomagnetic results

Results from thermomagnetic runs are presented in Fig. 4.10; Appendix XVI contains analytical data. The results can be roughly divided into two groups: samples showing a concave up thermomagnetic curve (A-D in Fig. 4.10) and samples showing a concave down thermomagnetic curve (E-G in Fig. 4.10). Samples subjected to stepwise heating and cooling before reaching maximum temperature, yielded the same overall heating curve as comparable samples that experienced continuous heating.

The first sample group (A-D) has magnetization equivalent to 0.02 - 0.06 Vrms at room temperatures that decreases to -0.010 - -0.005 Vrms at 700 °C. Upon cooling back to room temperature the magnetization reaches a 0.005 - 0.015 Vrms lower value than the initial starting value. The heating and cooling curve overlap between 500 and 700 °C. Especially in the heating curve of sample A a change in slope is visible between 400 and 500 °C that creates this overlap. Samples B-D show first an increase in slope and then flattening between 600 and 700 °C.

The sample group yielding concave down thermomagnetic curves (E-G) show irreversible curves too: magnetization starts at values equivalent to 0.085 - 0.270 Vrms at room temperature, decreases to 0.02 - 0.10 Vrms near 700 °C and ends at 0.015 - 0.025 Vrms lower than the starting value. The heating curves show a decreasing shift between 250 and 300 °C. In the few 10s of °C before reaching maximum temperature, the curves are at their steepest.

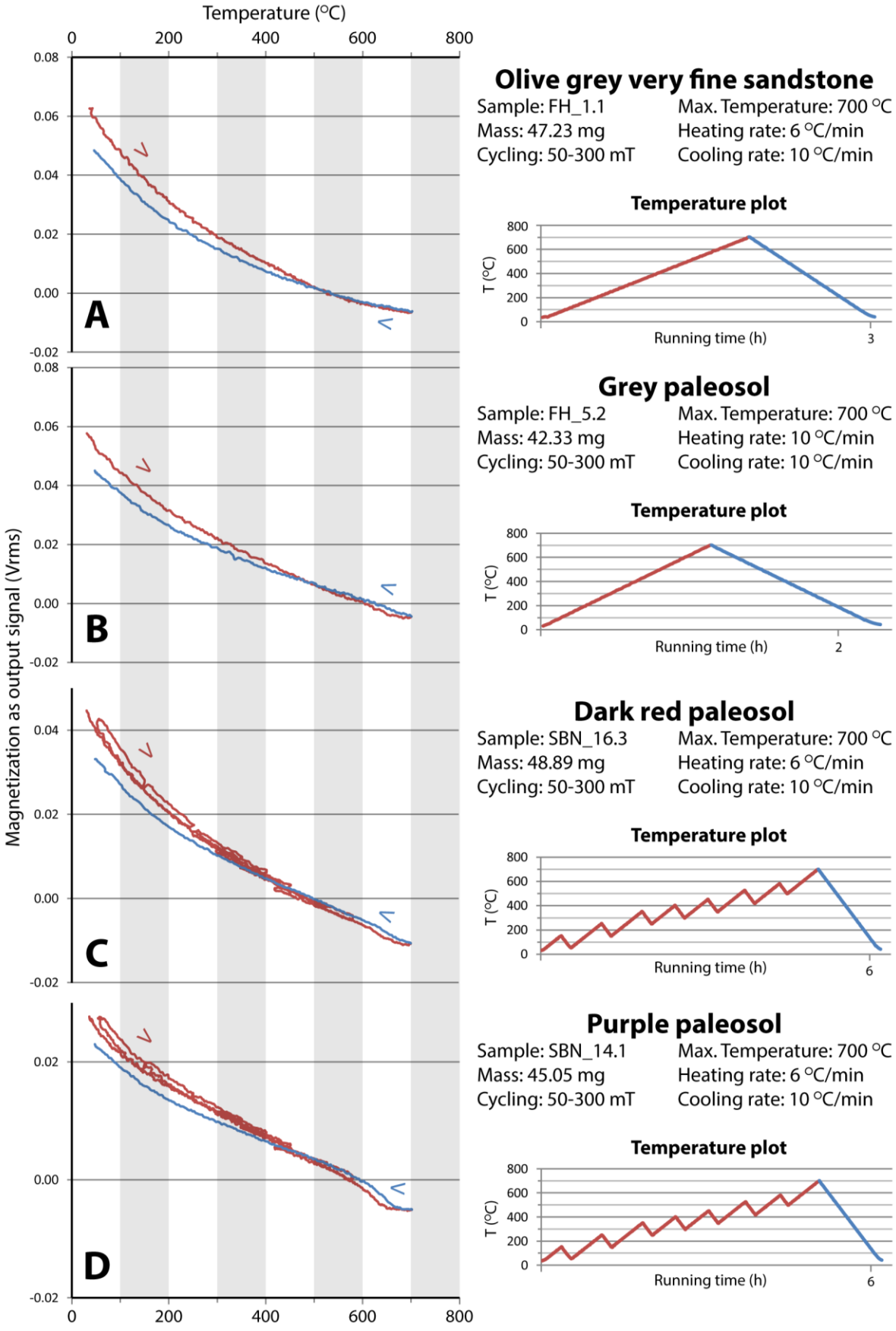

Figure 4.10 - *Continues on next page.*

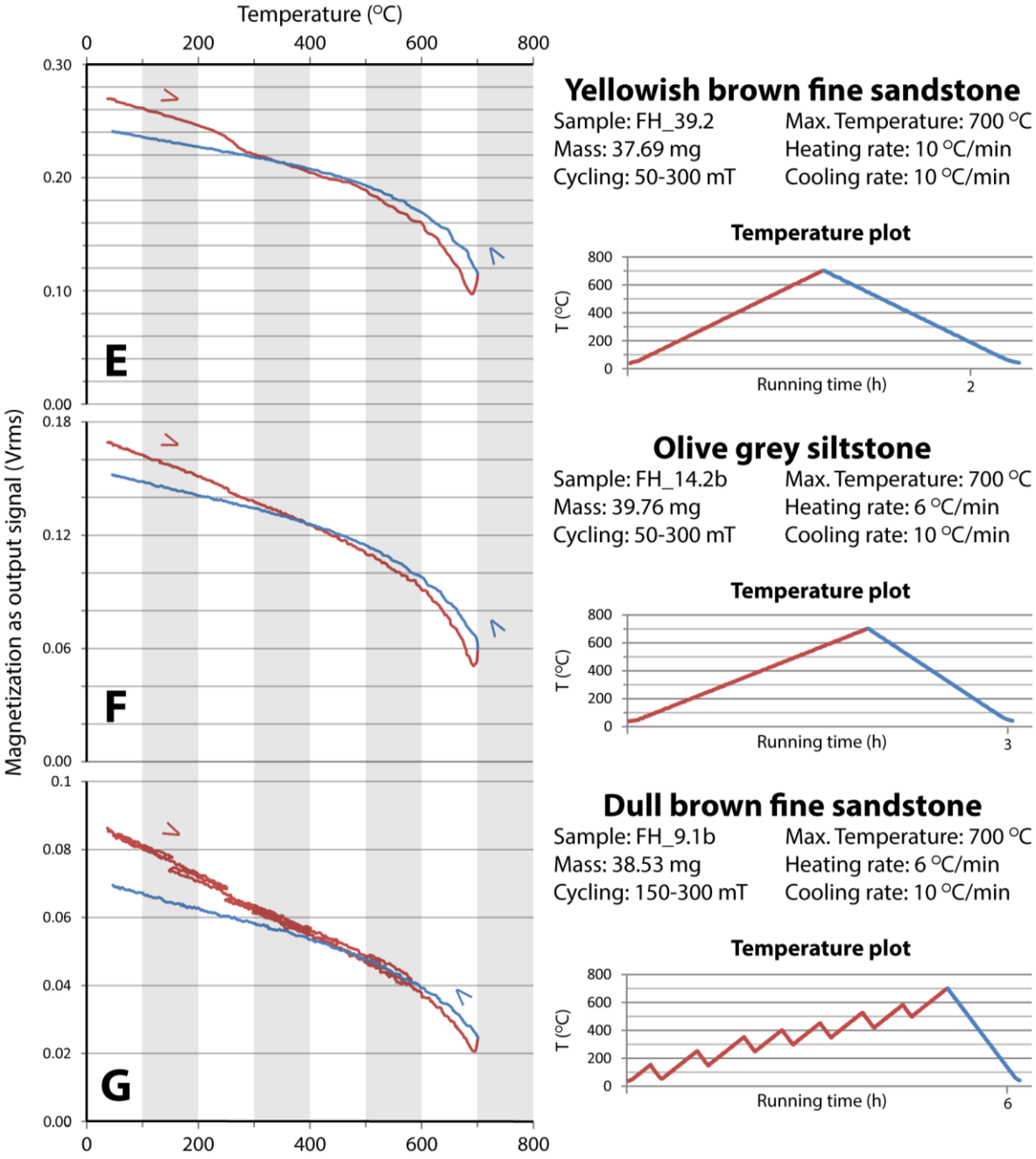

Figure 4.10 *- Results of thermomagnetic analyses on a Curie balance. On the left the Savitzky-Golay filtered thermomagnetic curves: in red the heating curves and in blue the cooling curves. Arrows indicate the (overall) direction of temperature change. Magnetization on y-axis is represented by the non-calibrated output signal of the sensor (note that horizontal grid lines in all graphs indicate steps of 0.02 Vrms). Sample and experiment specifics are given on the right. Temperature plots show the temperature applied during the runs: in red heating and in blue cooling (corresponding to the thermomagnetic heating and cooling curve).*

4.3.2 Characteristic remnant magnetisation

Paleomagnetic specimens have NRM in the range of 4 to 6,000 µA/m (median 444 µA/m). Specimens with NRM exceeding 10^3 µA/m generally came from paleosols. After AF demagnetisation up to 100 mT remaining magnetization was on average ~28% of NRM and for TH demagnetised specimens (up to maximum 650 °C) this was ~20%. Demagnetization behaviour was variable and frequently unstable. From 16.1% of specimens a ChRM could be established via PCA (Fig. 4.12A and B), 39.3% via a Fisher mean (Fig. 4.12D and E); 11.3% were demagnetised at ~200 °C (Fig. 4.12C) and from 33.3% no stable ChRM component could be isolated. Demagnetization behaviour of the latter group was uninterpretable (13.7%; Fig. 4.12F) or could best be described by a great circle path (19.6%; Fig. 4.12G). The majority of specimens showed a north and downward magnetization component in the 4 - 20 mT / 80 - 200 °C range. ChRM components were mostly isolated from demagnetisation steps 20 - 70 mT / 200 - 450 °C and 200 - 520 °C. ChRM directions have a wide spread (Fig 4.11); Fisher mean direction of data points on the lower hemisphere is 337.9/65.3 (n = 74; calculated in Stereonet 10.0 (Allmendinger et al., 2012; Cardozo and Allmendinger, 2013)). Upper hemisphere data points have a Fisher mean of 181.3/-67.5 (n = 19). Appendix XII contains NRM and ChRM data; raw demagnetisation data in Appendices XII, XIV and XV.

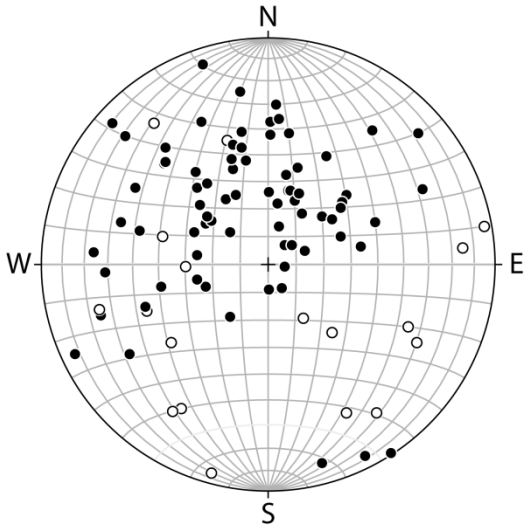

Figure 4.11 *- Equal area projection of all ChRM directions (n = 93). Closed symbols in lower hemisphere, open symbols in upper. Exported from Stereonet 10.0.*

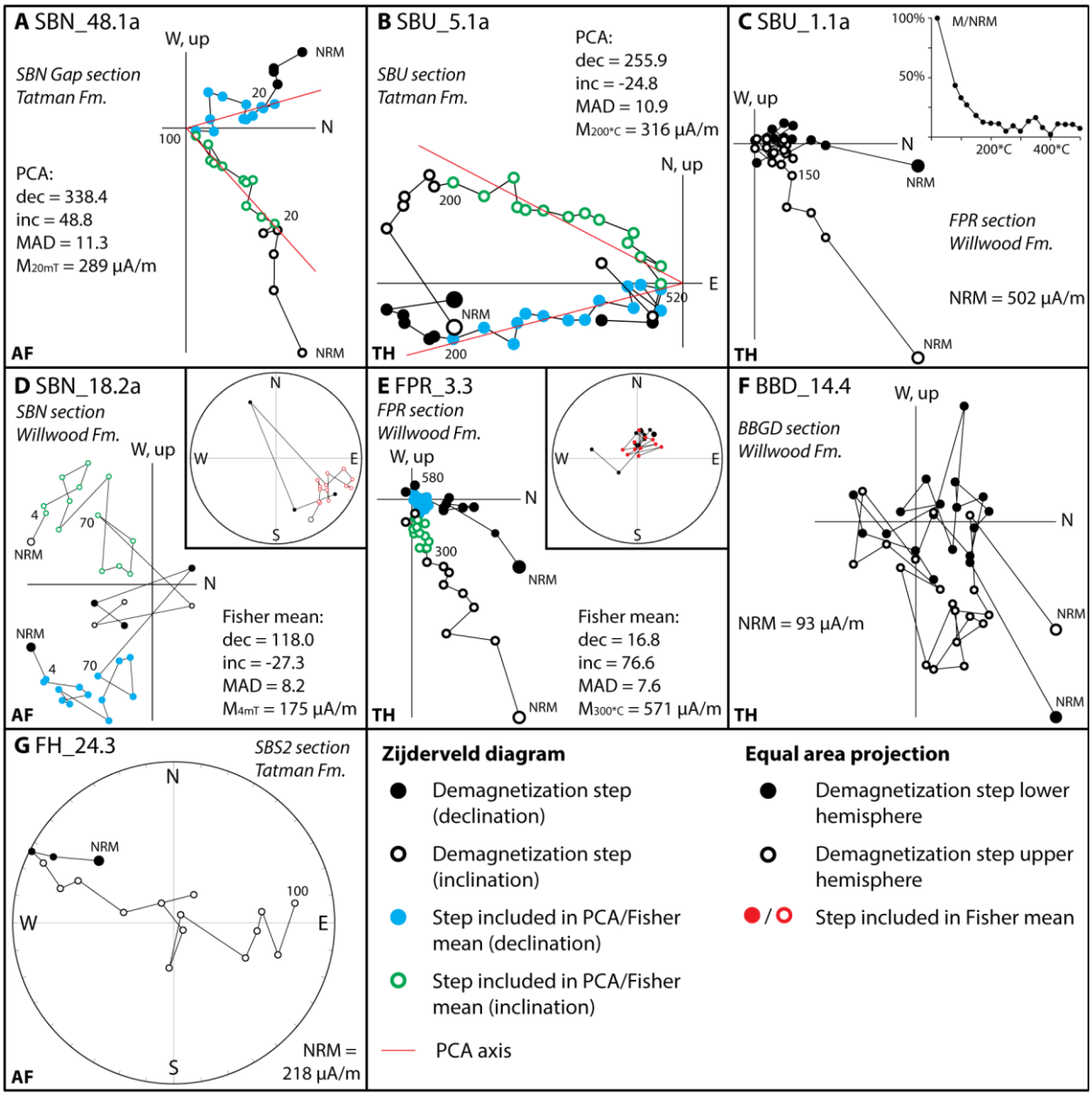

Figure 4.12 *- Examples of AF and TH demagnetization behaviour of samples from the Willwood and Tatman Fm. in Zijderveld diagrams and equal area projections. Type of demagnetisation in lower left corner. Zijderveld diagrams show data in geographic coordinates and on a north-south vertical plane, except for* ***B*** *(east-west vertical plane). Important demagnetization steps are quantified in either mT (AF) or °C (TH). For ChRMs - calculated through PCA (****A*** *and* ***B****) or a Fisher mean (****D*** *and* ***E****) - declination, inclination, MAD and magnetisation (M) at first included data point are specified.* ***C)*** *Sample demagnetised at ~200 °C. Resultant magnetisation relative to NRM vs. demagnetisation step is displayed in upper right corner.* ***F)*** *Uninterpretable demagnetisation behaviour.* ***G)*** *Demagnetisation best described by a great circle. All plots exported from Paleomagnetism.org (Koymans et al., 2016).*

4.4 Cyclostratigraphy

4.4.1 Colour reflectance, SDI and GSI records

Fig. 4.13A and B display the measured colour reflectance records (L*, a* and b*) and the calculated SDI and GSI records next to the lithostratigraphic logs of the Blackburn Gulch composite and the SBS2 section. Analytical data in Appendix XVII. For the Blackburn Gulch composite, sediment lightness L* varies between 20 and 80, yellowness b* between 0 and 30 and the redness a* between -4 and 16. The ranges of L* and b* of the SBS2 section are equal, but a* ranges from -2 to 11. The soil development of the Blackburn Gulch composite varies between no pedogenesis (SDI = 0) and intense pedogenesis (SDI 1 - 2). The GSI of the SBS2 section fluctuates between -0.1 (carbonaceous shale) and 1.9 (medium sandstone).

In general, lithology and colour reflectance are related: sandstones yield high L* and b* values, while mudrock and carbonaceous shales yield low L* and b* values. Paleosols are characterised by high a* values and low L* values, although grey paleosols yield low a* values. Purple paleosols generally have lower b* values than red paleosols. These relations are reflected by the distribution of colour values over the SDI and GSI (Fig. 4.13C and D): SDI and a* show a positive correlation, SDI and L* a negative correlation, but SDI and b* show no clear correlation. GSI and both L* and b* show a positive correlation, while GSI and a* show no correlation.

Metre-scale paleosols in the Blackburn Gulch composite alternate with metre-scale intervals of sandstones with no soil development and sandstone and mudrock with weak pedogenesis and minor carbonaceous shales. Below 35 m stratigraphic position these metre-scale paleosols are thickest; in the Interval of 35-75 m the frequency and intensity of paleosols is low; and above 75 m the frequency of paleosols is high. At SBS2 metre-scale fining upward sequences can be distinguished from sandstone to mudrock with no or weak pedogenesis and carbonaceous shale.

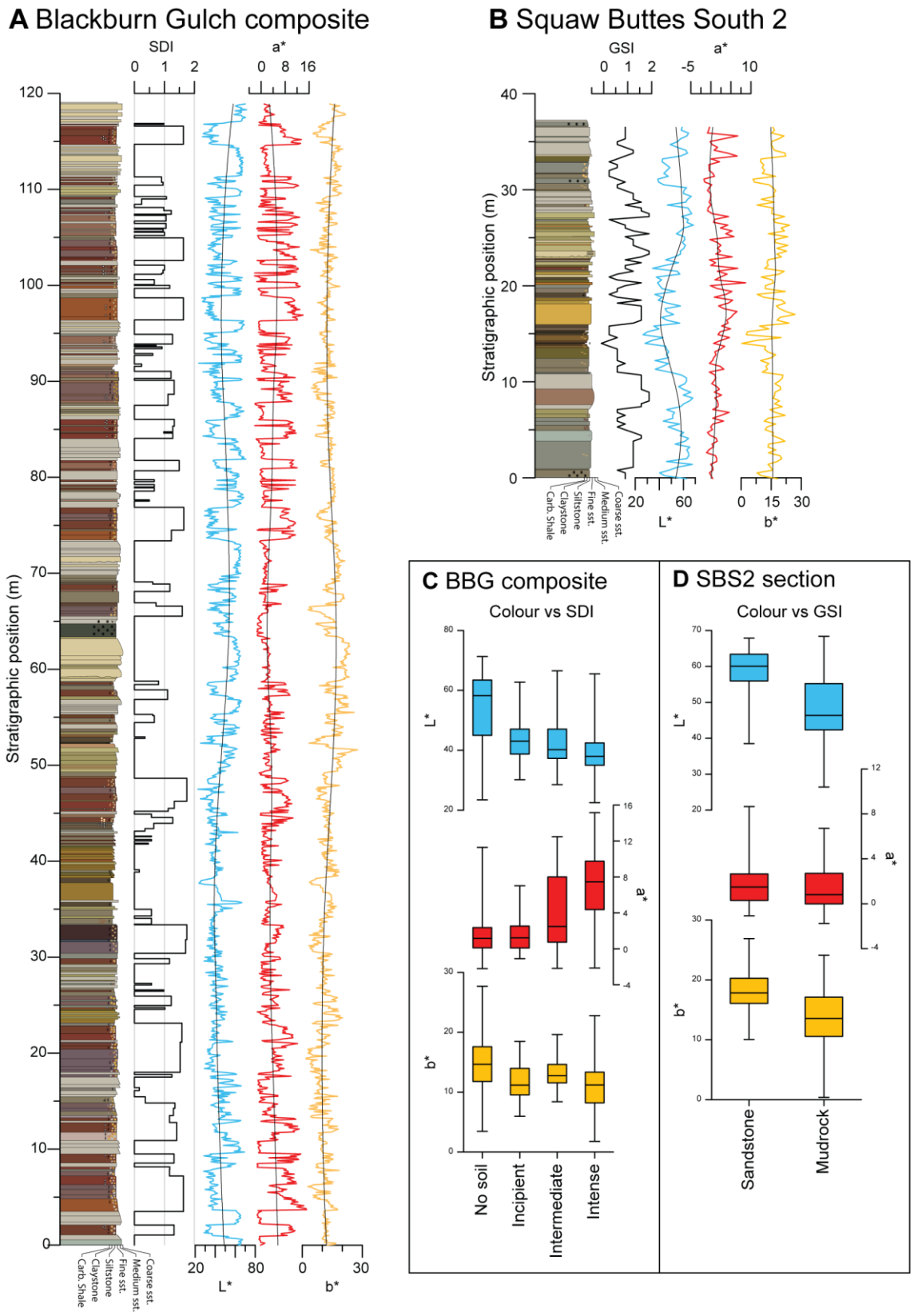

Figure 4.13 *- Blackburn Gulch composite* ***(A)*** *and Squaw Buttes South 2 section* ***(B)*** *lithostratigraphic logs accompanied by soil development index (SDI) and grain size index (GSI), respectively; and lightness (L*); redness (a*); and yellowness (b*). Low frequency*

trends in the colour reflectance records - removed by subsequent detrending - are represented by a black line within the L, a* and b* records. Willwood Ash at 64 m in A; SB-4 (0 m), SB-5 (31 m) and SB-6 (37 m) in B.* ***C)*** *Boxplots displaying the distribution of colour reflectance values over soil development: no soil (SDI = 0), incipient (SDI 0 - 0.5), intermediate (SDI 0.5 - 1) and intense (SDI >1).* ***D)*** *Boxplots displaying the distribution of colour reflectance values over mudrock (GSI < 1) and sandstone (GSI > 1).*

4.4.2 Spectral analysis

Results of 2π multitaper method spectral analysis of SDI, GSI and detrended colour reflectance records are presented in power spectra of Fig. 4.14. Dominant frequencies are listed and grouped in Table 4.3 and 4.4.

Blackburn Gulch composite							
SDI		**Lightness L***		**Redness a***		**Yellowness b***	
f (cycles/m)	Period (m)	f (cycles/m)	Period (m)	f (cycles/m)	Period (m)	f (cycles/m)	Period (m)
0.0807	12.39			0.0739	13.53	0.0723	13.83
0.1076	9.29	0.1092	9.16			0.0924	10.82
0.1546	6.47	0.1664	6.01	0.1361	7.35		
		0.1849	5.41			0.1832	5.46
0.2252	4.44	0.2269	4.41	0.2336	4.28		
0.3109	3.22	0.3126	3.20	0.3176	3.15		
0.3782	2.64	0.4017	2.49			0.3513	2.85
0.5496	1.82			0.5294	1.89		
0.6504	1.54			0.6706	1.49		

Table 4.3 *- Dominant spectral peaks in the records of the BBG composite in frequency (f) and period (1/frequency). Underlined periodicities are included in subsequent filtering.*

Squaw Buttes South 2							
GSI		**Lightness L***		**Redness a***		**Yellowness b***	
f (cycles/m)	Period (m)	f (cycles/m)	Period (m)	f (cycles/m)	Period (m)	f (cycles/m)	Period (m)
		0.0867	11.53	0.0867	11.53	0.0921	10.86
		0.1192	8.39	0.1138	8.79		
0.1518	6.59	0.1518	6.59	0.1463	6.84	0.1409	7.10
		0.1897	5.27				
0.542	1.85						
				0.8401	1.19		
0.981	1.02			0.9756	1.03		

Table 4.4 *- Dominant spectral peaks in the records of the SBS2 section in frequency (f) and period (1/frequency). Underlined periodicities are included in subsequent filtering.*

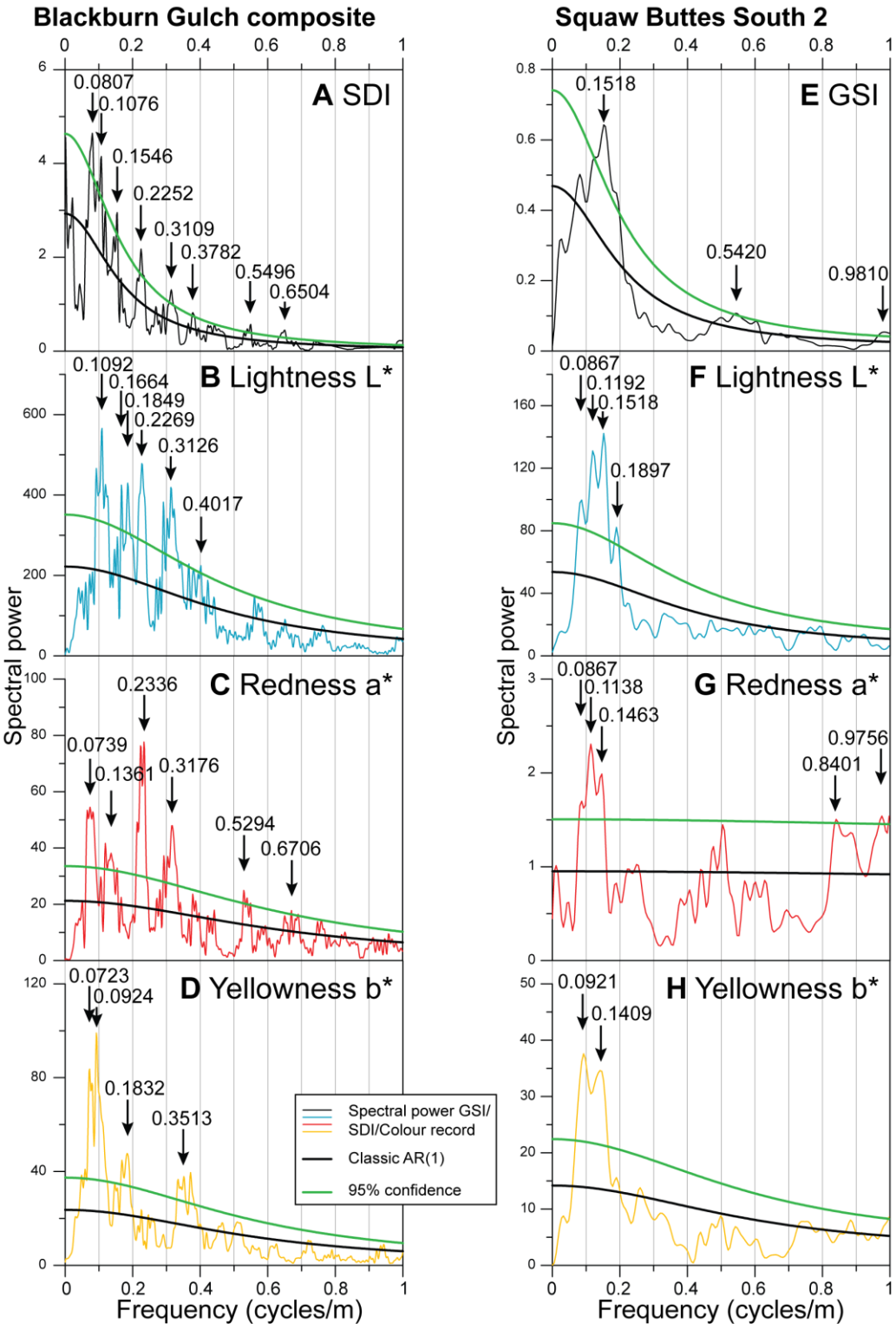

Figure 4.14 *- 2π multitaper method power spectra of* ***A)*** *SDI,* ***B)*** *lightness L*,* ***C)*** *redness a* and* ***D)*** *yellowness b* records of the Blackburn Gulch and* ***E)*** *GSI,* ***F)*** *L*,* ***G)*** *a* and* ***H)*** *b* of the Squaw Buttes South 2 section. Dominant spectral peaks, above 95% level of the AR(1) red noise model, are indicated by arrows.*

4.4.3 Filters

Dominant periodicities in the SDI, lightness L* and redness a* records from the Blackburn Gulch composite, extracted using bandpass filtering, are shown in Fig. 4.15. The filters are grouped in filters of ~9 m period, ~7.4 m, ~6 m and ~4.4 m. SDI and a* filters of the same period are in phase, but are 180° out of phase with L*. None of the filters has consistent amplitude throughout the composite, but the ~4.4 metre filters have low amplitude in the entire lower half of the composite. Filters are linked to the lithostratigraphic log by connecting the top of filter cycles to the top of paleosol(s) (intervals) (Fig. 4.15). The ~9 m filters are related to alternations of paleosol intervals and intervals of higher grain size and less pedogenesis, but have trouble characterizing the higher frequency of paleosols above 80 m stratigraphic position. Besides, the cycle between 33 and 40 m stratigraphic position does not match well with the stratigraphy. The ~7.4 m filter is similar to the ~9 m filters, but better reflects the higher frequency of paleosols in the upper part of the stratigraphy. The ~6 m filters also match well in this upper part, but divide some major paleosol intervals in the lower part into individual purple and red soil horizons and recognise thick sandstones as single cycles. The ~4.4 m filters are similar, but reflect even more paleosol intervals in the top part of the stratigraphy.

GSI, L*, a* and b* filters of the Squaw Buttes South 2 section are grouped in ~9 m and ~6 m filters (Fig. 4.16). The amplitude of all filters is fairly consistent throughout the section. The GSI, L* and b* filters of similar period are in phase, but the a* filter is not exactly in or out of phase. Filters are linked to the lithostratigraphic log by connecting filter cyclicity to fining upward sequences. Below 16 m stratigraphic position, all filters are related to two fining upward sequences. Above 16 m, the ~9 m filters reflect two sequences, but the ~6 m filters match to three sequences.

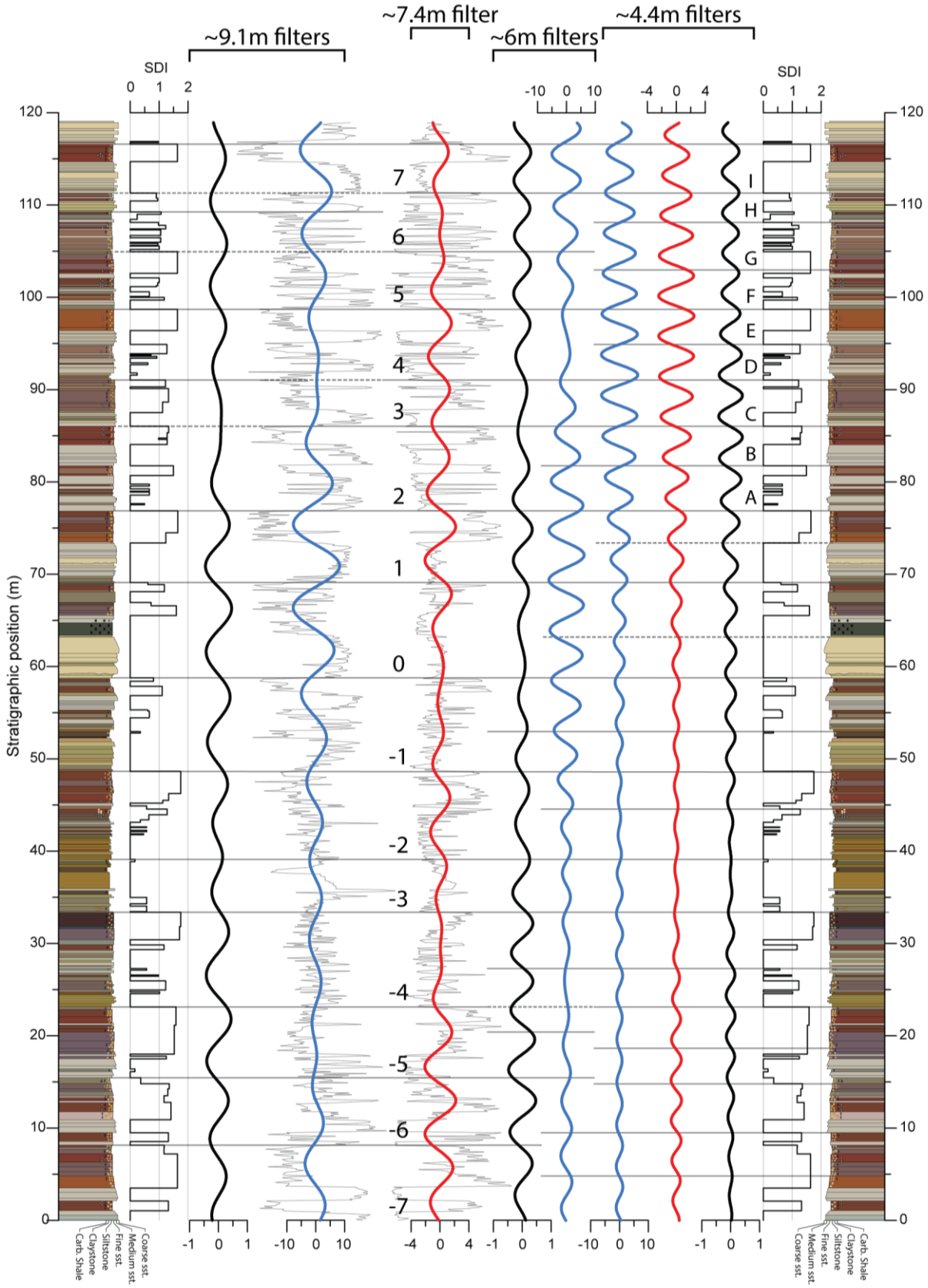

Figure 4.15 *- Blackburn Gulch composite lithostratigraphic log and soil development index (SDI) accompanied by Gaussian bandpass filters of SDI (black), lightness L*(blue) and redness a* (red). The detrended L* record is presented in grey behind the ~9.1 m L* filter (same*

scale); the detrended a record in grey behind the ~7.4 m a* filter (same scale). Horizontal lines relate filter cyclicity to the lithostratigraphic log (dotted if not relevant or problematic). Labelling of cycles is discussed in section 5.3.1.*

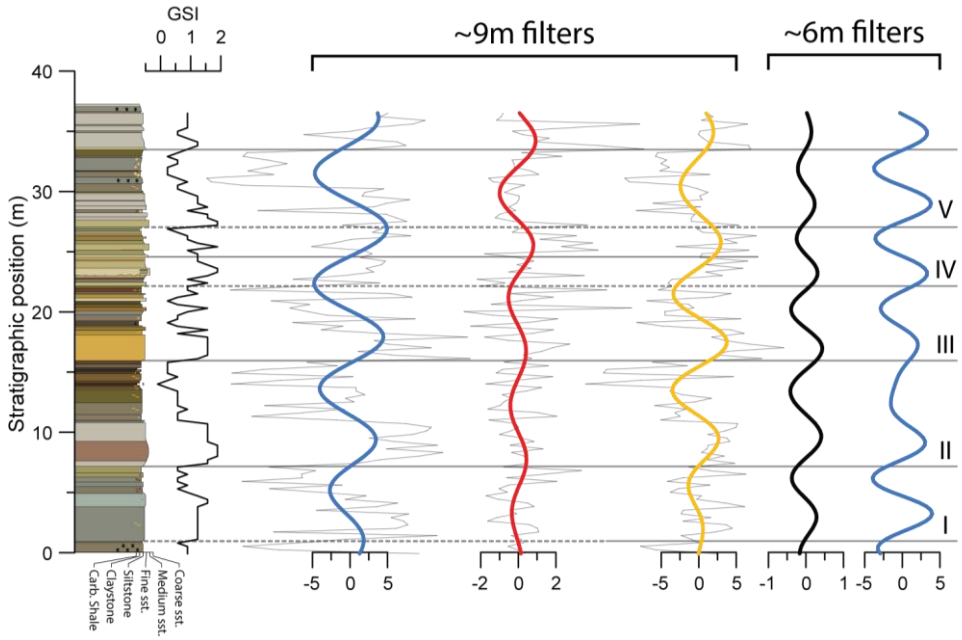

Figure 4.16 *- Squaw Buttes South 2 lithostratigraphic log and grain size index (GSI) accompanied by Gaussian bandpass filters of GSI (black), lightness L*(blue), redness a* (red) and yellowness b* (yellow). The detrended L* record is presented in grey behind the ~9 m L* filter; the detrended a* record in grey behind the a* filter; and the detrended b* record in grey behind the b* filter (record and filter on the same scale). Horizontal lines relate filter cyclicity to the sedimentary log (dotted if not relevant). Labelling of cycles is discussed in section 5.3.1.*

5. Discussion

5.1 Tephra ages

5.1.1 Willwood Ash

To date, the Willwood Ash provides the only radio-isotopic tie-point for the upper part of the Willwood Fm. Wing et al. (1991) presented the first radioisotopic age for a 1 m thick bentonite on the north side of Squaw Teats Divide (also Squaw Buttes Divide); their $^{40}Ar/^{39}Ar$ date of 52.8 ± 0.3 Ma (2σ error) was based on incremental heating of multigrain (100mg) sanidine using the Minnesota hornblende standard. Smith et al. (2003) recalculated this age to 53.09 ± 0.34 Ma using the standard ages of Renne et al. (1998). Smith et al. (2004) sampled Bed B of Rohrer (1964a, b) that circumvents Tatman Mountain: total fusion and incremental heating experiments of one to three sandine crystal aliquots yielded a $^{40}Ar/^{39}Ar$ age of 52.59 ± 0.19 Ma, included in the GTS 2012 (Vandenberghe et al., 2012; recalculated to 52.93 ± 0.23 Ma using FCT age of Kuiper et al. (2008)). Smith et al. (2014) recalculated the age of Smith et al. (2004) to 52.91 ± 0.23 Ma (internal error) relative to FCT age of Kuiper et al. (2008) and using ^{40}K decay constants of Min et al. (2000); equal to age calculations in this study.

This study contributes single grain total fusion $^{40}Ar/^{39}Ar$ dates an order of magnitude more precise for samples from three locations of the Willwood Ash: 1) north of Squaw Buttes Divide at the locality of Wing et al. (1991); 2) northwest of Squaw Buttes Divide, part of the Squaw Buttes sections, where the bentonite was named SB-1; and 3) south of Tatman Mountain in the Blackburn Gulch sections, corresponding to Bed B of Rohrer (1964a, b). The weighted mean $^{40}Ar/^{39}Ar$ dates are 52.43 ± 0.03/0.86 Ma, 52.52 ± 0.04/0.86 Ma and 52.54 ± 0.03/0.86 Ma, respectively, and are presented in Fig. 5.1. Although the latter two are statistically identical, the first date is significantly younger (90-110 kyr). The dates of this study can only be directly compared to the age of Smith et al. (2014), as $^{40}Ar/^{39}Ar$ ages need to be calibrated to the same standard age and decay constants for intercomparison (Schaen et al., 2020): the new dates are 370-480 kyr younger.

The discrepancy between the dates of the three samples of this study can arise from I) the existence of different tephra layers at the different sampling sites, II) geological variations within the sanidine populations of different samples or III) analytical inconsistencies. I) The

first option would imply that two different bentonites of similar thickness and appearance are present in the upper part of the Willwood Fm.; according to our dates the tephra at the Wing et al. (1991) locality would be positioned ~17 m stratigraphically above the tephra included in the Blackburn Gulch and Squaw Buttes sections, given a sedimentation rate of 170 m/Myr (Fig. 5.1C). However, another Willwood Fm. tephra has not been encountered in the sections or mentioned in literature. Tauxe et al. (1994) placed the tephra at the Wing et al. (1991) locality ~65 m below the Willwood-Tatman Fm. boundary in their stratigraphy, whereas at Blackburn Gulch and Squaw Buttes it is positioned ~54 m below the boundary; but this can be due to a difference in sedimentation rate, in placement of the boundary or due to the diachronous nature of the Tatman Fm. base. The younger tephra could have been eroded by subsequent fluvial processes at Blackburn Gulch and Squaw Buttes, while the older one would have been eroded at the Wing et al. (1991) locality. Yet Rohrer (1964a, b) found the bentonite present over several 10s of kilometres around Tatman Mountain, indicating good lateral preservation. In fact, it was possible to trace the striking appearance of the tephra between the Squaw Buttes and the Wing et al. (1991) localities over ~12 km via Google Earth Pro, connecting the sampling sites that yielded different dates (Fig. 4.1). Furthermore, the tephra is probably traceable along the entire eastern side of Squaw Buttes Divide. It is therefore most probable that the same single bentonite was sampled in this and previous studies: the Willwood Ash.

II) Dates of individual crystals older than the mode of a total fusion dataset are routinely explained by trapped excess ^{40}Ar or by the presence of antecrysts or xenocrysts, while younger dates reflect ^{40}Ar loss; calculation of a weighted mean age is then a balance between older and younger crystals leading to age dispersion between total fusion datasets (Schaen et al., 2020; Andersen et al., 2017). Differences between weighted mean dates of the Blackburn Gulch and Squaw Buttes datasets and the dataset from the Wing et al. (1991) locality must accordingly be explained by either preferential deposition of young sanidine crystals at the latter site and/or by fortuitously dominant selection of young crystals from the Wing et al. (1991) locality sample for analyses. Inverse isochron intercepts of the three weighted mean dates are indistinguishable from atmospheric ratio on the 2σ level, thus the influence of excess ^{40}Ar is not indicated. However, incremental heating experiments provide better assessment of eruption age and age dispersion (Andersen et al., 2017). Four

incremental heating experiments of Smith et al. (2004) indeed demonstrate crystal phases of contrasting apparent ages, and, consequently, their plateau weighted mean age is 80 kyr younger than their total fusion weighted mean age. From this perspective, the younger population of total fusion dates best represents the eruption age.

III) Samples from the Wing et al. (1991) locality and Blackburn Gulch were irradiated in the same cup and analysed in the same tray runs using the same standards, so analytical inconsistencies causing the discrepancy in date are unlikely. However, the assignment of the same J value to both samples might have been problematic: adopting - by way of illustration - a more conservative approach for the youngest sample through inclusion of standards from only the two closest positions in the same cup layer (F12 and F13; Appendix II), J-value increases by 0.14% and yields a weighted mean date of 52.50 ± 0.03 Ma which is statistically identical to the dates of the other two samples.

Lastly, the inconsistency between the dates presented here and the age of Smith et al. (2014) is not explained by favouring their plateau age over their combined weighted mean age as this is only 50 kyr younger (Smith et al., 2004). Smith et al. (2004) found their age based on experiments with one to three crystal aliquots to be 500 kyr younger than the multi-crystal result of Wing et al. (1991) and proposed that detrital or xenocryst contaminants distort analyses of larger sample sizes. Similarly, it can be stated that the exclusively single crystal dates here more effectively bypass this effect than the age of Smith et al. (2004, 2014), but it remains unclear whether this explains the entire 370-480 kyr difference. The new dates are preferred though, as they are based on a more extensive and precise analysis (125 vs. 20 experiments; errors an order of magnitude smaller). The J-value discrepancy (III) is the preferred explanation for the date discrepancy in this study since this offers the simplest solution to the contradictory age of one sample. In conclusion, the recommended eruption age of the Willwood Ash is 52.53 ± 0.04/0.86, the average of the Blackburn Gulch and Squaw Buttes samples, acknowledging that total fusion results possibly overestimate the eruption age.

5.1.2 Tatman tephras

This study presents the first radio-isotopic geochronology for the Tatman Fm. by providing single grain total fusion $^{40}Ar/^{39}Ar$ dates of three tephras labelled SB-3, SB-4 and SB-5 (Fig.

5.1; two samples from SB-3 yielded identical dates). The weighted mean dates (52.20 ± 0.04/0.85 Ma, 52.08 ± 0.04/0.85 and 51.94 ± 0.09/0.85, respectively) show no evidence of excess argon, are coherent with stratigraphic position and therefore are proposed to represent eruption ages. Unfortunately, poor bed-to-bed correlation between Squaw Buttes and Blackburn Gulch hampers the exact identification of these bentonites away from the Squaw Buttes site and thus their role as basin-wide stratigraphic markers is not yet resolved. The internal errors on the SB-3 and SB-4 ages are similar to that of the Willwood Ash samples, but the error on SB-5 is twice as large because its smaller sized crystals resulted in lower measurement intensities. Furthermore, the SB-5 range of individual dates is extensive and even encompasses crystals that are 10s of Myrs older than the weighted mean age. These inconsistent dates reveal the existence of xenocrysts/antecrysts or indicate a more complex depositional history of the bed involving influx of reworked crystals. Despite relatively inferior quality, the established weighted mean age of SB-5 is believed to reflect the age of eruption and, consequentially, the age of bed deposition.

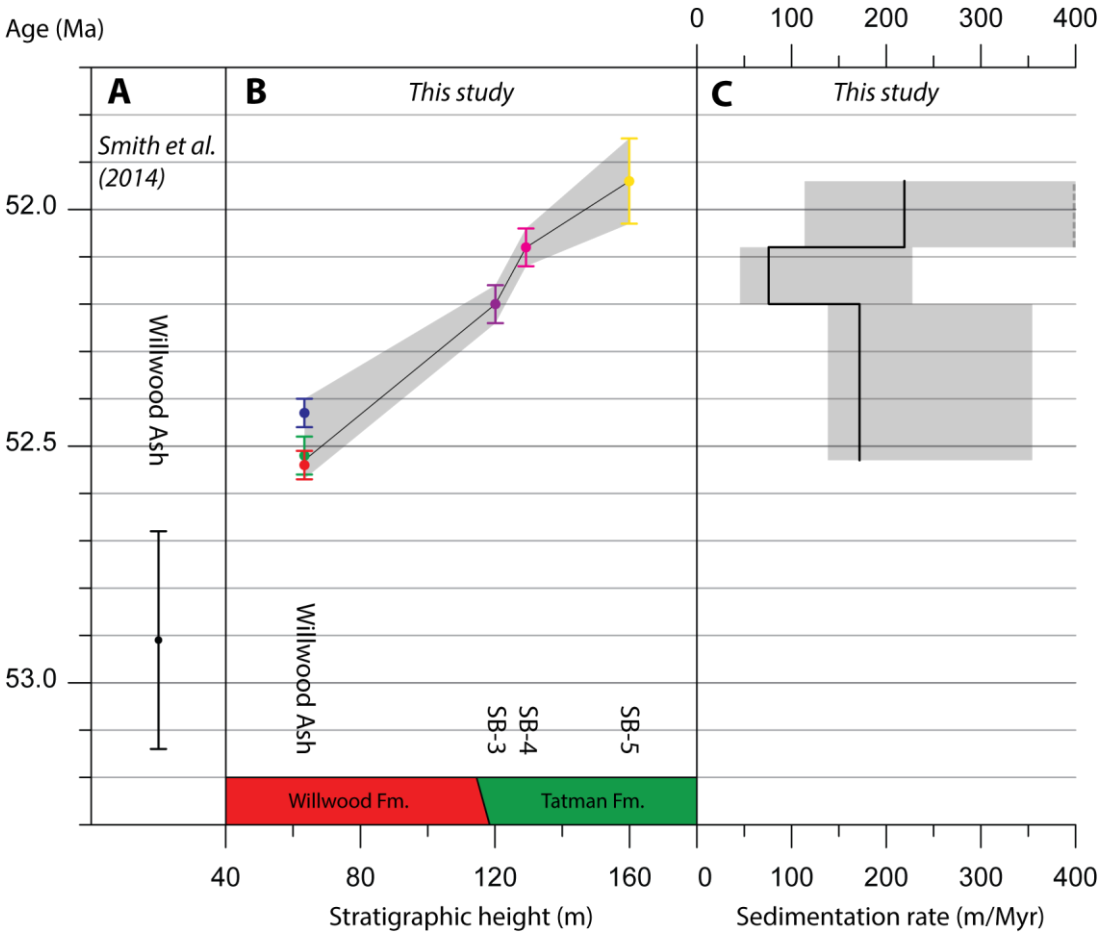

Figure 5.1 *- $^{40}Ar/^{39}Ar$ ages including 2σ internal error and sedimentation rates.* ***A)*** *$^{40}Ar/^{39}Ar$ age of Smith et al. (2014; recalculated from Smith et al., 2004).* ***B)*** *$^{40}Ar/^{39}Ar$ dates of this study set against stratigraphy. Date colour corresponds to Fig. 4.6 to 4.9. Line and grey outline indicate sedimentation rate.* ***C)*** *Sedimentation rates derived from the $^{40}Ar/^{39}Ar$ ages of this study; grey outline indicates range. Maximum rate between SB-4 and SB-5 falls outside graph: 3070 m/Myr.*

5.2 Magnetostratigraphy

5.2.1 Magnetic mineralogy

The mineral carriers and formation of NRM need to be evaluated to establish if ChRM reflects primary remanence at time of deposition and, therefore, if ChRM directions can be used to construct a magnetostratigraphy. Thermomagnetic analysis revealed two groups of behaviour: 1) concave down thermomagnetic curves (non-paleosols) and 2) concave up curves (mostly paleosols). The concave down curves are typical for ferri-/ferromagnetic minerals (McElhinny and McFadden, 2000) and their steep decrease near maximum temperature indicates a Curie temperature between 650 and 700 °C, which is diagnostic for hematite or maghemite (McElhinny and McFadden, 2000). The heating curve of the concave down group shows an irreversible decrease at ~250 °C that corresponds to the conversion of magnetite to maghemite (van Oorschot and Dekkers, 1999; Stacey and Banerjee, 1974). However, the expected irreversible transition of maghemite to hematite at higher temperature is not apparent, but could be inhibited if hematite impurities exist in the initial magnetite (Stacey and Banerjee, 1974). The concave up curve of the second group is typical for paramagnetic minerals (McElhinny and McFadden, 2000); the slight irreversibility of the curve is probably due to dehydration of clay minerals (Mullender et al., 1993). Two samples, purple paleosol and red paleosol, show a steepening of the thermomagnetic curve between 650 and 700 °C that indicates presence of hematite or maghemite (McElhinny and McFadden, 2000), but the latter is improbable due to the absence of distinct irreversible transitions.

Thermomagnetic analysis, therefore, leads to the interpretation that magnetite and (minor) hematite are the carriers of NRM in the non-paleosol Tatman Fm. samples, while hematite is the magnetic mineral in red or purple Willwood Fm. paleosols. Although the analysis was

limited to only seven samples from two sections, the interpreted magnetic mineralogical content is largely in agreement with findings of previous studies in the Willwood Fm.: Neasham and Vondra (1972) found magnetite as detrital material in sandstones through petrography. Butler et al. (1981) inferred the presence of magnetite or titanomagnetite in non-rubified fine lithologies based on petrography and IRM acquisition and demagnetization. Also based on IRM acquisition and demagnetization, Clyde et al. (1994, 2007) identified magnetite and minor hematite in soil A horizons and hematite and trace amounts of magnetite in AB/B horizons. XRD analysis of Kraus and Hasiotis (2006) attributed red colours in paleosols to hematite and also determined the presence of goethite in various soil matrix colours and pedogenic features.

5.2.2 NRM origin

AF and TH demagnetisation of Willwood and Tatman Fm. specimens usually revealed a low stability remanence component (<20 mT or <200 °C) and, if stable, revealed a medium/high stability component. TH treatment proved more successful in demagnetising specimens than AF. The expected normal polarity direction for the Bighorn Basin in the early Eocene, calculated from the reference pole for North America, is declination 349° and inclination 63° (Diehl et al., 1983; Clyde et al., 2007) and is practically indistinguishable from present-day geomagnetic field. Since the low stability component almost consistently showed this normal polarity, it is interpreted as a secondary viscous overprint, following Butler et al. (1981). About 75% of the specimens showed coherent demagnetisation characterised by a ChRM or great circle path generally in the 20-70 mT or 200-520 °C range. This coercivity and unblocking temperature suggests that ChRM is carried by magnetite (Butler, 1992). One specimen was unblocked by 650 °C which suggests a hematite carrier (Butler, 1992). ChRM directions are spread out and no reliable antipodal mean directions could be established. Yet, these ChRMs are believed to reflect normal and reversed primary NRM of Eocene age, obscured by incompletely removed normal overprints. This resistant overprint is especially apparent for specimens with a great circle path from a normal to a more reversed direction.

Primary NRM in the Blackburn Gulch and Squaw Buttes sections is interpreted to be predominantly a depositional remanence carried by detrital magnetite; equal to the conclusion of Butler et al. (1981) for non-pedogenically altered mudrock in the lower part of the Willwood Fm. Primary NRM in paleosols can also reside in fine grained hematite formed

during pedogenesis (Clyde et al., 1994, 2007). The resistant overprint, also reported by Tauxe et al. (1994) and Clyde et al. (1994, 2007), is probably the present-day magnetic field carried by secondary hematite (Clyde et al., 1994; Maxbauer et al., 2016). Maxbauer et al. (2016) compared magnetic properties of equivalent Willwood Fm. paleosols in core (Bighorn Basin Coring Project; Clyde et al., 2013) and outcrop and found increased properties in the latter attributed to the formation of pigmentary hematite during surficial weathering. Even though Maxbauer et al. (2016) only compared paleosol levels, similar weathering could occur in other lithologies as the strong overprint is considered present in many specimens of this study. Additionally, Maxbauer et al. (2016) inferred either a lack of pedogenic magnetite or alteration of pedogenic magnetite during diagenesis. The second scenario could implicate that also magnetite contributes to secondary overprints and that detrital magnetite was affected by diagenesis, challenging the proposed depositional remanence. However, it is assumed here that the first scenario is the case as previous studies have successfully built magnetostratigraphic records at least partly based on remanence residing in magnetite.

5.2.3 Magnetostratigraphy

In short, the ChRM directions are problematic due to a resistant normal overprint. Tauxe et al. (1994), who reported TH demagnetization results similar to this study, also presented widespread ChRM directions for stratigraphy parallel to the sections of this study (their Fig. 4; above ~550-600 m stratigraphic height). They, as well as Butler et al. (1981), Secord et al. (2006) and Clyde et al. (2007), used group statistics to obtain more reliable site mean directions, aided by great circles. However, Tauxe et al. (1994) were unable to calculate site means above the Willwood-Tatman Fm. boundary. Site mean directions were not used in this study because of the insufficient amount of ChRM directions per sampling site. Still, assuming the approximation of individual ChRM to primary remanence, these directions combined with great circle paths, were used to construct a magnetostratigraphy.

Polarity zones have been assigned to the FPR, BBGD, SBND, SBN, SBN gap, SBS2 and SBU sections (Fig. 5.2; Appendix I; combined in Fig. 5.4). The first zone is A+ for the exclusively normal ChRM directions in the FPR section. The polarity of the lower 11 m of the BBGD section is uncertain (zone B) because this interval is predominantly characterised by specimens that showed no ChRM; though two ChRM directions suggest normal polarity, one has a shallow inclination. Two great circles do not reveal an unambiguous original

component. The next 10 m are dominated by normal inclination and a normal zone (C+) has been interpreted, despite three ChRM direction having eastward or southward declination. A reversed polarity zone (D-) was inferred for southerly and downward or shallow directions in the upper part of the section. In the SBND section the ChRM directions are normal, though wide spread; great circles, contrarily, indicate a reversed primary component, so polarity is uncertain (E). The ChRM directions at the base of the SBN section are mostly upward or shallow and south- or eastward (ignoring one clearly normal direction) and great circles indicate a reversed characteristic component, so a reversed zone was interpreted there (F-). Above, the majority of directions is normal while a great circle path is unclear, so normal polarity (H+) was assigned. Reversed zone I- was interpreted for dominantly reversed ChRM directions and convincing great circle paths in the middle part of the SBN section, while a normal zone (K+) is indicated for downward though westward or more southward directions above. Near the top of the section most specimens did not yield a ChRM; a single medium stability ChRM and an unclear great circle make the polarity uncertain (L). Polarity of the SBN gap section is also uncertain (M) because ChRMs approximate normal direction, but great circles indicate reversed directions.

In the SBS2 section, above the Willwood-Tatman Fm. boundary, ChRM directions are closer to normal polarity, but have a wide spread and few have the expected normal direction. Many specimens describe a great circle path and some of those clearly move to a reversed direction. It is important to note that all SBS2 specimens were subjected to AF treatment which has difficulty demagnetising hematite, the probable carrier of normal overprint. For these reasons a reversed polarity is assumed (N-). The sampling resolution in the SBU section is poor and ⅓ of specimens did not yield a ChRM or great circle. Two ChRMs near the base possess normal polarity (normal zone O+), but the middle of the section is characterised by ChRMs with downward to shallow inclination and eastward to westward declination and by unclear great circle paths, thus polarity is uncertain there (P). A normal zone (Q+) was assigned to the top of the section as ChRMs approximate normal directions in spite of one positive inclination.

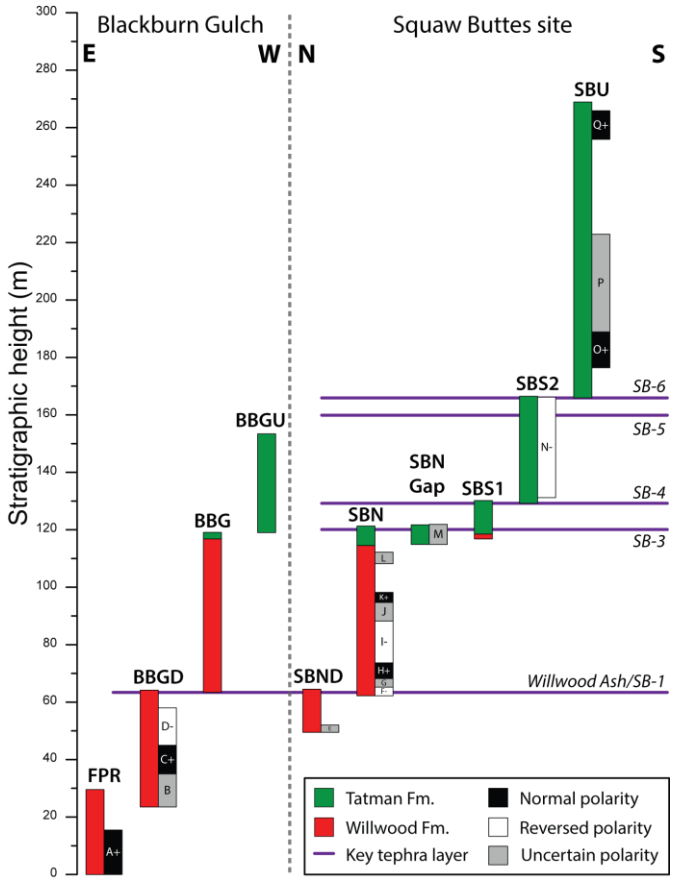

Figure 5.2 *- Overview of magnetostratigraphic interpretations. Composite section showing stratigraphic positions of sections, key tephras and interpreted magnetozones. Section abbreviations in Table 3.1.*

5.3 Astrochronology

5.3.1 Cyclostratigraphy

Time series analysis of detailed stratigraphy and high resolution colour records - combined with independent $^{40}Ar/^{39}Ar$ geochronology - allow a test for the presence of astronomically forced cyclicity in the upper part of the Willwood Fm. and lower part of the Tatman Fm. and, if reliable, the construction of a floating astrochronological timescale. Firstly, the sedimentary cyclic units as well as their vertical and lateral variability need to be established and interpreted. The cyclic unit of the Willwood Fm. at Blackburn Gulch generally consist of 1) a sandstone and mudrock interval exhibiting no or weak pedogenesis and 2) a mudrock interval containing one or several more strongly developed paleosols. These are interpreted as (1) avulsion deposits associated with relatively high accumulation rate and (2) slowly accumulated overbank deposits, following Kraus (2001) and Abels et al. (2013). The cyclic

units are relatively easily recognisable in the lower half of the Blackburn Gulch composite where overbank deposits contain several metres of stacked paleosols and the relatively thin avulsion deposits display weak pedogenic alteration. In the upper half of the composite section, the main paleosol intervals are typically 2 m thick and well developed paleosols are frequent in between, as demonstrated by the 4.4 m spectral filters. This obstructs the designation of cyclic units in the upper half and, consequently, the designation of a uniform cyclicity throughout the section. Two scenarios are presumed: I) stable supra-cycle sedimentation rate throughout the upper Willwood Fm. - thus uniform cycle thickness - and variability in avulsion deposit pedogenesis caused by variable avulsion accumulation rates and/or drainage; II) decreased supra-cycle sedimentation rate in the upper part of the composite introducing distinctly thinner cyclic units there.

In scenario I cycle thickness along section must correspond to the clearer cyclic units of the lower half of the section, since the high paleosol frequency is not present in the lower half. Fifteen cycles are recognised and labelled relative to the Willwood Ash in Fig. 4.15; this cyclicity is best expressed by the ~7.4 m redness (a*) filter. Cyclic units range from 5.1 m to 10.3 m in thickness and average 7.8 m with 1.7 m standard deviation. Cycle -3 does not contain a distinctive paleosol, but the clay and carbonaceous shale at the top of the unit is interpreted to be the distal equivalent of an overbank deposit (Abels et al., 2013; their Fig. 7). For scenario II, ~7.4 m cycles -7 to 1 are sustained; above, the cyclicity is best described by the ~4.4 m SDI, lightness (L*) and redness filters and labelled in Fig. 4.15. Thickness of cycles A to I ranges from 3.2 m to 5.3 m averaging 4.4 m with 0.7 m standard deviation. The SBN section is the lateral equivalent of the upper part of the Blackburn Gulch composite and contains, contrary to the composite, also the dated Tatman tephras. Effort was made to correlate the stratigraphy of both sites on cyclic unit-scale, but proved to be complicated (Fig. 5.3). Van der Meulen et al. (2020) were able to correlate individual cyclic units of two sections at Polecat Bench 8 km apart, though reported metre-scale lateral thickness variations and perturbing sandstones. The distance between the sections here - ~16 km - makes unambiguous correlation impossible due to large variability in for example the appearance of paleosol units.

The cyclic unit of the Tatman Fm. in the Squaw Buttes South 2 section comprises a metre-scale fining upward sequence from sandstone to mudrock with no or weak pedogenesis and carbonaceous shale. The coarse base is interpreted to have been deposited at high accumulation rates while the finer lithologies are related to slow rates, similar to the avulsion-overbank model of the Willwood Fm. Accordingly, the Willwood fluvial system is interpreted to continue essentially undisturbed in the lower part of the Tatman Fm., solely abandoning intense paleosol formation and starting palludial deposition in the overbank phase. The fining upward sequences are best approximated by the ~6 m GSI and lightness filters specifying five cycles labelled in Fig. 4.16. Resulting cyclic units vary between 4.9 m and 8.8 m thick and average 6.5 m (1.3 m standard deviation). The less detailed logs of the SBU section inhibit recognition of a uniform cyclic unit throughout the Tatman Fm. at Squaw Buttes, although light coloured sandstones occur at relatively stable intervals of 7-8 m in the SBU section. The Tatman Fm. at Blackburn Gulch (BBGU section) is supposed to be the lateral equivalent of at least part of the SBS2 section, but contains little sandstone. Identifying fining upward sequences that correlate to Squaw Buttes is unreliable based on the obtained log.

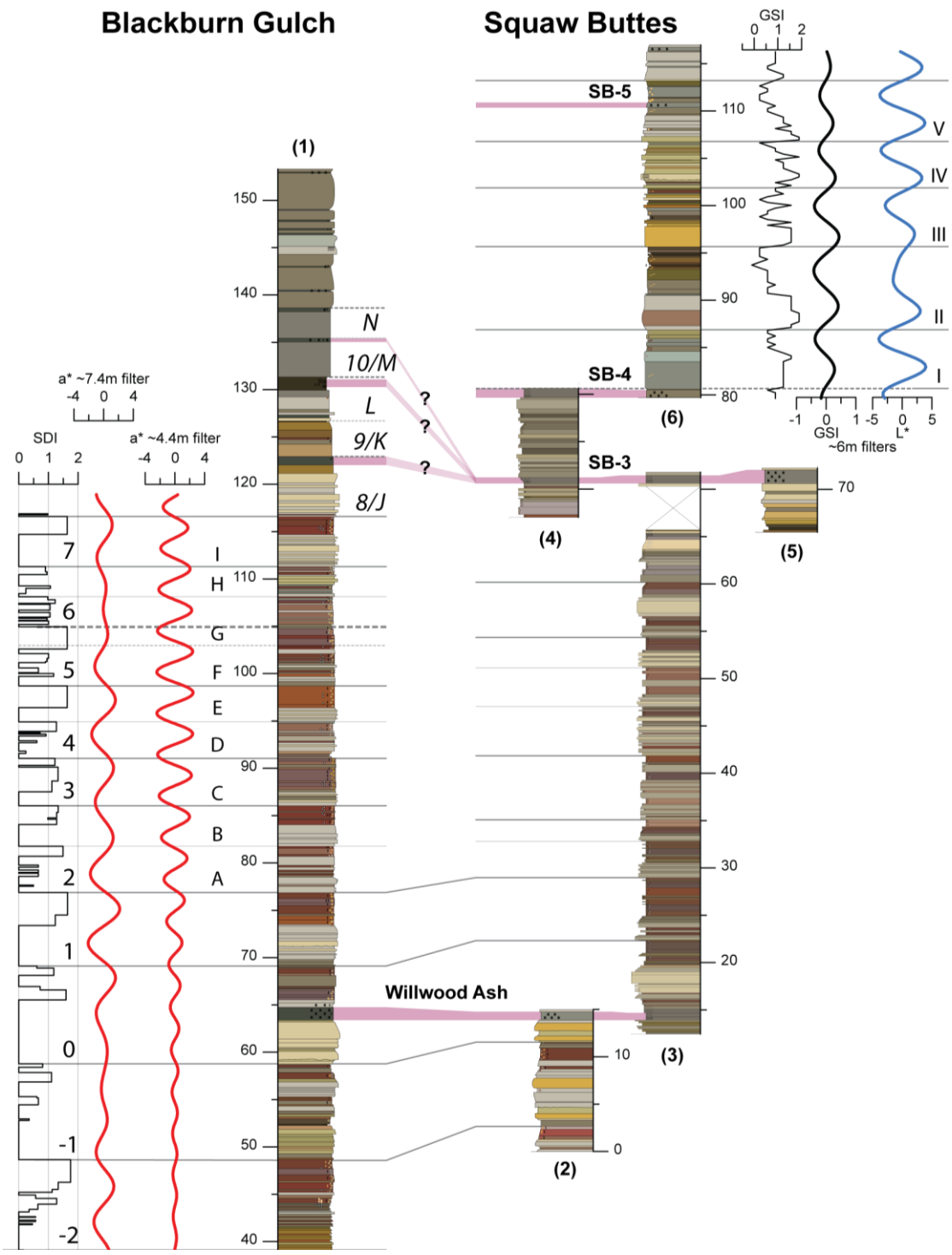

Figure 5.3 *- Correlation of Blackburn Gulch and Squaw Buttes sections; tephras in purple bars and cyclic units outlined by grey lines. (1) Blackburn Gulch composite (BBGD, BBG and BBGU sections); SDI, filters and labels on the left side from Fig. 4.15. Extension of cylcic unit labelling on right side. Possible positions of SB-3 in the Blackburn Gulch stratigraphy are displayed. Squaw Buttes sections are SBND (2), SBN (3), SBS1 (4), SBN gap (5) and SBS2 (6). GSI, filters and cyclic unit labelling next to (6) from Fig. 4.16.*

5.3.2 Time domain

Cyclicity in the stratigraphic domain is translated to the time domain based on cycle counting and the duration of section segments derived from the new $^{40}Ar/^{39}Ar$ ages (Tables 5.1 and 5.2), assuming stable sedimentation rates within these segments. The stratigraphic position of SB-3 in the Blackburn Gulch composite was estimated to obtain a duration for the cyclostratigraphic records in this section. Bed-to-bed correlation is impossible, but similar thicknesses of paleosols, heterolithic units and probably also cyclic units in the SBN section suggests that sedimentation rates at the two sites were similar, too (Fig. 5.3). Moreover, van der Meulen et al. (2020) concluded that, despite lateral variations on cyclic unit scale, overall sedimentation rate was very similar for their parallel sections. Accordingly, SB-3 was linked to a (possible) bentonite at similar stratigraphic height, discarding the possibility that SB-3 at Blackburn Gulch was removed by erosion. Cycles were interpreted for the basal part of the Tatman Fm., so a cycle duration can be calculated for different options for the SB-3 position (Table 5.1). The cyclostratigraphy of the SBS2 section is constrained by SB-4 and SB-5. SB-4 lies just below or at the base of cycle I and SB-5 lies within cycle V, so the time elapsed between the two tephras corresponds to 4-5 cycles (Table 5.2). The vertical proximity and relatively large error on the SB-5 age gives a wide range for the cycle duration. To give a more general approach, Willwood and Tatman Fm. cycle duration has also been calculated using the sedimentation rate between the Willwood Ash and SB-5 (Table 5.1 and 5.2).

Option	**Lower bound**	**Upper bound**	**Duration**	**Strat. height**	**Sed. rate**	**Number of cycles (~7.4m; ~4.4m)**	**Cycle duration**
SB-3 is bed at 122.1 m	52.53 ± 0.04 Ma; 63.4 m	52.20 ± 0.04 Ma; 122.1 m	330 ± 80 kyr	58.7 m	178m/Myr	8.5; 11.5	39 ± 9 kyr; 29 ± 7 kyr
SB-3 is in carbonaceous shale at ~130.5 m	52.53 ± 0.04 Ma; 63.4 m	52.20 ± 0.04 Ma; 130.5 m	330 ± 80 kyr	67.1 m	203 m/Myr	9.5; 13.5	35 ± 8 kyr; 24 ± 6 kyr
SB-3 is bed at 135.1 m	52.53 ± 0.04 Ma; 63.4 m	52.20 ± 0.04 Ma; 135.1 m	330 ± 80 kyr	71.7 m	217 m/Myr	10; 14.5	33 ± 8 kyr; 23 ± 6 kyr
Option	**Lower bound**	**Upper bound**	**Duration**	**Strat. height**	**Sed. rate**	**Average cycle thickness**	**Cycle duration**
Willwood Ash - SB-5	52.53 ± 0.04 Ma; 63.4 m	51.94 ± 0.09; 159.9 m	590 ± 130 kyr	96.5 m	164 m/Myr	7.8m; 4.4m	48 ± 11kyr; 27 ± 6 kyr

Table 5.1 *- Calculation of cycle duration in the Willwood Fm. at Blackburn Gulch.*

Option	Lower bound	Upper bound	Duration	Strat. height	Sed. rate	Number of cycles	Cycle duration
4 cycles between SB-4 and SB-5	52.08 ± 0.04 Ma; 79.7m	51.94 ± 0.09 Ma; 110.4m	140 ± 130 kyr	30.7m	219 m/Myr	4	35 ± 33 kyr
5 cycles between SB-4 and SB-5	52.08 ± 0.04 Ma; 79.7m	51.94 ± 0.09 Ma; 110.4m	140 ± 130 kyr	30.7m	219 m/Myr	5	28 ± 26 kyr
Option	**Lower bound**	**Upper bound**	**Duration**	**Strat. height**	**Sed. rate**	**Average cycle thickness**	**Cycle duration**
Willwood Ash - SB-5	52.53 ± 0.04 Ma; 63.4m	51.94 ± 0.09 Ma; 159.9m	590 ± 130 kyr	96.5m	164 m/Myr	6.5m	40 ± 9 kyr

Table 5.2 *- Calculation of cycle duration in the Tatman Fm. at Squaw Buttes.*

5.3.3 Astronomical forcing

Cyclicity, constrained in both stratigraphic and time domain, needs to be causally linked to oribital periodicities and their forcing. Although metre-scale Willwood Fm. cyclicity was initially associated with autocyclic fluvial processes (simple pedofacies sequences; Kraus, 1987), Kraus and Aslan (1993) hypothesized a relation to climate oscillations caused by precession cycles. Time series analysis of Abdul Aziz et al. (2008), Abels et al. (2012, 2013, 2016), Westerhold et al. (2018) and van der Meulen et al. (2020) confirmed the temporal link, but the exact forcing of ~21 kyr precession on Willwood Fm. avulsion-overbank cyclicity - and, consequently, their phase relation - is unclear. Abels et al. (2013) postulate that regional avulsion was triggered by either increased seasonality or increased strength of the North American monsoon during precession minima through increased flood frequency and/or magnitude. This study presents the first cyclostratigraphic analysis of the Tatman Fm. and no mechanistic and orbital forcing models have been hypothesized. Here, the mechanistic avulsion-overbank model is simply expanded to the basal part of the Tatman Fm. based on the fluvial character and comparable thickness of the cyclic units.

5.3.4 Precession-based timescale

Vvan der Meulen et al. (2020) determined an average precession cycle duration of 20.66 ± 1.9 kyr for the Paleocene-Eocene. The duration of the ~4.4 m Willwood Fm. cyclicity thus coincides with the duration of precession cyclicity; the duration of the ~7.4 m cycles is too long; and the duration of the ~6 m cycles in the Tatman Fm. might correspond to the precession cycle duration. The ~4.4 m cyclicity best represents precession, but cyclicity of this thickness is only present in the upper part of the Willwood Fm. sections, suggesting trends in sedimentation rate and/or unstable translation of precessional forcing into the

depositional environment. The construction of a reliable precession-based timescale is therefore severely obstructed.

If precession-induced cyclicity is assumed to be present throughout the new sections, then precession might have been marked by the ~7.4 m cyclicity in the lower part of the Willwood Fm. sections due to high sedimentation rate (380 m/Myr). Sedimentation rate dropped to 210 m/Myr after deposition of the Willwood Ash so precession was recorded in the ~4.4 m cycles. The Willwood-Tatman Fm. boundary zone is subsequently characterised by condensation and possibly non-deposition, supported by the duration between SB-3 and SB-4 (Fig. 5.1) indicating a sedimentation rate of 75 m/Myr and a precession-induced cycle thickness averaging 1.5 m. Another possibility is that the sedimentation rate throughout the Willwood Fm. is uniformly high, so precession was consistently recorded in the ~7.4 m cycles and the Willwood-Tatman boundary contains a paraconformity of ~160 kyr. In either case, after deposition of SB-4 sedimentation rate returned to higher values (310 m/Myr) and precession produced ~6 m cyclicity. Time control and cyclostratigraphy are unfortunately not extensive enough to confidently asses these possibilities.

Precession-based age models have been successfully constructed for the lower Willwood Fm. in the northern part of the Bighorn Basin (Abdul Aziz et al., 2008; Abels et al., 2012, 2013; Westerhold et al., 2018; van der Meulen et al., 2020), but sections in the central part of the basin (i.e. Red Butte, Abdul Aziz et al., 2008; and Basin Substation core, Westerhold et al., 2018) presented ambiguity (Table 5.3). Independent time control in the northern part of the basin (duration of C24r) implies a sedimentation rate that allows the link between cyclostratigraphy and precession (Abdul Aziz et al., 2008; Abels et al., 2013). Additionally, precession cyclicity is corroborated by indication of eccentricity modulation (Abels et al., 2013; Westerhold et al., 2018) and is in agreement with eccentricity forcing of hyperthermals (Abels et al., 2016). Abdul Aziz et al. (2008), on the other hand, found cyclicity of similar period at Red Butte, but magnetostratigraphy of Tauxe et al. (1994) and Clyde et al. (2007) indicates a sedimentation rate too low to allow coupling of this period to precession. To overcome this problem, they compared mammal evolutionary trends between Red Butte and the northern part of the basin and concluded that sedimentation rates were approximately the same at both sites. Westerhold et al. (2018) also identified

cyclicity of similar period in the Basin Substation core, but these cycles were not persistent throughout the core which they attributed to strong variations in sedimentation rate, condensed intervals and/or irregularities in their cyclostratigraphic proxy.

Strikingly, all studied Willwood Fm. sites, including this study, are (partly) characterised by cycles with periods averaging between 6.8 and 8.7 m, though long term sedimentation rates are expected to differ throughout the basin (Clyde et al., 2007). This raises the questions to what extent the avulsion-overbank cyclicity is related to either precession forcing or autocyclic fluvial processes; if there is a sedimentation rate-threshold above which precession can be recorded in the depositional system; and, subsequently, what the basin-wide variability therein is. It is therefore pivotal to assess the age models for the central part of the basin that are primarily based on uncertain magnetostratigraphy of Tauxe et al. (1994) and Clyde et al. (2007), and to revaluate sedimentation rates.

Study	**Section**	**Cyclo-stratigraphic records**	**Cycle period (m)**	**Time control**	**Sedimentation rate (m/Myr)**	**Precession control inferred?**
Polecat Bench						
Abdul Aziz et al. (2008)	Polecat Bench (PCB)	a*	**7.7/7.4;** 3.3	Duration C24r, P-E boundary, FAD *bunophorus*	391	Yes
Westerhold et al. (2018)	Polecat Bench core (PCB)	a*, XRF Fe	**8.2;** 3.45; 1.2; 1.02; 0.58	PETM, linking cyclostratigraphy to PCB outcrop (Abdul-Aziz et al., 2008)	363	Yes
van der Meulen et al. (2020)	Polecat Bench (PCB)	L*, a*, b*, SDI	**7.6**	PETM, linking cyclostratigraphy to precession	360	Yes
van der Meulen et al. (2020)	Head of Big Sand Coulee (HBSC)	L*, a*, b*, SDI	**8.0**	PETM, linking cyclostratigraphy to precession	380	Yes
McCullough Peaks area						
Abels et al. (2012)	Upper Deer Creek (UDC)	a*	**7.0**	ETM2, H2, fossil record (Biohorizon B), C24r-C24n reversal	340	Yes
Abels et al. (2012)	Gilmore Hill (GH)	-	-	H2, fossil record (Biohorizon B), C24r-C24n reversal	-	-
Westerhold et al. (2018)	Gilmore Hill core (GMH)	a*, XRF Fe	**7.5-6.7;** 3.3; 2.5; ~1; 0.62	PETM, ETM2; linking cyclostratigraphy to UDC and GH outcrop (Abels et al., 2012)	359	Yes
Abels et al (2013)	Deer Creek Amphitheater (DCA)	L*, a*, SDI	**7.1;** 2.1-3.2	Duration C24r; Duration Wa4; Cycle counting between ETM2 and H2 in UDC (Abels et al., 2012)	391 ± 21; 288 ± 20; 316 ± 41	Yes
Abels et al (2016)	Creek Star Hill (CSH)	-	**~7.1**	ETM2, H2, I1, I2; linking cyclicity to precession	~350	Yes
Abels et al (2016)	West Branch (WB)	-	**~7.1**	ETM2, H2, I1, I2; linking cyclicity to precession	~350	Yes
Central Bighorn Basin						
Abdul Aziz et al. (2008)	Red Butte (RB)	a*	**8.7;** 2.6	Base C24, FAD *bunophorus,* Willwood Ash; Base C24r, top C24n, FAD *bunophorus*, Willwood Ash; Evolutionary trends compared to PCB (Abdul Aziz et al., 2008)	238; 259; Similar to PCB	Yes
Westerhold et al. (2018)	Basin Substation core (BSN)	a*, XRF Fe	6.8; 3.3; 2; 1.7; 1.25; 1.05; 0.58	-	-	Unclear: cycles not persistent

Table 5.3 *(previous page) - Summary of previous cyclostratigraphic studies in the Bighorn Basin.*

5.4 Age model central Bighorn Basin

5.4.1 Chronostratigraphic framework

Since the new magneto- and cyclostratigraphy suffer large uncertainties, the $^{40}Ar/^{39}Ar$ chronology serves as the primary tie for the Blackburn Gulch and Squaw Buttes sections to the GTS 2020 (Fig. 5.4); note that the external error should be taken into account for intercomparison. Further, the Willwood Ash was used as correlative datum to link the composite of Tauxe et al. (1994) to this study, marking poor overlap of magnetostratigraphy between the two studies: firstly, the ash is part of a reversed polarity zone in this study, but belongs to a normal zone in Tauxe et al. (1994). However, the Willwood Ash is positioned in between reversed and normal polarity sites in Tauxe et al. (1994), so this discrepancy can be readily explained by their tentatively placed polarity boundary. Secondly, the magnetostratigraphy of both studies below this ash shows a resemblance, but the boundaries do not exactly overlap. Thirdly, above the Willwood Ash, Tauxe et al. (1994) predominantly recognised normal polarity, whereas in this study polarity is mostly reversed.

Comparing both studies to the GTS 2020, in which the Willwood Ash age indicates the C24n.1n-C23r reversal, the existence of reversed zones just below the ash is problematic as reversed overprints have not been reported in the Bighorn Basin. The reversal can be placed in the magnetostratigraphy of this study (C+/D- boundary), but then remains enigmatic in Tauxe et al. (1994). Moreover, the first appearance datum of *Heptodon*, marking the start of the Wa6 biozone, is positioned in the middle of C24n.3n in Tauxe et al. (1994), but in the GTS 2020 Wa6 starts at the top this Chron, adding to the confusion. From the fossil locality map published in Gingerich and Clyde (2001) it is apparent that sections of this study are located exclusively among Wa6 and Wa7 fossil sites. The ages of SB-3, SB-4 and SB-5 place them in the upper part of C23r of the GTS 2020, so the base of magnetozone O+ might be interpreted as the base of C23n.2n and the two small normal zones below (H+ and K+) as normal overprints. Again, the zones of Tauxe et al. (1994) do not fit this interpretation.

It is important to note that the magnetozones of Tauxe et al. (1994) and the Willwood Ash age of Smith et al. (2014; Fig. 5.4) still corroborate the original magnetostratigraphic

interpretation of Tauxe et al. (1994) when linked to the GTS 2020. This alternative challenges the validity of the $^{40}Ar/^{39}Ar$ analyses of this study, as well as the interpretation of magnetozones. To address the validity, the $^{40}Ar/^{39}Ar$ data of this study, of Smith et al. (2004) and the recalculation of Smith et al., (2014) should be thoroughly re-analysed. For now, however, the discrepancies remain unexplained and the $^{40}Ar/^{39}Ar$ geochronology for the new sections is considered valid (as discussed in section 5.1).

Fig. 5.4 additionally displays the other cyclostratigraphic section in the central part of the basin and upper part of the Willwood Fm.: Red Butte of Abdul Aziz et al. (2008; Basin Substation of Westerhold et al. (2018) spans the PETM). Abdul Aziz et al. (2008) provides little information on the stratigraphic position of the section, but states it yields Wa6 fauna. Therefore it is tentatively placed in the middle of the Wa6 biozone of the GTS 2020 and its precession based duration is indicated. Also the stratigraphically highest section of the northern part of the basin, the McCullough Peaks composite of Abels et al. (2016), is included and is tied to the GTS 2020 through hyperthermals evident from its $\delta^{13}C$ record, corroborated by magnetostratigraphy (Abels et al., 2012).

Figure 5.4 *(next page) - Chronostratigraphic framework for the central Bighorn Basin. See text for discussion. Tephra correlation in pink, magnetostratigraphic correlation in black, hyperthermal correlation in green and cyclostratigraphic correlation in blue. GTS 2020 (left) and 2004 (right) start at the Paleocene-Eocene boundary. Hyperthermals from Francescone et al. (2019) except the PETM (from Speijer et al., 2020), H2, I1 and I2 (from Westerhold et al., 2017).* $^{40}Ar/^{39}Ar$ *ages display 2σ internal error; 2σ full external error for the Willwood Ash is also plotted (SB-3, SB-4 and SB-5 have similar external errors). The Willwood Ash is tied to the GTS 2004 using the age of Smith et al. (2014). To the right of the new composite the ~7.4 m and ~4.4 m redness filters and ~6 m GSI filter are drawn. The magnetostratigraphic interpretations of (1) Tauxe et al. (1994) and (2) Clyde et al. (2007) are indicated.*

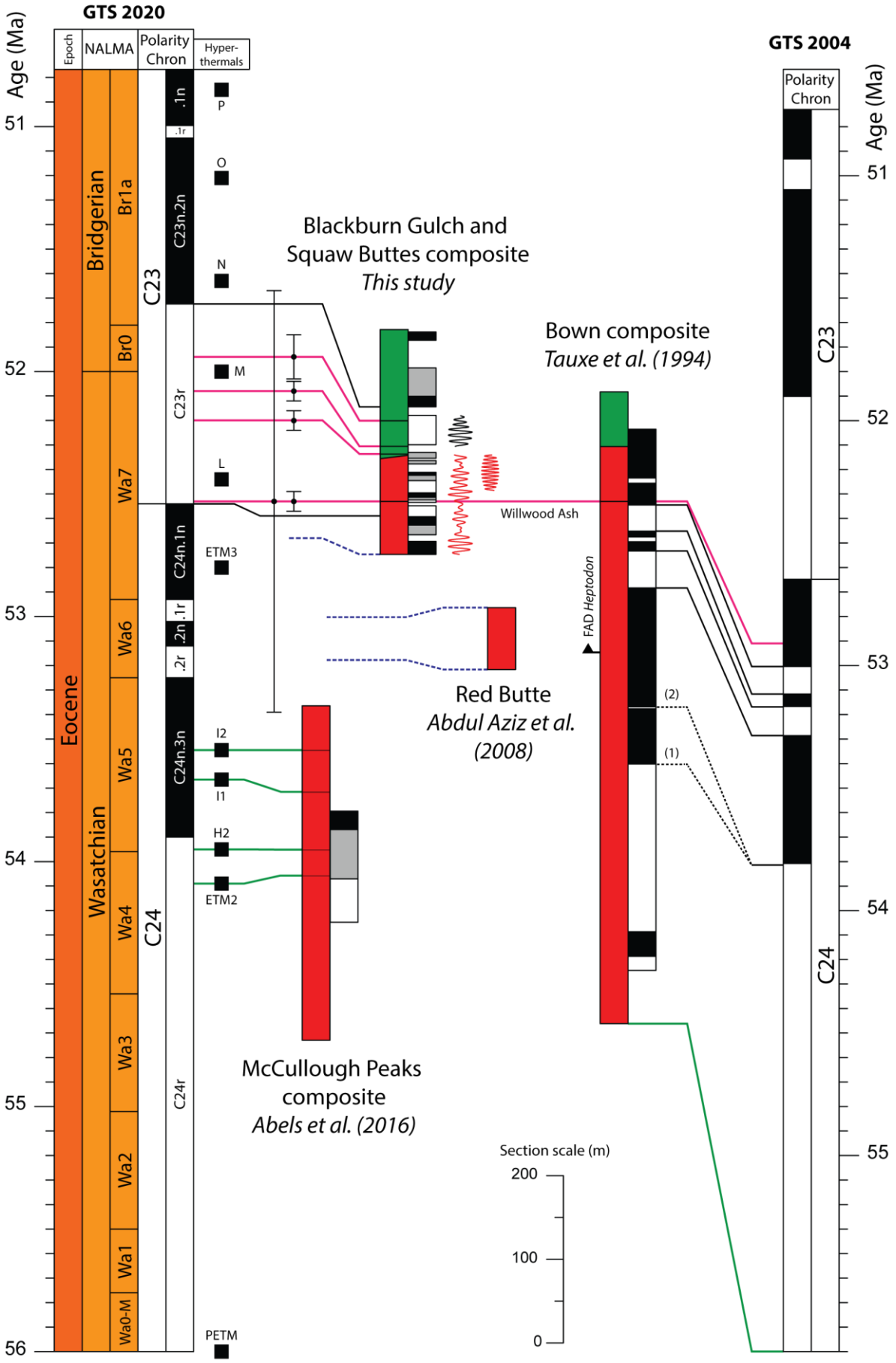
GTS 2020
Age (Ma)
Epoch
NALMA
Polarity Chron
Hyper-thermals
Eocene
Bridgerian
Wasatchian
Br1a
Br0
Wa7
Wa6
Wa5
Wa4
Wa3
Wa2
Wa1
Wa0-M
C23
C24
C23n.2n
C23r
C24n.1n
C24n.3n
C24r
.1n
.1r
.2n
.2r
P
O
N
M
L
ETM3
I2
I1
H2
ETM2
PETM
51
52
53
54
55
56
Blackburn Gulch and
Squaw Buttes composite
This study
Willwood Ash
Red Butte
Abdul Aziz et al.
(2008)
McCullough Peaks
composite
Abels et al. (2016)
Bown composite
Tauxe et al. (1994)
FAD Heptodon
(2)
(1)
GTS 2004
Polarity Chron
Section scale (m)
200
100
0

5.4.2 Precession forcing in the Willwood Fm.

The chronostratigraphic framework and the GTS 2020 allow a revaluation of the sedimentation rate of Red Butte (Abdul Aziz et al., 2008) and, subsequently, an independent test for precession forcing of avulsion-overbank cycles there and in the Willwood Fm. in general. The 8.7 m thick cycles at Red Butte require a sedimentation rate of ~420 m/Myr to confirm precession control. Taking the magnetostratigraphic interpretations of Tauxe et al. (1994) and Clyde et al. (2007) - placing the base of Chron C24n either at 310 m or 380 m in the Tauxe et al. (1994) stratigraphy, and the Willwood Ash at 620 m - the updated time control (i.e. base C24n at 53.900 Ma (GTS 2020) and age of the Willwood Ash 52.53 Ma (this study)) yields sedimentation rates of 226 m/Myr or 175 m/Myr. Alternatively, the start of Wa6 (FAD of *Heptodon* at 440 m in Tauxe et al., 1994), which coincides with the base of C24n.2r in GTS 2020 (53.250 Ma), can be combined with the Willwood Ash yielding a rate of 250 m/Myr. As these rates are too low and no other reliable and continuous sedimentation rate can be established from the sections of this study or Tauxe et al. (1994), precession control in the Willwood Fm. cannot be confirmed here.

5.4.3 Future carbonate nodule $\delta^{13}C$

The presented age model provides time control for future $\delta^{13}C$ records from carbonate nodules that were sampled during fieldwork of this study (Appendix III for sample list). The base of the composite section in Fig. 5.4 is tied to the GTS 2020 based on precession-forced cycle counting below the Willwood Ash, but since this control is not corroborated by sedimentation rates, it should be regarded as oldest limit. The future $\delta^{13}C$ record will then cover the (upper half) of C24n.1n and lower third of C23r, possibly including hyperthermals ETM3 and L. Thus central Bighorn Basin outcrops in general can contribute to the extension of the paleosol $\delta^{13}C$ record of Abels et al. (2016) to at least hyperthermal L. Furthermore, the future $\delta^{13}C$ record will provide additional time control through correlation to marine records and, therefore, provide a test for the presented chronostratigraphic framework.

5.4.4 Willwood-Tatman Fm. boundary

The transition from the Willwood to Tatman Fm. in the Blackburn Gulch and Squaw Buttes sections is evident from the abrupt lack of colourful paleosol B-horizons in the latter - although weak pedogenesis and sparse paleosols still persist - and higher prominence of carbonaceous shales. At the squaw Buttes site the fining-upward sequences in the Tatman

Fm. are similar to deposits in the Willwood Fm., suggesting a continuation of the fluvial system but a switch in floodplain conditions. The Tatman Fm. base is not isochronous, however, as 1) the highest prominent paleosol in different Squaw Buttes sections differs several metres in stratigraphic position, 2) the formation boundary is placed 10 m higher relative to the Willwood Ash in Tauxe et al. (1994) and 3) tongues of paleosol strata in the lower part of the Tatman Fm. have been reported (Rohrer and Smith, 1969; van Houten, 1944). Intertonguing of the Willwood and Tatman Fm. is also inferred from basin-wide stratigraphic reconstructions (Rohrer and Smith, 1969; Bown, 1982), but the exact temporal scale hereof is not clear. A similar but opposite transition in fluvial deposits, from dominant palludial to varicoloured pedogenic, is observed at the conformal boundary between the Fort Union and Willwood Fm. (Wing and Bown, 1985). Small scale diachroneity of this transition was linked to lateral paleogeographical and structural differences, whereas the overall emergence of intense pedogenesis was attributed to a climate trend from warm and moist to subtropical and seasonally dry in the late Paleocene (Wing and Bown, 1985). This raises the question if the Willwood-Tatman Fm. transition is related to global or regional climatic shifts, too.

The paleoclimate record of Wing et al. (1991) indicates that the Fort Union-Willwood Fm. and Willwood-Tatman Fm. boundaries are comprised within the same long term warming trend; supported by the new age model which places the latter boundary within but below the peak of the EECO (Speijer et al., 2020). It is apparent from the $^{40}Ar/^{39}Ar$ geochronology that at least the basal part of the Tatman Fm. is characterised by condensed and/or non-deposition. Moreover, the emergence of a higher frequency cyclicity (~4.4 m) above the Willwood Ash indicates that sedimentation rates in the upper 50 m of the Willwood Fm. were already declining. This suggests that formation boundary is linked to changes in accommodation space or sediment supply caused by tectonics. Increased volcanism around the basin, evident from frequent tephras in the Tatman Fm., might be linked to these structural changes. Therefore the Willwood-Tatman Fm. transition is primarily associated with long term structural trends observed in several Laramide basins (ponded basins of Dickinson et al., 1988), rather than global events. Possible drainage restriction might have caused hydrological changes in the basin that increased floodplain wetness and thus

restricted paleosol formation, while the fluviatile depositional system could continue fairly undisturbed.

6. Conclusion

A new composite section in the central Bighorn Basin is presented comprising detailed sedimentology and stratigraphy, tephrochronology, magnetostratigraphy and cyclostratigraphy. High-precision single grain $^{40}Ar/^{39}Ar$ ages were produced for the Willwood Ash and three new tephra layers providing time control independent from magnetostratigraphy and biostratigraphy of previous studies. The Willwood Ash approximately coincides with the C23-C24 reversal, placing the upper part of the Willwood and lower part of the Tatman Fm. in a younger timeframe. However, ambiguous magnetostratigraphy of this study, troubled by persistent normal overprints, preclude confident correlation to the composite of Tauxe et al. (1994) and obstruct the assessment of uncertainties in their chronology. The poor magnetostratigraphic framework also limits the use of the $^{40}Ar/^{39}Ar$ geochronology outside the basin.

Cyclostratigraphic analysis revealed avulsion-overbank cyclicity in the Willwood Fm. of similar thickness as previously found in the northern part of the basin where it is linked to ~21 kyr precession forcing. $^{40}Ar/^{39}Ar$ geochronology and bandpass filters indicate condensed or non-deposition in the Willwood-Tatman Fm. boundary zone, severely hampering cyclostratigraphic translation into the time domain. Revision of the central Bighorn Basin chronostratigraphy yields sedimentation rates too low to allow coupling of the avulsion-overbank cycles and precession, and consequently challenges precession control on the Willwood Fm. stacking pattern. This study additionally contributes a cyclostratigraphic record from the Tatman Fm. identifying rhythmic fining-upward sequences that might correspond to the duration of precession cycles.

Carbonate nodules sampled from the composite provide future extension of the Bighorn Basin $\delta^{13}C$ record; the new age model suggests that the composite encompasses hyperthermal L and implies that also ETM3 can be sampled in the central Bighorn Basin.

The Willwood-Tatman Fm. transition - marked by the disappearance of intense paleosol formation, yet fairly undisturbed fluvial deposition - is constrained to the time just before the peak of the EECO. The transition is not attributed to a specific climatic event or trend but rather to structural dynamics leading to restriction of the Bighorn Basin.

Recommendations

Further actions should be taken to improve the presented chronostratigraphic framework: 1) review $^{40}Ar/^{39}Ar$ data analysis of this study and Smith et al. (2004; recalculated in Smith et al., 2014) to explain inconsistent ages between samples of this study and the ~0.5 Ma older age of Smith et al. (2004, 2014), so a definitive age for the Willwood Ash can be established. 2) Carry out an extensive paleomagnetic study in the top of Willwood and Tatman Fm. with the aim to understand magnetic carriers, secondary NRM components and to design a reliable magnetostratigraphic procedure. Remaining paleomegnetic samples from this study can be used. It is recommended that at least three specimens from a single sampling site are analysed in future magnetostratigraphic studies in the central basin. 3) For now, magnetostratigraphy in this part of the basin should be considered unreliable. To connect the new sections to the Bown composite (used by Tauxe et al., 1994) in an alternative way, detailed (cyclo)stratigraphic sections should be produced from the Bown composite. The Bown composite constitutes of sections from a wide area in the central and southeast of the basin, so possible sedimentation rate differences throughout the composite should be taken into account. 4) Analyse paleosol carbonate nodules from the new sections and use resulting $\delta^{13}C$ records for correlation to the hyperthermal timescale. Construction of $\delta^{13}C$ records from the Bown composite will also help the correlation between the Bown composite and the new sections.

Additional research is needed to test the inferred precession control on the Willwood Fm. fluvial stacking pattern. Detailed cyclostratigraphy from the Bown section will allow the construction of long cyclostratigraphic records from the central and south-eastern part of the Bighorn Basin, probably comprising fluvial deposition under various sedimentation rates. If cycles have a (consistent) thickness of 7-8 m there as well, than autocyclic control is most logical and interpretation of precession forcing in the northern basin can be an artefact of fortuitous correspondence of sedimentation rates and cycle thickness. Detailed stratigraphy from the Bown composite can also help to evaluate the presence of hiatuses (or periods of condensed deposition) in the upper part of the Willwood Fm., for this can imply higher sedimentation rates in between hiatuses corroborating precession control. Further, the Willwood Ash outcrops over several 10s of kilometres around Tatman Mountain and Squaw Buttes Divide and therefore provides a reliable lateral timehorizon which can be used to

reconstruct the Willwood Fm. floodplain just before tephra deposition. This allows the evaluation of lateral facies differences and basin-wide synchrony of avulsion and overbank deposition. Satellite or aerial images of higher resolution than Google Earth Pro can considerably assist in outcrop correlation. For future cyclostratigraphic studies, parallel sections are recommended, but this study suggests that a lateral distance of ~16 km is too big to allow confident correlations on cyclic unit scale. Finally, a GSI from the Blackburn Gulch composite should be constructed and compared to the SDI (and their bandpass filters) to evaluate the usefulness of a GSI as cyclostratigraphic record in the Willwood Fm. A GSI can be constructed without additional equipment and can be constructed from existent lithostratigraphic logs of previous studies.

The Tatman Fm. encompasses a high frequency of tephra layers and future high-precision $^{40}Ar/^{39}Ar$ dating can offer extraordinary time control to: 1) address basin-wide chronostratigraphic and structural interpretations of the Tatman Fm. and Tatman-like strata in the marginal parts of the basin (Bown, 1982), including quantifying diachroneity of the Willwood-Tatman Fm. boundary; 2) link Bighorn Basin stratigraphic and structural evolution and chronology to other Laramide basins (specifically the Green River Basin); 3) constrain future climate and carbon cycle proxies from the Tatman Fm. (e.g. leaf margins, n-alkenes from carbonaceous shales); and 4) allow thorough analysis of precession forcing in the Tatman Fm. where longer cyclostratigraphic records should be produced. It is recommended to design $^{40}Ar/^{39}Ar$ age determination from individual crystal dates in advance.

Acknowledgements

First of all, I want to thank my supervisors Antonio Turtù, Klaudia Kuiper and Ron Kaandorp. I thank Antonio specifically for offering me this project, introducing me to the various aspects of integrated stratigraphy in the Bighorn Basin and mentoring me during laboratory and fieldwork. I offer my gratitude to Philip Gingerich, Holly Smith and Tom Churchill and his family for their hospitality, logistical support, materials and sharing their knowledge during fieldwork. I also thank Hemmo Abels for dinner at the Buffalo Bill restaurant in Cody. For $^{40}Ar/^{39}Ar$ analysis, I thank Roel van Elzas at the VU mineral separation laboratory, Klaudia for her guidance on the data analysis and Marjolein Daeter for assistance with ArArCalc. I want to thank Wout Krijgsman for access to the paleomagnetic laboratory at the Fort Hoofddijk, Maxim Krasnoperov for his time and assistance during my paleomagnetic analyses, Mark Dekkers for the AF demagnetization on the robot and Bertwin de Groot for assistance with the Curie balance. I thank Robin van der Velde and Jesper Volmer for their support during the writing of this report.

In this study I also processed samples and data collected in previous fieldwork, so I acknowledge Hemmo Abels, Frits Hilgen, Philip Gingerich, Antonio Turtù and others for previous seasons in the Bighorn Basin. I express my gratitude to the Molengraaff Foundation for a grant partly covering personal fieldwork costs. Also a VU fieldwork grant covered part of my personal costs. Scientific costs were funded by VIDI grant 864.12.005 of Klaudia Kuiper.

References

Abdul Aziz, H., Hilgen, F. J., van Luijk, G. M., Sluijs, A., Kraus, M. J., Pares, J. M., & Gingerich, P. D. (2008). Astronomical climate control on paleosol stacking patterns in the upper Paleocene–lower Eocene Willwood Formation, Bighorn Basin, Wyoming. *Geology, 36*(7), 531-534.

Abels, H. A., Clyde, W. C., Gingerich, P. D., Hilgen, F. J., Fricke, H. C., Bowen, G. J., & Lourens, L. J. (2012). Terrestrial carbon isotope excursions and biotic change during Palaeogene hyperthermals. *Nature Geoscience, 5*, 326-329.

Abels, H. A., Lauretano, V., van Yperen, A. E., Hopman, T., Zachos, J. C., Lourens, L. J., . . . Bowen, G. J. (2016). Environmental impact and magnitude of paleosol carbonate carbon isotope excursions marking five early Eocene hyperthermals in the Bighorn Basin, Wyoming. *Climate of the past, 12*, 1151-1163.

Abels, H., Kraus, M., & Gingerich, P. (2013). Precession-scale cyclicity in the fluvial lower Eocene Willwood Formation of the Bighorn Basin, Wyoming (USA). *Sedimentology, 60*, 1467-1483.

Allmendinger, R. W., Cardozo, N., & Fisher, D. (2012). *Structural geology algorithms: Vectors and tensors in structural geology.* Vambridge University Press.

Andersen, N. L., Jicha, B. R., Singer, B. S., & Hildreth, W. (2017). Incremental heating of Bishop Tuff sanidine reveals preeruptive radiogenic Ar and rapid remobilization from cold storage. *Proceedings of the National Academy of Sciences of the United States of America, 114*(47), 12407-12412.

Bown, T. M. (1980). Summary of Latest Cretaceous and Cenozoic Sedimentary, Tectonic, and Erosional Events, Bighorn Basin, Wyoming. (P. D. Gingerich, Ed.) *Papers on Paleontology, 24*, 25-32.

Bown, T. M. (1982). *Geology, paleontology, and correlation of Eocene volcaniclastic rocks, southeast Absaroka Range, Hot Springs, County, Wyoming.* Washington: United States Government Printing Office.

Butler, R. (1992). *Paleomagnetism: magnetic domains to geologic terranes* (Electronic Edition ed.). Boston: Blackwell Scientific Publications.

Butler, R. F., Gingerich, P. D., & Lindsay, E. H. (1981). Magnetic polarity stratigraphy and biostratigraphy of Paleocene and Lower Eocene continental deposits, Clark's Fork Basin, Wyoming. *Journal of Geology, 89*, 299-316.

Cardozo, N., & Allmendinger, R. W. (2013). Spherical projections with OSXStereonet. *Computers & Geosciences, 51*, 193-205.

Chadima, M., & Hrouda, F. (2006). Remasoft 3.0 – a user-friendly paleomagnetic data browser and analyzer. *Travaux Géophysiques, 27*, 20-21.

Clyde, W. C., Gingerich, P. D., Wing, S. L., Röhl, U., Westerhold, T., Bowen, G., . . . Team, B. S. (2013). Bighorn Basin Coring Project (BBCP): a continental perspective on early Paleogene hyperthermals W. *Scientific Drilling, 16*, 21-31.

Clyde, W. C., Stamatakos, J., & Gingerich, P. D. (1994). Chronology of the Wasatchian Land-Mammal Age (Early Eocene): Magnetostratigraphic Results from the McCullough Peaks Section, Northern Bighorn Basin, Wyoming'. *The journal of Geology, 102*, 367-377.

Clyde, W., Bartels, W., Gunnell, G., & Zonneveld, J.-P. (2004). Discussion and reply: 40 Ar/39 Ar geochronology of the. *GSA Bulletin, 116*(1/2), 251-252.

Clyde, W., Finarelli, J., Wing, S., Schankler, D., & Chew, A. (2007). Basin-wide magnetostratigraphic framework for the Bighorn Basin, Wyoming. *Geological Society of America Bulletin, 119*(7/8), 848-859.

Cohen, E. R., & Taylor, B. N. (1988). The 1986 CODATA Recommended Values of the Fundamental Physical Constants. *Journal of Physical and Chemical Reference Data, 17*, 1795-1803.

Cramer, B. S., Wright, J. D., Kent, D. V., & Aubry, M.-P. (2003). Orbital climate forcing of D13C excursions in the late Paleocene–early Eocene (chrons C24n–C25n). *Paleoceanography and Paleoclimatology, 18*(4), 21 1-25.

DeCelles, P. G. (2004). Late Jurassic to Eocene evolution of the Cordilleran thrust belt and foreland basin system, western U.S.A. *American Journal of Science, 304*, 105-168.

Dickinson, W. R., Klute, M. A., Hayes, M. J., Janecke, S. U., Lundin, E. R., McKittrick, M. A., & Olivares, M. D. (1988). Paleogeographic and paleotectonic setting of Laramide sedimentary basins in the central Rocky Mountain region. *Bulletin of the Geological Society of America, 100*, 1023-1039.

Diehl, J. F., Beck, M. E., Beske-Diehl, S., Jacobson, D., & Hearn, B. C. (1983). Paleomagnetism of the Late Cretaceous Early Tertiary north- central Montana alkalic province (USA). *Journal of Geophysical Research, 88*(B12), 10,593-10,609.

ENSDF database. (2021, June 29). Retrieved 2017, from https://www.nndc.bnl.gov/ensdf/

Fan, M., & Carrapa, B. (2014). Late Cretaceous–early Eocene Laramide uplift, exhumation, and basin subsidence in Wyoming: Crustal responses to flat slab subduction. *Tectonics, 33*, 509-529.

Fisher, R. (1953). Dispersion on a sphere. *Proceedings of the Royal Society of London. Series A, Mathematical and Physical Sciences, 217*(1130), 295-305.

Francescone, F., Lauretano, V., Bouligand, C., Moretti, M., Sabatino, N., Schrader, C., . . . Galeotti, S. (2019). A 9 million-year-long astrochronological record of the early– middle Eocene corroborated by seafloor spreading rates. *Bulletin of the Geological Society of America, 131*(3/4), 499-520.

Gingerich, P. D. (1983). Paleocene-Eocene Faunal Zones and a Preliminary Analysis of Laramide structural Deformation in the Clark's Fork Basin, Wyoming. *Thirty-Fourth Annual Field Conference - Wyoming Geological Association Guidebook*, (pp. 185-195).

Gingerich, P. D., & Clyde, W. C. (2001). Overview of Mammalian Biostratigraphy in the Paleocene-Eocene Fort Union and Willwood Formations of the Bighorn and Clarks Fork Basins. (P. D. Gingerich, Ed.) *University of Michigan Papers on Paleontology, 33*, 1-14.

Hajek, E. A., & Straub, K. M. (2017). Autogenic Sedimentation in Clastic Stratigraphy. *Annual Review ofEarth and Planetary Sciences, 45*, 681-709.

Husson, D. (2014). *MathWorks File Exchange: RedNoise_ConfidenceLevels*. Retrieved from https://www.mathworks.com/matlabcentral/fileexchange/45539-rednoise_confidencelevels

Kennett, J. P., & Stott, L. D. (1991). Abrupt deep-sea warming, palaeoceanographic. *Nature, 353*, 225-229.

Kirschvink, J. L. (1980). The least-squares line and plane and the analysis of palaeomagnetic data. *Geophys. J. R. astr. Soc., 62*, 699-718.

Koch, P. L., Zachos, J. C., & Gingerich, P. D. (1992). Correlation between isotope records in marine and continental carbon reservoirs near the Palaeocene/Eocene boundary. *Nature, 358*, 319-322.

Kodema, K. P., & Hinnov, L. A. (2014). *Rock Magnetic Cyclostratigraphy.* Wiley-Blackwell.

Koppers, A. (2002). ArArCALCFsoftware for 40Ar/39Ar age calculations. *Computers & Geosciences, 28*, 605-619.

Koymans, M. R., Langereis, C. G., Pastor-Galan, D., & van Hinsbergen, D. J. (2016). Paleomagnetism.org: An online multi-platform open source environment for paleomagnetic data analysis. *Computers and Geosciences, 93*, 127-137.

Kraus, M. J. (1987). Integration of channel and floodplain suites, II. Vertical relations of alluvial paleosols. *Journal of Sedimentary Petrology, 57*(4), 602-612.

Kraus, M. J. (2001). Sedimentology and Depositional Setting of the Willwood Formation in the Bighorn and Clarks Fork Basins. (P. D. Gingerich, Ed.) *University of Michigan Papers on Paleontology*(33), 15-28.

Kraus, M. J., & Aslan, A. (1993). Eocene hydromorphic paleosols: Significance for interpreting ancient floodplain processes. *Journal of Sedimentary Petrology, 63*(3), 453-463.

Kraus, M. J., & Hasiotis, S. T. (2006). Significance of Different Modes of Rhizolith Preservation to Interpreting Paleoenvironmental and Paleohydrologic Settings: Examples from Paleogene Paleosols, Bighorn Basin, Wyoming, U.S.A. *Journal of Sedimentary Research*, 633-646.

Kuiper, K., Deino, A., Hilgen, F., Krijgsman, W., Renne, P., & Wijbrans, J. (2008). Synchronizing Rock Clocks of Earth History. *Science, 320*, 500-504.

Kuiper, K., Turtu, A., & Wijbrans, J. (2018). A new branch on the tree of 40Ar/39Ar multi-collector mass spectrometers. *Geophysical Research Abstracts. 20.* EGU2018.

Lauretano, V., Hilgen, F. J., Zachos, J. C., & Lourens, L. J. (2016). Astronomically tuned age model for the early Eocene carbon isotope events: A new high-resolution delta C-13(benthic) record of ODP Site 1263 between similar to 49 and similar to 54 Ma. *Newsletters on Stratigraphy, 49*(2), 383-400.

Lee, J.-Y., Marti, K., Severinghaus, J. P., Kawamura, K., Yoo, H.-S., Lee, J. B., & Kim, J. S. (2006). A redetermination of the isotopic abundances of atmospheric Ar. *Geochimica et Cosmochimica, 70*, 4507-4512.

Lelieveldt, S. (1995). *Determination of Ca- and K-correction factors for 40Ar/39Ar dating for OSU TRIGA and ECN Petten reactors.* Internal report, Vrije Universiteit, Amsterdam, Department of Petrology and Isotope Geology.

Li, M., Hinnov, L., & Kump, L. (2019). Acycle: Time-series analysis software for paleoclimate research and education. *Computers and Geosciences, 127*, 12-22.

Lourens, L. J., Sluijs, A., Kroon, D., Zachos, J. C., Thomas, E., Röhl, U., . . . Raffi, I. (2005). Astronomical pacing of late Palaeocene to early Eocene global warming events. *Nature, 453*, 1083-1087.

Maxbauer, D. P., Feinberg, J. M., Fox, D. L., & Clyde, W. C. (2016). Magnetic minerals as recorders of weathering, diagenesis, and paleoclimate: A core–outcrop comparison of Paleocene–Eocene paleosols in the Bighorn Basin, WY, USA. *Earth and Planetary Science Letters*(452), 15-26.

McElhinny, M. W., & McFadden, P. L. (2000). *Paleomagnetism: continents and oceans* (73 ed.). Elsevier.

McInerney, F. A., & Wing, S. L. (2011). The Paleocene-Eocene Thermal Maximum: A Perturbation of Carbon Cycle, Climate, and Biosphere with Implications for the Future. *Annual Review of Earth and Planetary Sciences, 39*, 489-516.

Miall, A. D., Catuneanu, O., Vakarelov, B. K., & Post, R. (2008). The Western Interior Basin Andrew. In A. D. Miall, *Sedimentary Basins of the World, Volume 5* (pp. 329-362). Amsterdam: Elsevier.

Min, K., Mundil, R., Renne, P. R., & Ludwig, K. R. (2000). A test for systematic errors in 40Ar/39Ar geochronology through comparison with U/Pb analysis of a 1.1-Ga rhyolite. *Geochimica et Cosmochimica Acta, 64*(1), 73-98.

Mokrzycki, W., & Tatol, M. (2009). Perceptual difference in L * a * b * color space as the base for object colour identfication. *1st International Conference on Image Processing & Communications*, (pp. 1-8).

Mullender, T. A., van Velzen, A. J., & Dekkers, M. J. (1993). Continuous drift correction and separate identification of ferrimagnetic and paramagnetic contributions in thermomagnetic runs. *Geophysical Journal International, 114*, 663-672.

Mullender, T., Frederichs, T., Hilgenfeldt, C., de Groot, L. V., Fabian, K., & Dekkers, M. J. (2016). Automated paleomagnetic and rock magnetic data acquisition with an in-line horizontal ‘‘2G’’ system. *Geochemistry, Geophysics, Geosystems, 17*, 3546-3559.

Neasham, J. W., & Vondra, C. F. (1972). Stratigraphy and Petrology of the Lower Eocene Willwood Formation, Bighorn Basin, Wyoming. *Geological Society of America Bulletin, 83*, 2167-2180.

Nier, A. O. (1950). A Redetermination of the Relative Abundances of the Isotopes of Carbon, Nitrogen, Oxygen, Argon, and Potassium. *Phys. Rev., 77*, 789-793.

Noorbergen, L. J., Abels, H. A., Hilgen, F. J., Robson, B. E., de Jong, E., Dekkers, M. J., . . . Kuiper, K. F. (2018). Conceptual models for short-eccentricity-scale climate control on peat formation in a lower Palaeocene fluvial system, north-eastern Montana (USA). *Sediemntology, 65*(3), 775-808.

Pierce, W. G., & Andrews, D. A. (1941). Geology and Oil and Coal Resources of the Region South of Cody, Park County, Wyoming. *U.S. Geological Survey Bulletin, 921-B*, 99-180.

Renne, P. R., Sharp, Z. D., & Heizler, M. T. (2008). Cl-derived argon isotope production in the CLICIT facility of OSTR reactor and the effects of the Cl-correction in 40Ar/39Ar geochronology. *Chemical Geology, 255*(3-4), 463-466.

Renne, P. R., Swisher, C. C., Deino, A. L., Karner, D. B., Owens, T. L., & DePaolo, D. J. (1998). Intercalibration of standards, absolute ages and uncertainties in 40Ar/39Ar dating. *Chemical Geology, 145*(1-2), 117-152.

Rohrer, W. L. Geology of the Sheep Mountain Quadrangle, Wyoming. *U.S. Geological Survey Geologic Quadrangle Map GQ-310.*

Rohrer, W. L. Geology of the Tatman Mountain Quadrangle, Wyoming. *U.S. Geological Survey Geologic Quadrangle Map GQ-311.*

Rohrer, W., & Smith, J. (1969). Tatman Formation. *21st Annual Field Conference Guidebook* (pp. 49-54). Wyoming: Wyoming Geological Association.

Schaen, A. J., Jicha, B. R., Hodges, K. V., Vermeesch, P., Stelten, M. E., Mercer, C. M., . . . Singer, B. S. (2020). Interpreting and reporting 40Ar/39Ar geochronologic data. *GSA Bulletin, 133*(3-4), 461-487.

Secord, R., Gingerich, P. D., Smith, M. E., Clyde, W. C., Wilf, P., & Singer, B. S. (2006). Geochronology and mammalian biostratigraphy of middle and upper Paleocene continental strata, Bighorn Basin, Wyoming. *American Journal of Science, 306*, 211-245.

Shapiro-Wilk Test Calculator. (2017, November). Retrieved March 2021, from Statistics Kingdom: https://www.statskingdom.com/320ShapiroWilk.html

Sinclair, W. J., & Granger, W. (1912). Notes on the Tertiary deposits of the Bighorn Basin. *Bulletin American Museum of Natural History., 31*, 57-67.

Sircombe, K. N. (2004). AgeDisplay: an EXCEL workbook to evaluate and display univariate geochronological data using binned frequency histograms and probability density distributions. *Computers & Geosciences, 30*, 21-31.

Smith, M. E., Carroll, A. R., Scott, J. J., & Singer, B. S. (2014). Early Eocene carbon isotope excursions and landscape destabilization at eccentricity minima: Green River Formation of Wyoming. *Earth and Planetary Science Letters, 403*, 393-406.

Smith, M. E., Singer, B., & Carroll, A. (2003). 40Ar/39 geochronology of the Eocene Green River Formation, Wyoming. *GSA Bulletin, 115*(5), 549-565.

Smith, M., Singer, B., & Carroll, A. (2004). Reply. *GSA Bulletin, 116*(1/2), 253-256.

Speijer, R. P., Pälike, H., Hollis, C. J., Hooker, J. J., & Ogg, J. G. (2020). The Paleogene Period. In F. M. Gradstein, J. G. Ogg, M. D. Schmitz, & G. M. Ogg, *Geologic Time Scale 2020* (2 ed., pp. 1087-1140). Elsevier B.V.

Stacey, F. D., & Banerjee, S. K. (1974). *The Physical Principles of Rock Magnetism.* Amsterdam: Elsevier.

Steenbrink, J., van Vugt, N., Hilgen, F. J., Wijbrans, J. R., & Meulenkamp, J. E. (1999). edimentary cycles and volcanic ash beds in the Lower Pliocene lacustrine succession of Ptolemais (NW Greece): discrepancy between 40Ar/39Ar and astronomical ages. *Palaeogeography, Palaeoclimatology, Palaeoecology, 152*(3-4), 283-303.

Tauxe, L., Gee, J., Gallet, Y., Pick, T., & Bown, T. (1994). Magnetostratigraphy of the Willwood Formation, Bighorn Basin, Wyoming: new constraints on the location of Paleocene/Eocene boundary. *Earth and Planetary Science Letters, 125*, 159-172.

van der Meulen, B., Gingerich, P. D., Lourens, L. J., Meijer, N., van Broekhuizen, S., van Ginneken, S., & Abels, H. A. (2020). Carbon isotope and mammal recovery from extreme greenhouse warming at the Paleocene–Eocene boundary in astronomically-calibrated fluvial strata, Bighorn Basin, Wyoming, USA. *Earth and Planetary Science Letters, 534*, 116044.

van Houten, F. (1944). Stratigraphy of the Willwood and Tatman formations in northwestern Wyoming. *Bulletin of the Geological Society of America, 55*, 165-210.

van Oorschot, I. H., & Dekkers, M. J. (1999). Dissolution behaviour of fine-grained magnetite and maghemite in the citrate–bicarbonate–dithionite extraction method. *Earth and Planetary Science Letters, 167*(3-4), 283-295.

Vandenberghe, N., Hilgen, F., Speijer, R., Ogg, J., Gradstein, F., Hammer, O., . . . Hooker, J. (2012). The Paleogene Period. In F. Gradstein, J. Ogg, M. Schmitz, & G. Ogg, *The Geologic Time Scale 2012* (1 ed., pp. 855-921). Boston: Elsevier.

Westerhold, T., Röhl, U., Frederichs, T., Agnini, C., Raffi, I., Zachos, J. C., & Wilkens, R. H. (2017). Astronomical calibration of the Ypresian timescale: implications for seafloor spreading rates and the chaotic behavior of the solar system? *Climate of the past*(13), 1129-1152.

Westerhold, T., Röhl, U., Frederichs, T., Agnini, C., Raffi, I., Zachos, J. C., & Wilkens, R. H. (2017). Astronomical calibration of the Ypresian timescale: implications for seafloor spreading rates and the chaotic behavior of the solar system? *Climate of the past*(13), 1129-1152.

Westerhold, T., Röhl, U., Wilkens, R. H., Gingerich, P. D., Clyde, W. C., Wing, S. L., . . . Kraus, M. J. (2018). Synchronizing early Eocene deep-sea and continental records - Cyclostratigraphic age models for the Bighorn Basin Coring Project drill cores. *Clim. Past, 14*, 303-319.

Wijbrans, J. R., Pringle, M. S., Koppers, A. A., & Scheveers, R. (1995). Argon geochronology of small samples using the Vulkaan argon laserprobe. *Proceedings of the Royal Netherlands Academy of Arts and Sciences, 98*(2), 185-218.

Wing, S. L., & Bown, T. M. (1985). Fine scale reconstruction of Late Paleocene-Early Eocene paleogeography in the Bighorn basin of Northern Wyoming. *Cenozoic paleogeography of West-Central United States*, 93-105.

Wing, S., Bown, T., & Obradovich, J. (1991). Early Eocene biotic and climatic change in interior western North America. *Geology, 19*, 1189-1192.

Zachos, J. C., Dickens, G. R., & Zeebe, R. E. (2008). An early Cenozoic perspective on greenhouse warming and carbon-cycle dynamics. *Nature, 451*, 279-283.

Zachos, J. C., McCarren, H., Murphy, B., Röhl, U., & Westerhold, T. (2010). Tempo and scale of late Paleocene and early Eocene carbon isotope cycles: Implications for the origin of hyperthermals. *Earth and Planetary Science Letters, 299*, 242-249.

Zachos, J., Pagani, M., Sloan, L., Thomas, E., & Billups, K. (2001). Trends , Rhythms , and Aberrations in Global Climate 65 Ma to Present. *Science*(292), 686-694.

Zijderveld, J. D. (1967). A. C. Demagnetization of Rocks: Analysis of Results. In D. W. Collinson, K. M. Creer, & S. K. Runcorn, *Methods in Palaeomagnetism* (pp. 254-286). Amsterdam: Elsevier.

Appendix I - Detailed lithostratigraphic logs

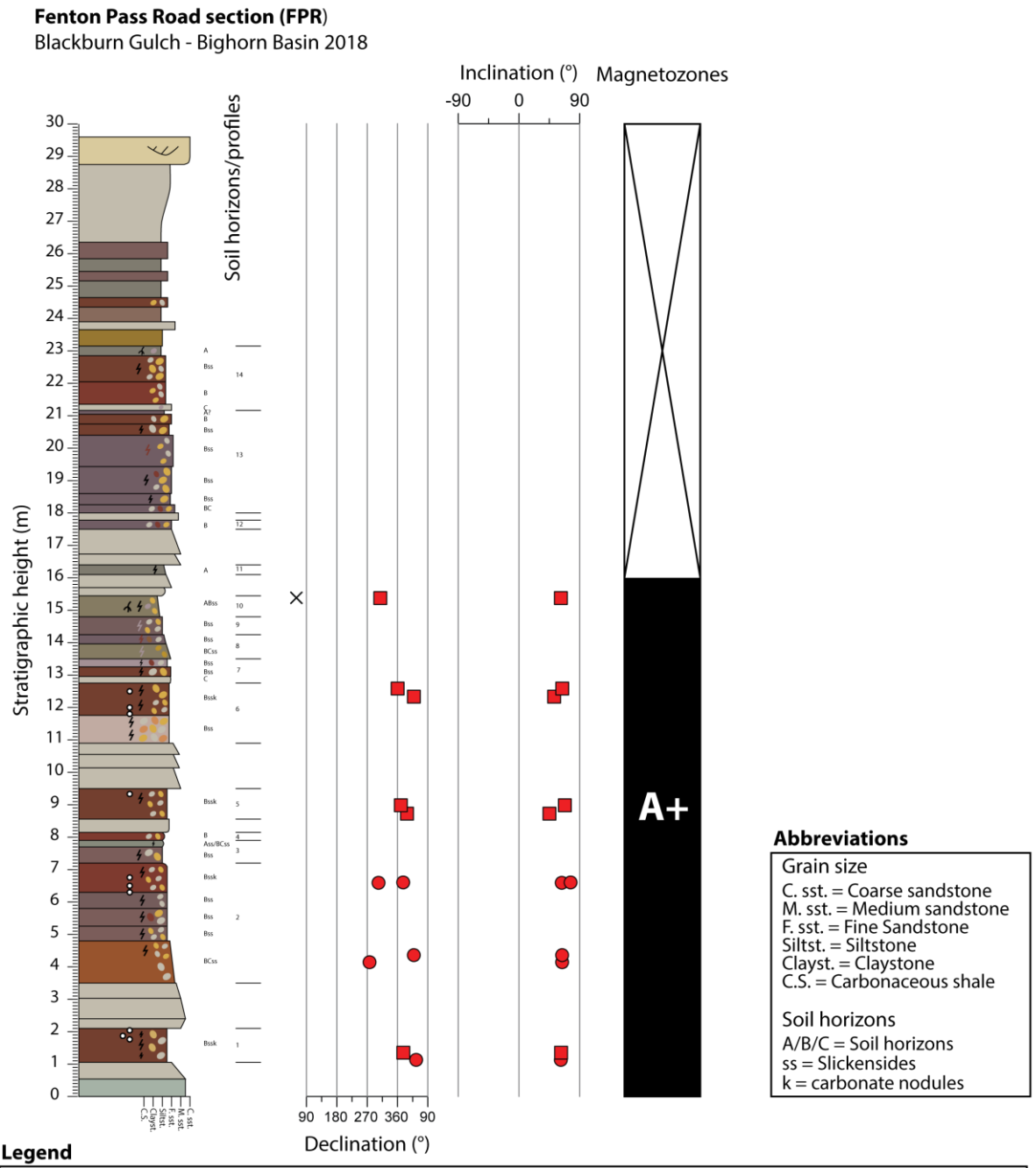

Blackburn Gulch Downward extension (BBGD)

Blackburn Gulch - Bighorn Basin 2018

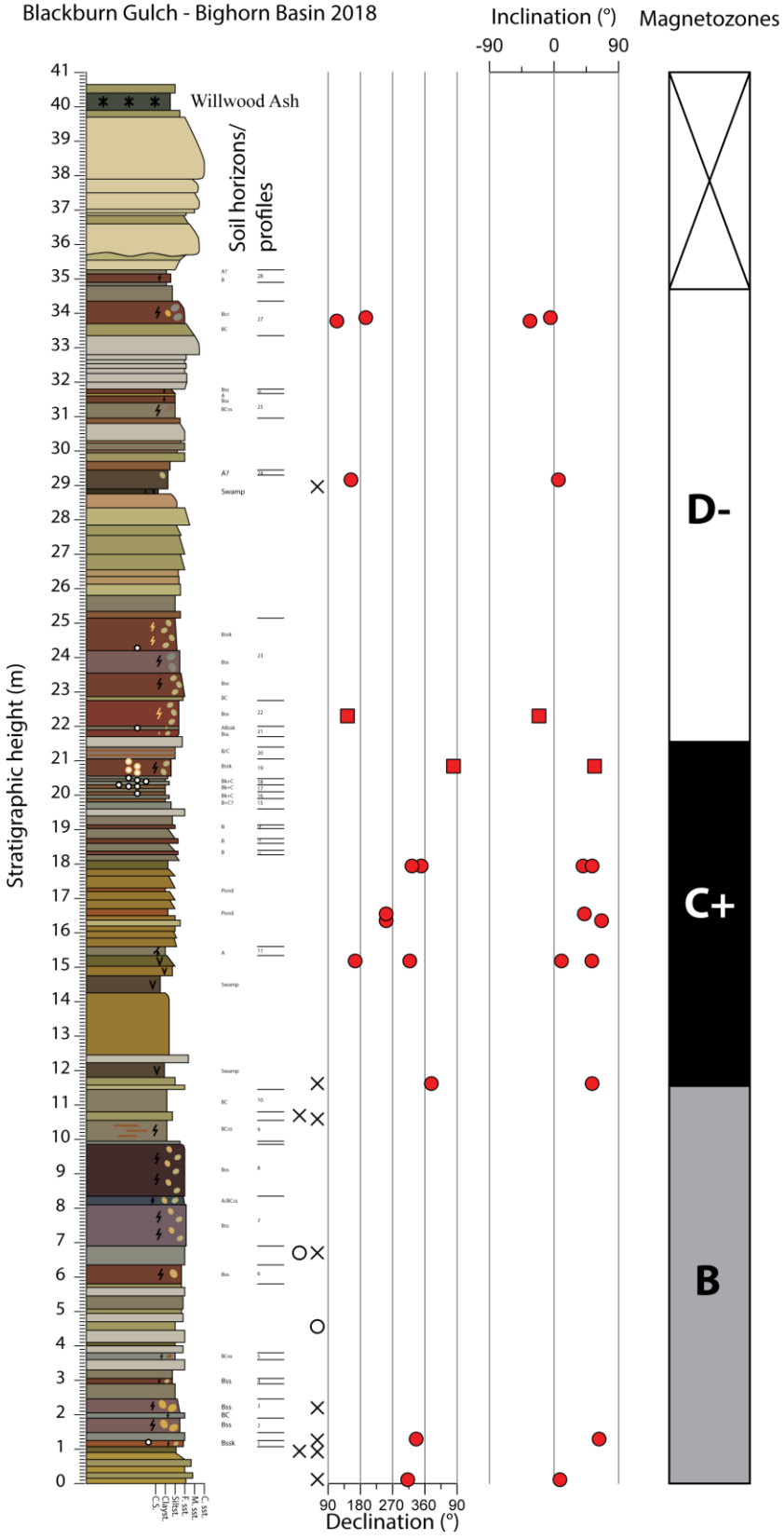

Blackburn Gulch section (BBG)
Section BBG1 (0-35.35m) and Section BBG2 (30-55.70m)
Blackburn Gulch - Bighorn Basin 2018

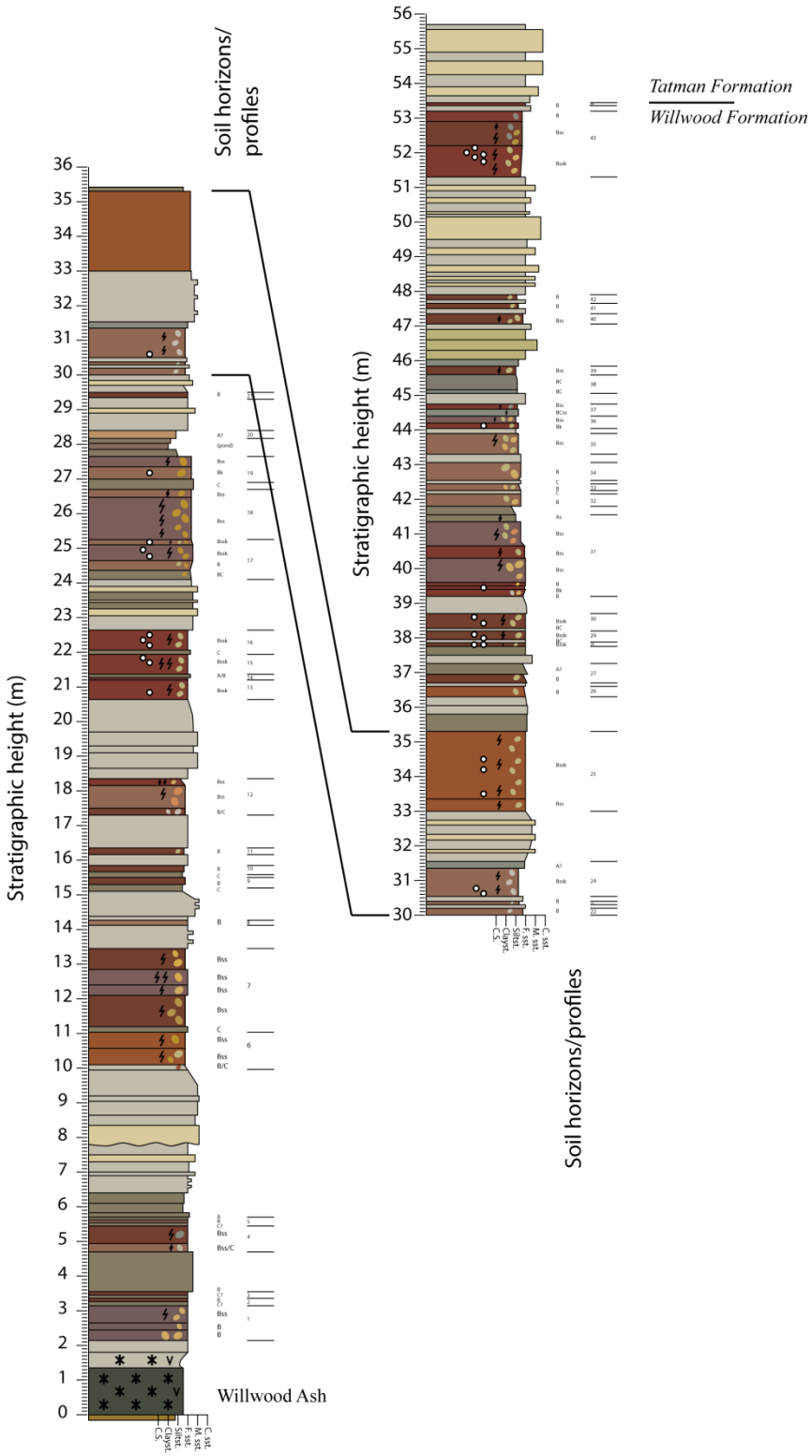

Blackburn Gulch Upward extension (BBGU)
Single section
Blackburn Gulch - Bighorn Basin 2018

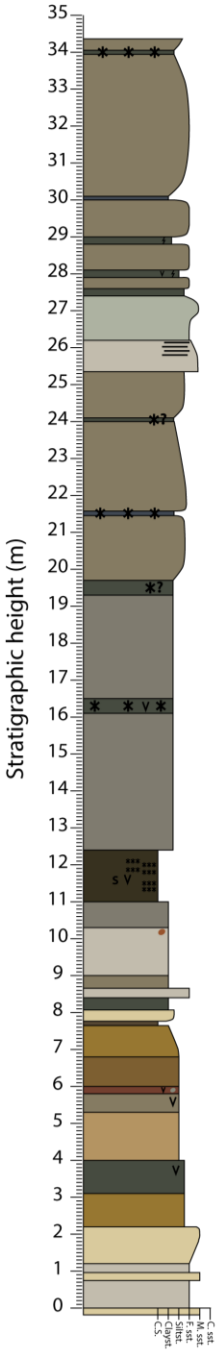

Squaw Buttes North Downward extension (SBND)
Squaw Buttes - Bighorn Basin 2017

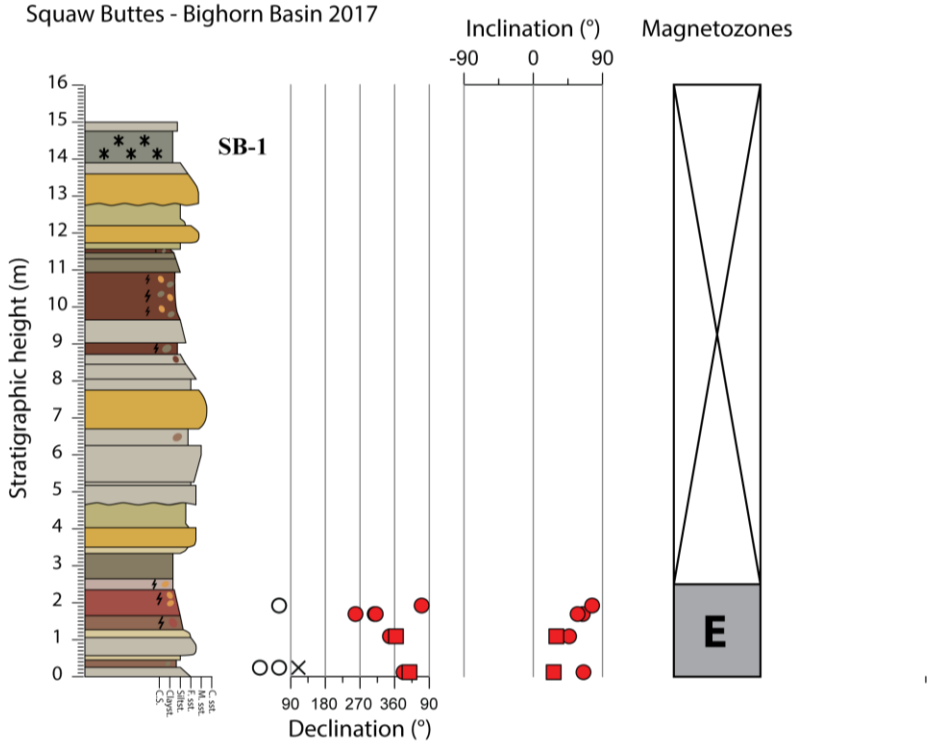

Squaw Buttes North (SBN) Gap section
Squaw Buttes - Bighorn Basin 2017

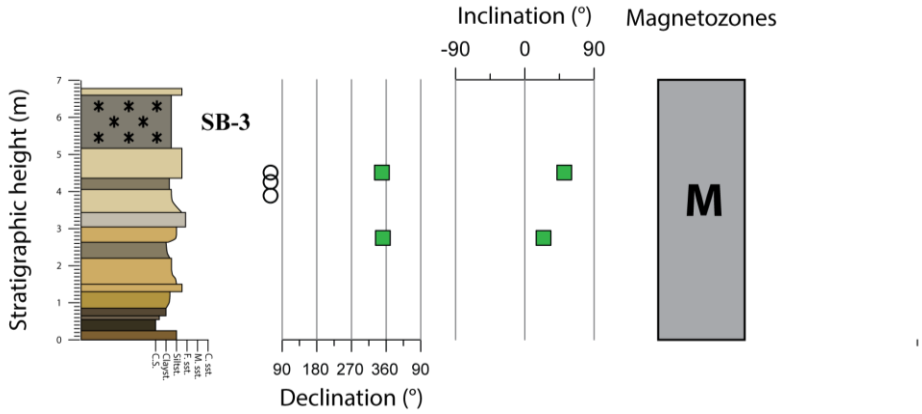

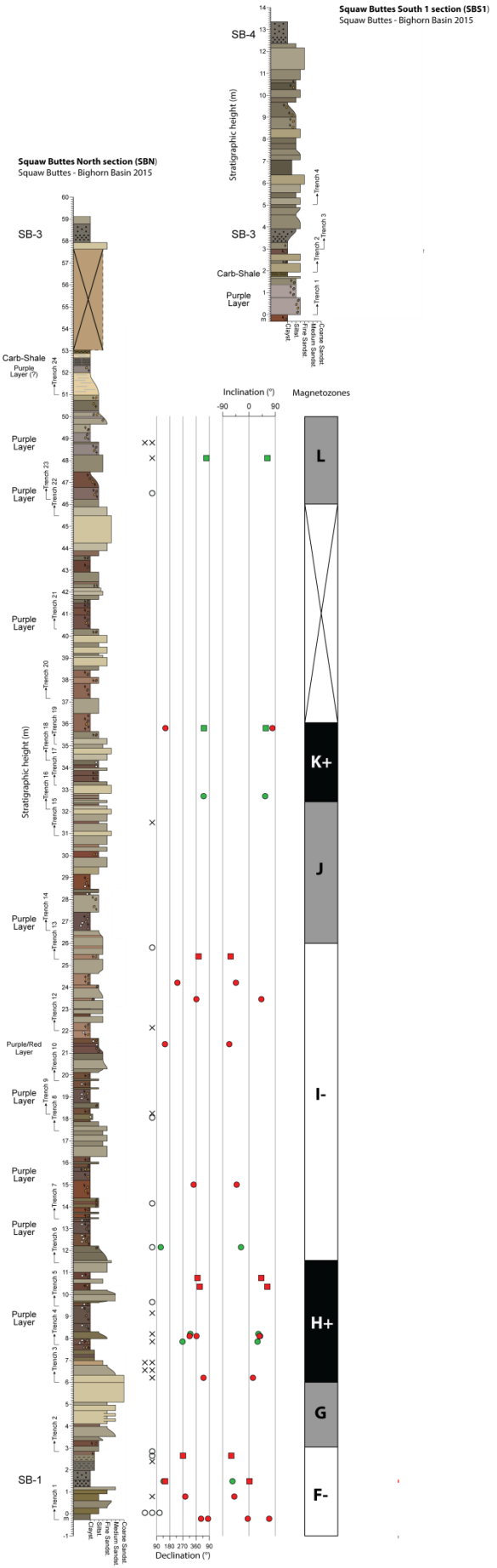

Lithostratigraphic logs SBN and SBS1 adapted from A. Turtù (unpublished)

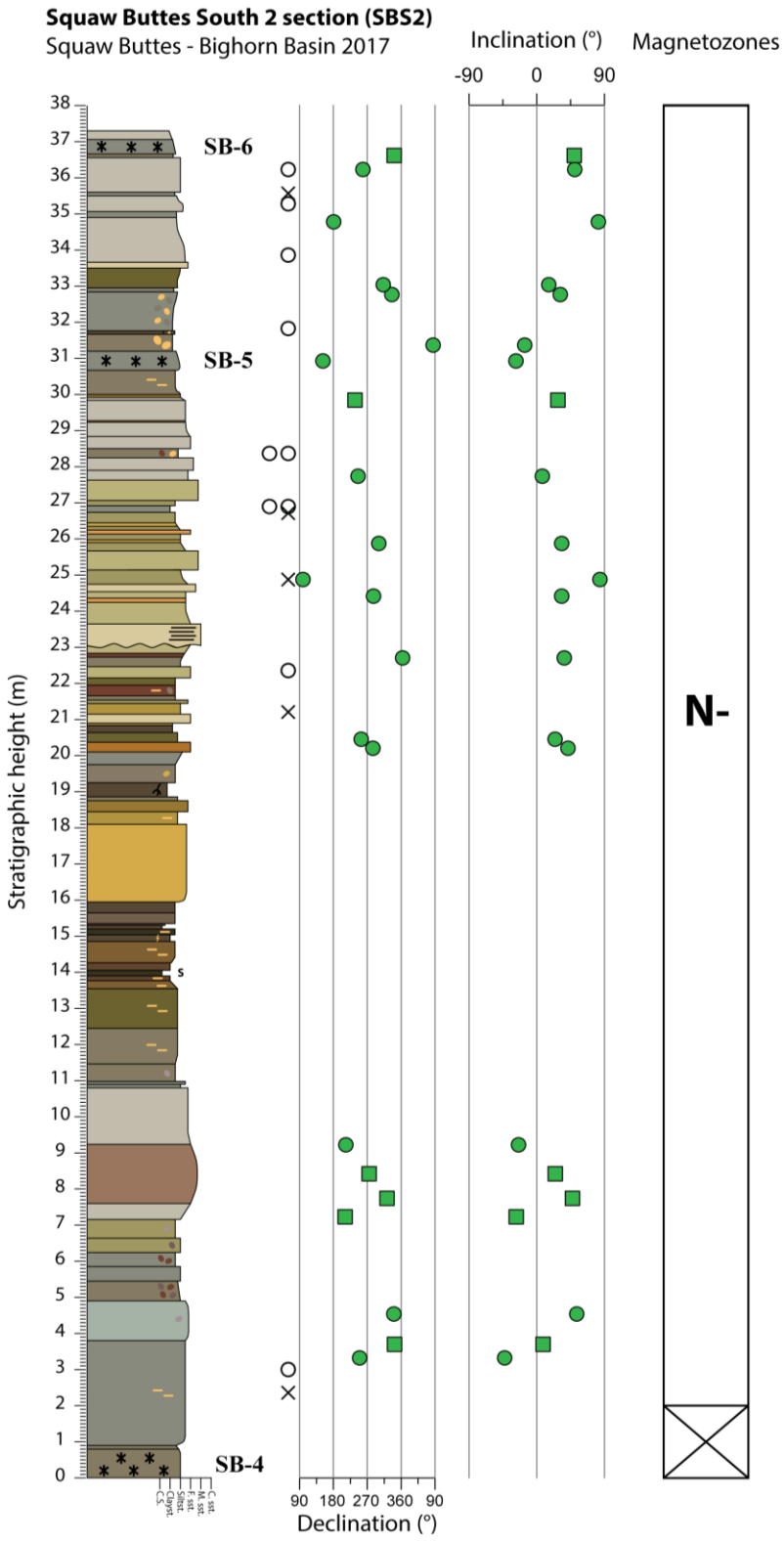
Squaw Buttes South 2 section (SBS2)
Squaw Buttes - Bighorn Basin 2017
Inclination (°)
-90
0
90
Magnetozones
SB-6
SB-5
SB-4
N-
Stratigraphic height (m)
90 180 270 360 90
Declination (°)

Squaw Buttes Upward extension (SBU)
Single section
Squaw Buttes - Bighorn Basin 2018

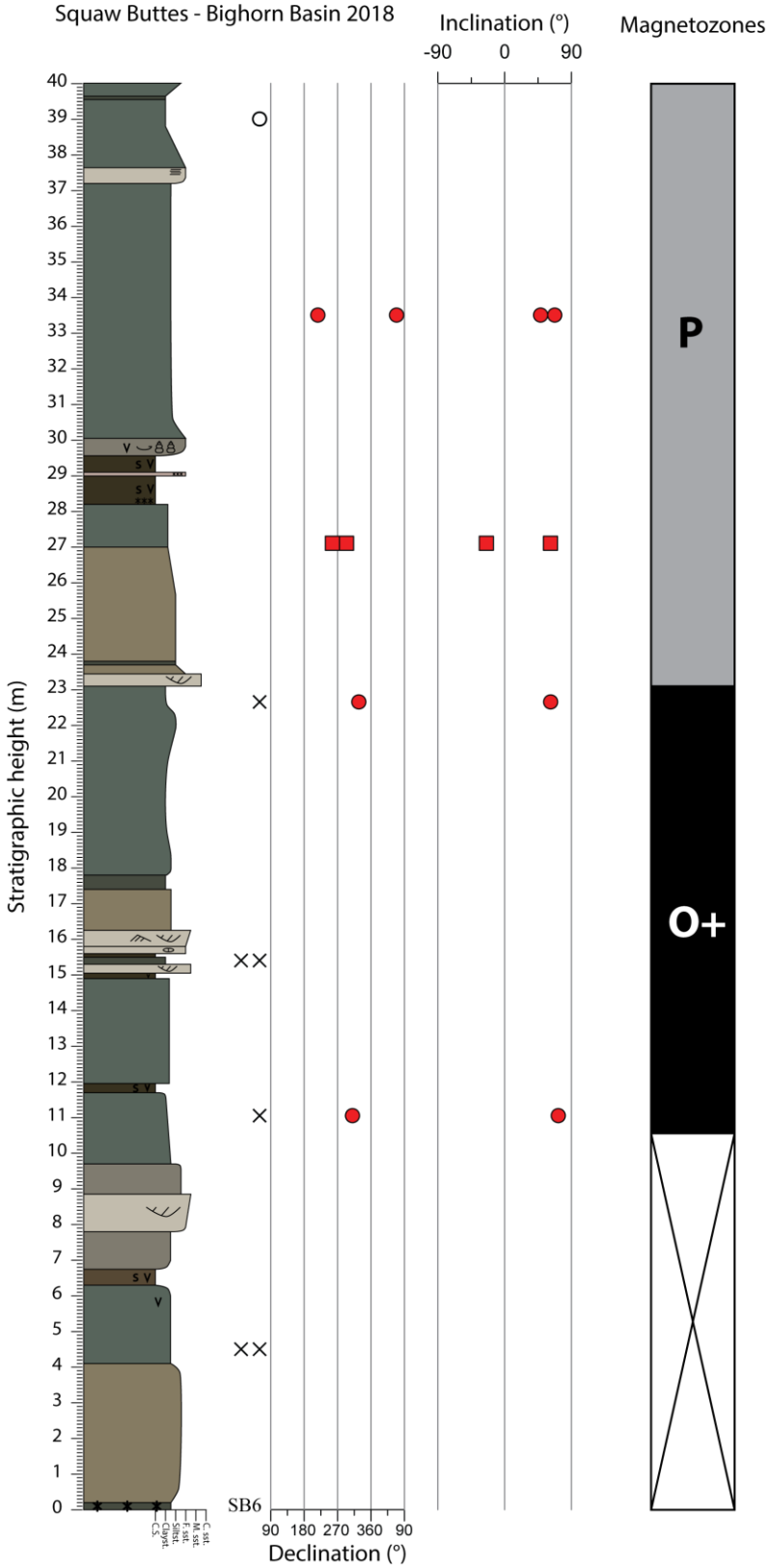

Squaw Buttes Upward extension (SBU) - Continued

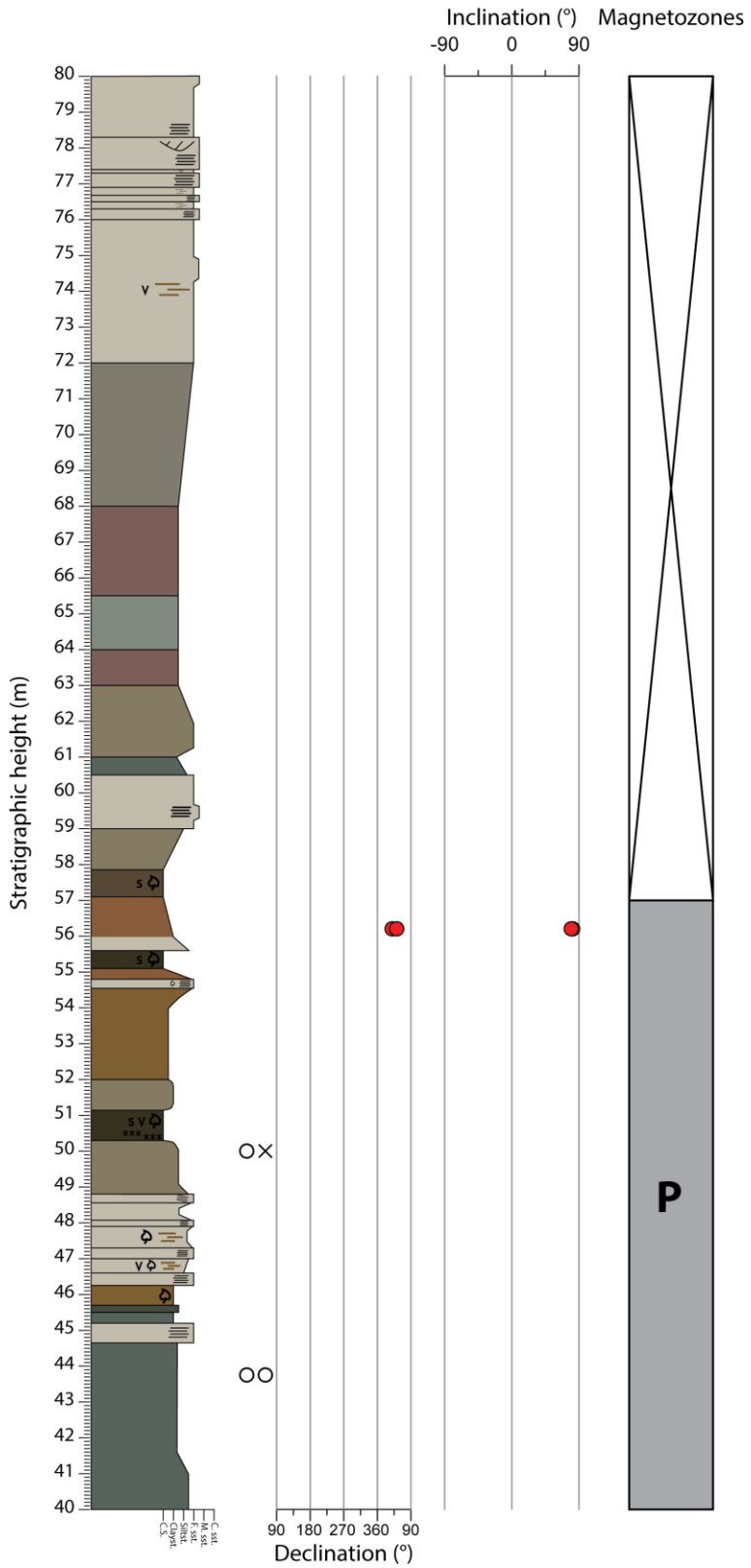

Squaw Buttes Upward extension (SBU) - Continued

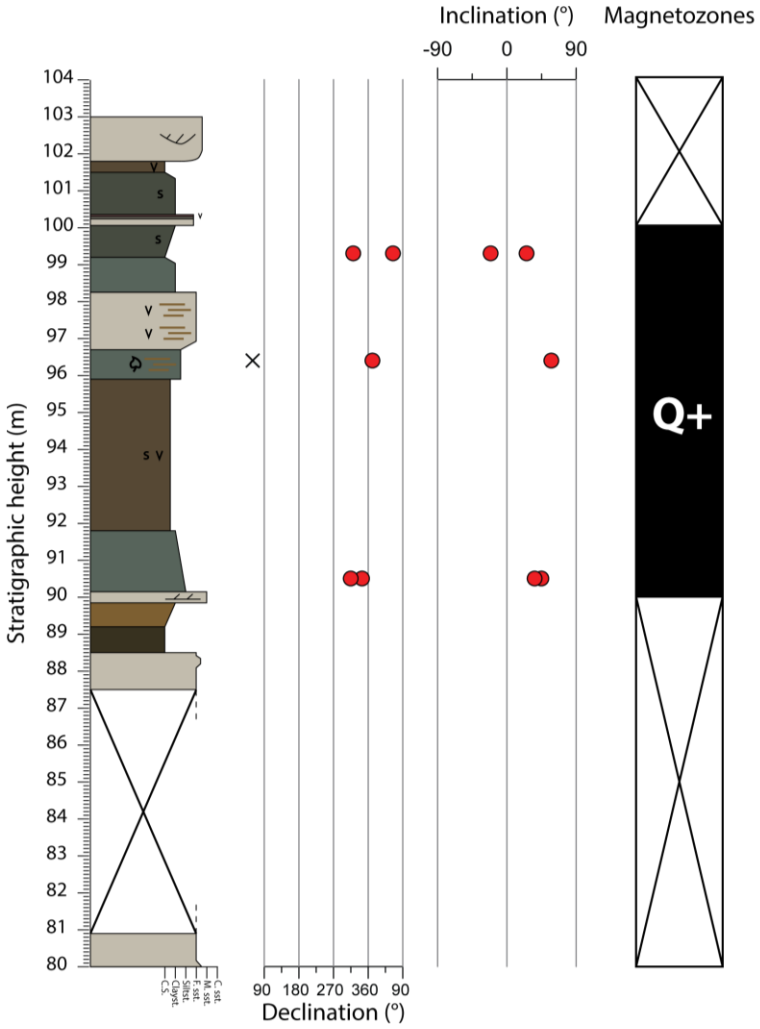

Appendix II - Irradiation cup layouts

Irradiation batch VU111

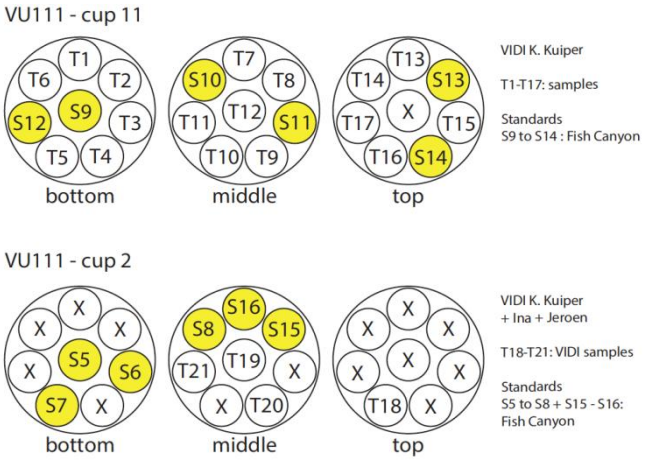

ID	Sample	Relevant FCT standards
T15	SB1	S10, S11, S13, S14
T16	SB3	S10, S11, S13, S14
T17	SB4	S10, S11, S13, S14
T18	SB5	S6, S7, S8, S15, S16

Irradiation batch VU112

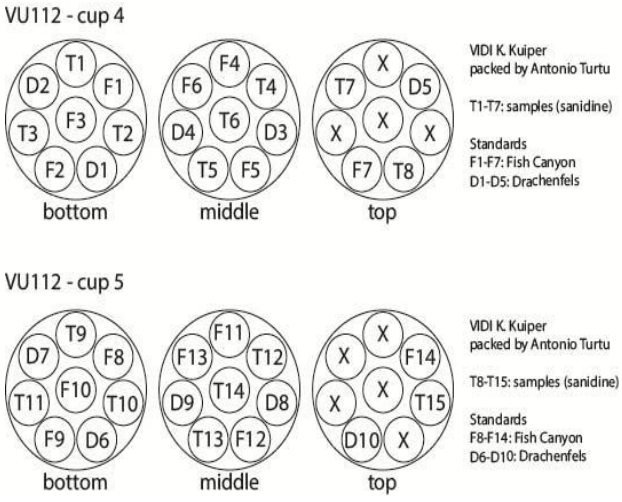

ID	Sample	Relevant FCT standards
T13	WA-2017-1	F8, F9, F10, F11, F12, F13, F14
T14	BBG-2017-1	F8, F9, F10, F11, F12, F13, F14
T15	SBN-2017-SB3	F8, F9, F10, F11, F12, F13, F14